



저작자표시 2.0 대한민국

이용자는 아래의 조건을 따르는 경우에 한하여 자유롭게

- 이 저작물을 복제, 배포, 전송, 전시, 공연 및 방송할 수 있습니다.
- 이차적 저작물을 작성할 수 있습니다.
- 이 저작물을 영리 목적으로 이용할 수 있습니다.

다음과 같은 조건을 따라야 합니다:



저작자표시. 귀하는 원저작자를 표시하여야 합니다.

- 귀하는, 이 저작물의 재이용이나 배포의 경우, 이 저작물에 적용된 이용허락조건을 명확하게 나타내어야 합니다.
- 저작권자로부터 별도의 허가를 받으면 이러한 조건들은 적용되지 않습니다.

저작권법에 따른 이용자의 권리는 위의 내용에 의하여 영향을 받지 않습니다.

이것은 [이용허락규약\(Legal Code\)](#)을 이해하기 쉽게 요약한 것입니다.

[Disclaimer](#) 

공학박사학위논문

고성능 리튬이차전지용 인산염계
양극 소재에 관한 연구

**Tailoring phosphate cathode
materials for high performance
lithium rechargeable battery**

2014년 2월

서울대학교 대학원

재료공학부

김 종 순

고성능 리튬이차전지용 인산염계

양극 소재에 관한 연구

**Tailoring phosphate cathode materials for high
performance lithium rechargeable battery**

지도교수 강 기 석

이 논문을 공학박사 학위논문으로 제출함

2014 년 2 월

서울대학교 대학원

재료공학부

김종순

김종순의 박사 학위논문을 인준함

2013 년 12 월

위 원 장 _____ 남 기 태 (인)

부위원장 _____ 장 호 원 (인)

위 원 _____ 강 기 석 (인)

위 원 _____ 박 찬 범 (인)

위 원 _____ 전 석 우 (인)

Abstract

Tailoring phosphate cathode materials for high performance lithium rechargeable battery

Jongsoon Kim

Department of Material Science and Engineering

The Graduate School

Seoul National University

Electrochemical energy storage systems have attracted tremendous interests due to skyrocketing growth of sustainable and environmental-friendly energy market in the world. Lithium rechargeable batteries have been widely used as the energy storage system for portable electronic due to its high energy/power density and long cycle life. Recently, intensive research efforts have focused on the development of Li rechargeable battery for large scale applications such as electric vehicles. Conventional cathode materials such as lithium transition metal oxides (LiMO_2 , M = transition metals) possess intrinsic chemical instability at overcharged state. They release oxygen from the crystal structure or experience irreversible phase transformation at

elevated temperature, which consequently raises safety concerns during operation. In this respect, numerous studies have been carried out in order to find a safe and stable cathode material. Among many candidates, phosphate materials have been considered as the best candidate of energy storage system for large-scale applications due to its high structural stability and safety by strong P-O covalent bonding, potentially low production cost, high energy density, and excellent cyclability. In this thesis, various phosphate electrode materials such as olivine, NASICON, and alluaudite are investigated.

Olivine studies consist of three parts: (i) the improvement of electrochemical performance of LiMnPO_4 , (ii) the particle size effect on phase stability on the LiMnPO_4 , and (iii) thermal stability of binary olivine $\text{LiFe}_{1-x}\text{Mn}_x\text{PO}_4$. In the (i) part, we demonstrate that the electrochemical properties of LiMnPO_4 can be significantly improved by doping small amount of Fe and Mg. The presence of Fe and Mg in LiMnPO_4 provide multiple nucleation sites, unlike pure LiMnPO_4 , thus the power capability of a LiMnPO_4 was significantly enhanced by easier Li^+ de/intercalation resulted from multiple nucleation sites. Fe-Mg co-doped $\text{LiFe}_{0.05}\text{Mn}_{0.05}\text{Mn}_{0.9}\text{PO}_4$ indicates a discharge capacity of $\sim 140\text{mAh g}^{-1}$ at C/5 rate ($1\text{C} = 170\text{mA g}^{-1}$) and the high capacity is retained at even higher current rates (110mAh g^{-1} at

3C), which has yet to be achieved in LiMnPO_4 without nucleation enhancers.

In the (ii) part, the particle size effect on the phase stability of delithiated LiMnPO_4 is elucidated using temperature-controlled *in situ* X-ray diffraction. The phase stability of Li_xMnPO_4 ($x < 1$) at high temperature was significantly influenced by the particle size. While Li_xMnPO_4 phase having large particle size (larger than 200nm) decomposed into $\text{Mn}_2\text{P}_2\text{O}_7$ at the temperature above 200°C , delithiated Li_xMnPO_4 was transformed into $\text{Mn}_3(\text{PO}_4)_2$ above 200°C when the delithiated Li_xMnPO_4 has a small particle size (*ca.* 50 nm). This indicates that the phase transformation of a LiMnPO_4 -based battery is influenced by the particle size.

In the (iii) part, the phase stability of $\text{LiFe}_{1-x}\text{Mn}_x\text{PO}_4$ is extensively studied. It is identified that the thermal stability of partially delithiated $\text{Li}_{1-y}\text{Fe}_{1-x}\text{Mn}_x\text{PO}_4$ is sensitively affected by the Fe/Mn ratio of $\text{Li}_{1-y}\text{Fe}_{1-x}\text{Mn}_x\text{PO}_4$. While Fe-rich material in $\text{Li}_{1-y}\text{Fe}_{1-x}\text{Mn}_x\text{PO}_4$ readily formed a solid solution phase of $\text{Li}_{1-y}\text{Fe}_{1-x}\text{Mn}_x\text{PO}_4$ near room temperature or with only slight heating, the Mn-rich material in $\text{Li}_{1-y}\text{Fe}_{1-x}\text{Mn}_x\text{PO}_4$ retained its two-phase characteristic up to $\sim 250^\circ\text{C}$ before decomposition into non-olivine phases. The decomposition mechanism of fully delithiated $\text{Li}_{1-y}\text{Fe}_{1-x}\text{Mn}_x\text{PO}_4$ is more sensitively affected by the Fe/Mn ratio in the crystal. It is identified that the decomposition temperature of $\text{Li}_{1-y}\text{Fe}_{1-x}\text{Mn}_x\text{PO}_4$ is higher when Fe/Mn ratios in the structure increase.

The NASICON study is focused on the improvement of electrochemical performances of monoclinic $\text{Li}_3\text{V}_2(\text{PO}_4)_3$. The power capability of the $\text{Li}_3\text{V}_2(\text{PO}_4)_3$ electrode can be greatly improved by a simple low-temperature coating of a conducting polymer, namely, poly(3,4-ethylenedioxythiophene) (PEDOT). The carbon-free $\text{Li}_3\text{V}_2(\text{PO}_4)_3/\text{PEDOT}$ electrode delivered *ca.* 120 mAh g^{-1} , more than 90% of its theoretical capacity of 133mAh g^{-1} , at a rate of 10C (where 1C = 133 mA g^{-1}). The capacity retention at this rate was 97% after 100 cycles. At 30C, $\text{Li}_3\text{V}_2(\text{PO}_4)_3/\text{PEDOT}$ delivered *ca.* 110mAh g^{-1} . This remarkable power and cycle stability achieved by a simple coating process places this 4V-class electrode among the most promising electrode candidates for next-generation batteries.

In the alluaudite study, we focus the non-olivine LiFePO_4 with alluaudite structure. Non-olivine LiFePO_4 with an alluaudite structure were successfully prepared for the first time via soft chemical ion-exchange of the novel alluaudite $\text{Na}_{0.67}\text{FePO}_4$. The open crystal structure of alluaudite LiFePO_4 allows fast lithium motion as evidenced from the reversible electrochemical cycling in a lithium rechargeable battery system. About 0.8 Li in LiFePO_4 could be extracted and reinserted in a highly reversible manner. The charge/discharge profile reveal that the one-phase (solid-solution) reaction based lithiation and delithiation occurs within the

alluaudite crystal structure contrary to the well-known two-phase reaction in the olivine LiFePO_4 .

In conclusion, phosphate electrode materials such as olivine, NASICON, and alluaudite have the excellent characteristics enough to be used as the cathode material for large-scale applications. We believe that the results reported herein provide a new basis and strategy for phosphate cathode materials, which can be used as better-performing lithium rechargeable batteries.

Keywords: Li rechargeable battery, phosphate, olivine, NASICON, alluaudite

Student Number: 2011-30783

Table of Contents

Abstract	i
Table of contents	vi
List of tables	ix
List of figures	x
Chapter 1 Introduction	1
1.1 Reference.....	10
Chapter 2 General Backgrounds	13
2.1 Lithium Rechargeable Battery.....	13
2.2 Phosphate Electrodes	15
2.2.1 Olivine Electrodes.....	15
2.2.2 NASICON Electrodes.....	19
2.2.3 Alluaudite Electrodes	21
2.3 Reference.....	27
Chapter 3 Olivine Electrode	30
3.1 Nucleation enhancer for high power Mn based olivine cathode materials.....	30
3.1.1 Research Background	30

3.1.2 Experimental Section	31
3.1.3 Results and Discussion	33
3.1.4 Concluision	39
3.1.5 References.....	49
3.2 The Effect of Particle Size on Phase Stability of the Delithiated Li _x MnPO ₄	53
3.2.1 Research Background	53
3.2.2 Experimental Section	54
3.2.3 Computational Details	56
3.2.4 Results and Discussion	56
3.2.5 Concluision	63
3.2.6 References.....	73
3.3 Thermal stability of Fe-Mn binary olivine cathode for Li rechargeable battery	76
3.3.1 Research Background	76
3.3.2 Experimental Section	78
3.3.3 Computational Details	79
3.3.4 Results and Discussion	80
3.3.5 Concluision	97
3.3.6 References.....	118

Chapter 4 NASICON Electrode.....	121
4.1 $\text{Li}_3\text{V}_2(\text{PO}_4)_3/\text{Conducting Polymer}$ as a High Power 4V-class Lithium battery electrode.....	121
4.1.1 Research Background	121
4.1.2 Experimental Section	123
4.1.3 Results and Discussion	124
4.1.4 Concluision	129
4.1.5 References.....	138
Chapter 5 Alluaudite electrode	141
5.1 LiFePO_4 with an alluaudite crystal structure for lithium ion batteries.....	141
5.1.1 Research Background	141
5.1.2 Experimental Section	143
5.1.3 Results and Discussion	145
5.1.4 Concluision	151
5.1.5 References.....	166
Chapter 6 Summary.....	169
Chapter 7 Abstract in Korean.....	173

List of Tables

Table 3.1.1 Lattice parameters of LiMnPO_4 and $\text{LiFe}_{0.05}\text{Mg}_{0.05}\text{Mn}_{0.9}\text{PO}_4$ obtained by the Rietveld refinement	47
Table 3.1.2 Site occupancies of $\text{LiFe}_{0.05}\text{Mg}_{0.05}\text{Mn}_{0.9}\text{PO}_4$ obtained by the Rietveld refinement	48
Table 3.3.1 Atomic ratio of metal ions (Li, Fe, and Mn) in $\text{Li}_{1-y}\text{Fe}_{1-x}\text{Mn}_x\text{PO}_4$ [$0 \leq x, y \leq 1$]	115
Table 3.3.2 Lattice parameters of $\text{LiFe}_{1-x}\text{Mn}_x\text{PO}_4$ [$0 \leq x \leq 1$]	116
Table 3.3.3 The thermal coefficients of $\text{LiFe}_{1-x}\text{Mn}_x\text{PO}_4$ [$0 \leq x \leq 1$]	117
Table 4.1.1 Lattice parameters of pristine $\text{Li}_3\text{V}_2(\text{PO}_4)_3$, delithiated $\text{Li}_{3-x}\text{V}_2(\text{PO}_4)_3$, and $\text{Li}_3\text{V}_2(\text{PO}_4)_3/\text{PEDOT}$ composite	137
Table 5.1.1 Lattice parameters of alluaudite $\text{Na}_{0.67}\text{FePO}_4$	161
Table 5.1.2 Atomic position and occupancy of refined $\text{Na}_{0.67}\text{FePO}_4$ using the ND pattern	162
Table 5.1.3 The atomic ratio of the ion-exchanged alluaudite- $\text{Li}_{0.67}\text{FePO}_4$ at harsh conditions (5M LiBr in Hexanol for 48 hours at 170°C)	163
Table 5.1.4 Atomic position and occupancy of refined alluaudite $\text{Li}_{0.67}\text{FePO}_4$ using the XRD pattern	164
Table 5.1.5 Atomic position and occupancy of refined alluaudite $\text{Li}_{0.67}\text{FePO}_4$ using the ND pattern	165

List of Figures

Figure 1.1 Renewable energy sources	8
Figure 1.2 Comparison of various battery systems	9
Figure 2.1.1. Cell structure and principles of Li rechargeable Battery. The charge and discharge cycles are achieved through the exchange of lithium ions between the positive and negative electrodes.	23
Figure 2.2.1. Structures of Olivine LiMPO_4 (M = Fe, Mn, Co, Ni)	24
Figure 2.2.2 Structure of (a) Rhombohedral $\text{Li}_3\text{V}_2(\text{PO}_4)_3$ and (b) Monoclinic $\text{Li}_3\text{V}_2(\text{PO}_4)_3$	25
Figure 2.2.3. General alluaudite structure	26
Figure 3.1.1 (Color online) Schematic illustration of the nucleation enhancing process in a multicomponent Mn based olivine cathode during charging and discharging (Yellow: Li, red: MnO_6 , purple: FeO_6 , blue: MgO_6 , orange: PO_4 , white: vacancy). Arrows are used to indicate the favorable interaction.	41
Figure 3.1.2 (Color online) XRD patterns and lattice parameter of LiMnPO_4 and $\text{LiFe}_{0.05}\text{Mg}_{0.05}\text{Mn}_{0.9}\text{PO}_4$ between $2\theta = 15^\circ$ and $2\theta = 45^\circ$	42
Figure 3.1.3 Scanning electron microscopy images of (a) LiMnPO_4 and (b) $\text{LiFe}_{0.05}\text{Mg}_{0.05}\text{Mn}_{0.9}\text{PO}_4$	43
Figure 3.1.4 (Color online) (a) Rate capability of $\text{LiFe}_{0.05}\text{Mg}_{0.05}\text{Mn}_{0.9}\text{PO}_4$	

LiMnPO₄ from C/5 to 3C; 1C corresponds to about 171 mA g⁻¹, (b) The Ragone plot for LiMnPO₄ and LiFe_{0.05}Mg_{0.05}Mn_{0.9}PO₄, (c) Galvanostatic cyclability data of the 50 cycles for LiFe_{0.05}Mg_{0.05}Mn_{0.9}PO₄ between 4.8 and 2 V at a C/3 rate, (d) Corresponding charge/discharge curves of the 50 cycles for LiFe_{0.05}Mg_{0.05}Mn_{0.9}PO₄. 44

Figure 3.1.5 (Color online) (a) Charge/discharge profile of LiFe_{0.05}Mg_{0.05}Mn_{0.9}PO₄ [(i): the charge state of the examined Li_{1-x}Fe_{0.05}Mg_{0.05}Mn_{0.9}PO₄; (ii): the discharge state of the examined Li_xFe_{0.05}Mg_{0.05}Mn_{0.9}PO₄], (b) Typical HRTEM image of a particle charged up to 0.4V, (c) Fourier transforms of the Figure 4(b) image [yellow circle: delithiated phase], (d) Typical HRTEM image of a particle charging up to 4.8V, and (e) Fourier transforms of the Figure 4(d) image [yellow circle: lithiated phase] 45

Figure 3.1.6 (Color online) PITT measurements upon charging of (a) LiFe_{0.05}Mg_{0.05}Mn_{0.9}PO₄ and (b) LiMnPO₄ from 3 to 4.6 V, and the zoomed PITT profiles of LiFe_{0.05}Mg_{0.05}Mn_{0.9}PO₄ (c) between 7 and 10 h and (d) between 21 and 26 h. 46

Figure 3.2.1 SEM images of three different pristine LiMnPO₄ synthesized at (a) 600°C, (b) 700°C and (c) 800°C 64

Figure 3.2.2 Evolution of XRD patterns of Li_xMnPO₄-800 [0 < x ≤ 1] with a

delithiation process..... 65

Figure 3.2.3 (a) *in-situ* XRD patterns of partially delithiated $\text{Li}_x\text{MnPO}_4\text{-800}$ (PD1) at high temperature from 200°C to 400°C around $2\theta = 24^\circ\sim 40^\circ$, (b) *in-situ* XRD patterns of more partially delithiated $\text{Li}_x\text{MnPO}_4\text{-800}$ (PD2) at high temperature from 200°C to 400°C around $2\theta = 24^\circ \sim 40^\circ$, and (c) *in-situ* XRD patterns of nearly fully delithiated $\text{Li}_x\text{MnPO}_4\text{-800}$ (PD3) at high temperature from 200°C to 400°C around $2\theta = 24^\circ\sim 40^\circ$. [Li amount in the structure: PD1 > PD2 > PD3] 66

Figure 3.2.4 XRD patterns of $\text{Li}_x\text{MnPO}_4\text{-700}$ [$0 \leq x \leq 1$]..... 67

Figure 3.2.5 (a) *in-situ* XRD patterns of partially delithiated $\text{Li}_x\text{MnPO}_4\text{-700}$ at high temperature from 200°C to 400°C around $2\theta = 24^\circ\sim 40^\circ$, and (b) *in-situ* XRD patterns of fully delithiated $\text{Li}_x\text{MnPO}_4\text{-700}$ at high temperature from 200°C to 400°C around $2\theta = 24^\circ\sim 40^\circ$ 68

Figure 3.2.6 XRD patterns of $\text{Li}_x\text{MnPO}_4\text{-600}$ [$0 \leq x \leq 1$]..... 69

Figure 3.2.7 (a) *in-situ* XRD patterns of fully delithiated $\text{Li}_x\text{MnPO}_4\text{-600}$ as temperature is increased up to 450°C around $2\theta = 15^\circ\sim 45^\circ$, (b) *in-situ* XRD patterns of fully delithiated $\text{Li}_x\text{MnPO}_4\text{-600}$ at high temperature from 200°C to 400°C around $2\theta = 15^\circ\sim 45^\circ$, (c) *in-situ* XRD patterns of partially delithiated $\text{Li}_x\text{MnPO}_4\text{-600}$ as temperature is increased up to 450°C around $2\theta = 15^\circ\sim 45^\circ$, and (d) *in-situ* XRD patterns of partial delithiated $\text{Li}_x\text{MnPO}_4\text{-600}$

at high temperature from 200°C to 400°C around $2\theta = 15^\circ \sim 45^\circ$	70
Figure 3.2.8 Phase stability of delithiated Li_xMnPO_4 as functions of particle size and temperature.....	71
Figure 3.2.9 SEM images of pristine LiMnPO_4 and fully delithiated MnPO_4 synthesized at 600°C and 700°C (LMP-600 and 700).....	72
Figure 3.3.1 XRD patterns of as-prepared $\text{LiFe}_{1-x}\text{Mn}_x\text{PO}_4$ [$0 \leq x \leq 1$]	99
Figure 3.3.2 (a) <i>in-situ</i> XRD patterns of fully lithiated LiFePO_4 at temperature from 25°C to 700°C and at 2θ from 15° to 45°, (b) <i>in-situ</i> XRD patterns of fully lithiated $\text{LiFe}_{0.75}\text{Mn}_{0.25}\text{PO}_4$ at temperature from 25°C to 700°C and at 2θ from 15° to 45°, (c) <i>in-situ</i> XRD patterns of fully lithiated $\text{LiFe}_{0.5}\text{Mn}_{0.5}\text{PO}_4$ at temperature from 25°C to 700°C and at 2θ from 15° to 45°, (d) <i>in-situ</i> XRD patterns of fully lithiated $\text{LiFe}_{0.25}\text{Mn}_{0.75}\text{PO}_4$ at temperature from 25°C to 700°C and at 2θ from 15° to 45°, and (e) <i>in-situ</i> XRD patterns of fully lithiated LiMnPO_4 at temperature from 25°C to 700 °C and at 2θ from 15° to 45°.	100
Figure 3.3.3 (a) Lattice parameter <i>a</i> , (b) Lattice parameter <i>b</i> , (c) Lattice parameter <i>c</i> , and (d) volume of $\text{LiFe}_{1-x}\text{Mn}_x\text{PO}_4$ [$0 \leq x \leq 1$] varied by temperature	101
Figure 3.3.4 (a) Evolution of XRD patterns of $\text{Li}_{1-y}\text{FePO}_4$ [$0 \leq y \leq 1$] with a delithiation process, (b) Evolution of XRD patterns of $\text{Li}_{1-y}\text{Fe}_{0.75}\text{Mn}_{0.25}\text{PO}_4$ [0	

$\leq y \leq 1$] with a delithiation process, (c) Evolution of XRD patterns of $\text{Li}_{1-y}\text{Fe}_{0.5}\text{Mn}_{0.5}\text{PO}_4$ [$0 \leq y \leq 1$] with a delithiation process, (d) Evolution of XRD patterns of $\text{Li}_{1-y}\text{Fe}_{0.25}\text{Mn}_{0.75}\text{PO}_4$ [$0 \leq y \leq 1$] with a delithiation process, and (e) Evolution of XRD patterns of $\text{Li}_{1-y}\text{MnPO}_4$ [$0 \leq y \leq 1$] with a delithiation process 102

Figure 3.3.5 (a) *in-situ* XRD patterns of fully delithiated FePO_4 at temperature from 25°C to 700°C and at 2θ from 15° to 45° and (b) *in-situ* XRD patterns of fully delithiated FePO_4 at temperature from 450°C to 600°C and at 2θ from 24° to 40° 103

Figure 3.3.6 (a) *in-situ* XRD patterns of partially delithiated $\text{Li}_{0.6}\text{FePO}_4$ at temperature from 25°C to 700°C (2θ from 15° to 45°), (b) *in-situ* XRD patterns of partially delithiated $\text{Li}_{0.6}\text{FePO}_4$ at temperature from 300°C to 400°C (2θ from 15° to 45°), (c) *in-situ* XRD patterns of partially delithiated $\text{Li}_{0.6}\text{FePO}_4$ at temperature from 500°C to 650°C and at 2θ from 15° to 45°, (d) Comparison of lattice parameter a of $\text{Li}_{1-y}\text{FePO}_4$ [$y = 0, 0.4, \text{ and } 1$] varied by temperature and (e) XRD patterns of partially delithiated $\text{Li}_{0.6}\text{FePO}_4$ at 700°C compared with $\text{Fe}_2\text{P}_2\text{O}_7$ and $\text{Fe}_7(\text{PO}_4)_6$ among at 2θ from 15° to 45° . 104

Figure 3.3.7 (a) *in-situ* XRD patterns of fully delithiated MnPO_4 at temperature from 25°C to 700°C and at 2θ from 15° to 45°, (b) *in-situ* XRD patterns of fully delithiated MnPO_4 at temperature from 200°C to 400°C and

at 2θ from 24° to 40° , and (c) *in-situ* XRD patterns of fully delithiated MnPO_4 at temperature from 450°C to 600°C and at 2θ from 15° to 45° . [* : the XRD peak of Pt holder]..... 105

Figure 3.3.8 (a) *in-situ* XRD patterns of partially delithiated $\text{Li}_{0.5}\text{MnPO}_4$ at temperature from 25°C to 700°C and at 2θ from 15° to 45° , (b) *in-situ* XRD patterns of partially delithiated $\text{Li}_{0.5}\text{MnPO}_4$ at temperature from 200°C to 400°C , and at 2θ from 24° to 40° , and (c) *in-situ* XRD patterns of partially delithiated $\text{Li}_{0.5}\text{MnPO}_4$ at temperature from 500°C to 600°C and at 2θ from 15° to 45° 106

Figure 3.3.9 (a) *in-situ* XRD patterns of fully delithiated $\text{Fe}_{0.75}\text{Mn}_{0.25}\text{PO}_4$ at temperature from 25°C to 700°C and at 2θ from 15° to 45° , (b) *in-situ* XRD patterns of fully delithiated fully delithiated $\text{Fe}_{0.75}\text{Mn}_{0.25}\text{PO}_4$ at temperature from 450°C to 550°C and at 2θ from 24° to 40° , and (c) *in-situ* XRD patterns of fully delithiated fully delithiated $\text{Fe}_{0.75}\text{Mn}_{0.25}\text{PO}_4$ at temperature from 500°C to 600°C and at 2θ from 24° to 40° 107

Figure 3.3.10 (a) *in-situ* XRD patterns of partially delithiated $\text{Li}_{0.44}\text{Fe}_{0.75}\text{Mn}_{0.25}\text{PO}_4$ at temperature from 25°C to 700°C and at 2θ from 15° to 45° and (b) *in-situ* XRD patterns of partially delithiated $\text{Li}_{0.44}\text{Fe}_{0.75}\text{Mn}_{0.25}\text{PO}_4$ at temperature from 500°C to 600°C at 2θ from 15° to 45° 108

Figure 3.3.11 (a) *in-situ* XRD patterns of fully delithiated $\text{Fe}_{0.5}\text{Mn}_{0.5}\text{PO}_4$ at

temperature from 25°C to 700°C and at 2θ from 15° to 45°, (b) *in-situ* XRD patterns of fully delithiated fully delithiated $\text{Fe}_{0.5}\text{Mn}_{0.5}\text{PO}_4$ at temperature from 250°C to 400°C and at 2θ from 24° to 40°, and (c) *in-situ* XRD patterns of fully delithiated fully delithiated $\text{Fe}_{0.5}\text{Mn}_{0.5}\text{PO}_4$ at temperature from 550°C to 700°C and at 2θ from 24° to 40° 109

Figure 3.3.12 (a) *in-situ* XRD patterns of partially delithiated $\text{Li}_{0.4}\text{Fe}_{0.5}\text{Mn}_{0.5}\text{PO}_4$ at temperature from 25°C to 700°C and at 2θ from 15° to 45°, (b) *in-situ* XRD patterns of partially delithiated fully delithiated $\text{Li}_{0.4}\text{Fe}_{0.5}\text{Mn}_{0.5}\text{PO}_4$ at temperature from 150°C to 250°C and at 2θ from 15° to 45°, and (c) *in-situ* XRD patterns of partially delithiated fully delithiated $\text{Li}_{0.4}\text{Fe}_{0.5}\text{Mn}_{0.5}\text{PO}_4$ at temperature from 500°C to 600°C and at 2θ from 15° to 45° 110

Figure 3.3.13 (a) *in-situ* XRD patterns of fully delithiated $\text{Fe}_{0.25}\text{Mn}_{0.75}\text{PO}_4$ at temperature from 25°C to 700°C and at 2θ from 15° to 45°, (b) *in-situ* XRD patterns of fully delithiated fully delithiated $\text{Fe}_{0.25}\text{Mn}_{0.75}\text{PO}_4$ at temperature from 250°C to 400°C and at 2θ from 24° to 40°, and (c) *in-situ* XRD patterns of fully delithiated fully delithiated $\text{Fe}_{0.25}\text{Mn}_{0.75}\text{PO}_4$ at temperature from 500°C to 600°C and at 2θ from 24° to 40° 111

Figure 3.3.14 (a) *in-situ* XRD patterns of partially delithiated $\text{Li}_{0.46}\text{Fe}_{0.25}\text{Mn}_{0.75}\text{PO}_4$ at temperature from 25°C to 700°C and at 2θ from 15°

to 45°, (b) <i>in-situ</i> XRD patterns of partially delithiated fully delithiated $\text{Li}_{0.46}\text{Fe}_{0.25}\text{Mn}_{0.75}\text{PO}_4$ at temperature from 200°C to 300°C and at 2θ from 15° to 45°, and (c) <i>in-situ</i> XRD patterns of partially delithiated fully delithiated $\text{Li}_{0.46}\text{Fe}_{0.25}\text{Mn}_{0.75}\text{PO}_4$ at temperature from 500°C to 600°C and at 2θ from 15° to 45°	112
Figure 3.3.15 The phase stability map of fully delithiated $\text{Fe}_{1-x}\text{Mn}_x\text{PO}_4$ [$0 \leq x \leq 1$] as functions of temperature	113
Figure 3.3.16 The phase stability map of partially delithiated $\text{Li}_{1-y}\text{Fe}_{1-x}\text{Mn}_x\text{PO}_4$ [$0 \leq x \leq 1, y \approx 0.6$] as functions of temperature	114
Figure 4.1.1 Schematic illustration of the fabrication process of $\text{Li}_3\text{V}_2(\text{PO}_4)_3/\text{PEDOT}$ composite	131
Figure 4.1.2 XRD patterns of pristine $\text{Li}_3\text{V}_2(\text{PO}_4)_3$ (black), partially delithiated $\text{Li}_{3-x}\text{V}_2(\text{PO}_4)_3$ (red), and $\text{Li}_3\text{V}_2(\text{PO}_4)_3/\text{PEDOT}$ composite (blue)	132
Figure 4.1.3 Comparison of FT-IR between $\text{Li}_3\text{V}_2(\text{PO}_4)_3/\text{PEDOT}$ composite and pristine $\text{Li}_3\text{V}_2(\text{PO}_4)_3$	133
Figure 4.1.4 (a,b) TEM images of $\text{Li}_3\text{V}_2(\text{PO}_4)_3/\text{PEDOT}$ composite. (c-e) TEM analysis in bright-field mode (c), elemental analysis using energy-dispersive X-ray mapping (d) (V: blue, P: green, S: red), and cross-sectional composition line profiles (e) (V: blue, P: green, S: red) of $\text{Li}_3\text{V}_2(\text{PO}_4)_3/\text{PEDOT}$ composite	134

Figure 4.1.5 TGA profile of $\text{Li}_3\text{V}_2(\text{PO}_4)_3/\text{PEDOT}$ composite and pristine $\text{Li}_3\text{V}_2(\text{PO}_4)_3$	135
Figure 4.1.6 (a) Specific discharge capacities of $\text{Li}_3\text{V}_2(\text{PO}_4)_3/\text{PEDOT}$ and $\text{Li}_3\text{V}_2(\text{PO}_4)_3/\text{carbon}$ in the voltage range 2.5-4.4 V with various current rates. b) Cyclability of $\text{Li}_3\text{V}_2(\text{PO}_4)_3/\text{PEDOT}$ and $\text{Li}_3\text{V}_2(\text{PO}_4)_3/\text{carbon}$ electrode in the voltage range 2.5-4.4 V with a current rate of 10C (1C = 133 mA g ⁻¹)... 136	
Figure 5.1.1 (a) Schematic representation of alluaudite $\text{Na}_{0.67}\text{FePO}_4$ or $\text{Li}_{0.67}\text{FePO}_4$. The local geometry of the chains of edge-shared FeO_6 octahedra linked by tetrahedra PO_4 units in the alluaudite, (b) Rietveld refinements of the ND pattern of $\text{Na}_{0.67}\text{FePO}_4$ with its refined lattice parameters ($R_p = 4.15\%$, $R_I = 5.40\%$, $R_F = 2.17\%$, and $\chi^2 = 6.17\%$)	153
Figure 5.1.2 Rietveld refinements of the XRD pattern of $\text{Na}_{0.67}\text{FePO}_4$. ($R_p = 1.26\%$, $R_I = 0.78\%$, $R_F = 0.74\%$, $\chi^2 = 2.17\%$)	154
Figure 5.1.3 The XRD pattern of ion-exchanged alluaudite $\text{Li}_{0.67}\text{FePO}_4$ at harsh condition (25M LiBr in Hexanol for 48 hours at 170°C)	155
Figure 5.1.4 Rietveld refinements of the XRD pattern of alluaudite $\text{Li}_{0.67}\text{FePO}_4$ ($R_p = 4.51\%$, $R_I = 5.52\%$, $R_F = 5.86\%$, and $\chi^2 = 2.10\%$)	156
Figure 5.1.5 Simulated XRD patterns of alluaudite $\text{Li}_{0.67}\text{FePO}_4$ as a function of partial occupancy of Fe.....	157
Figure 5.1.6 Rietveld refinements of the ND pattern of alluaudite	

Li_{0.67}FePO₄ with its refined lattice parameters. ($R_p = 2.17\%$, $R_I = 3.41\%$, $R_F = 1.88\%$, $\chi^2 = 2.28\%$) 158

Figure 5.1.7 (a) XRD of fully lithiated alluaudite LiFePO₄ with its refined lattice parameters. ($R_p = 2.86\%$, $R_I = 2.39\%$, $R_F = 2.66\%$, and $\chi^2 = 2.32\%$. The blank regions between 37.7° and 39° and between 44° and 45.1° are the XRD peaks of Al foil. (b) Comparison of XRD patterns between alluaudite Li_{0.67}FePO₄ and alluaudite LiFePO₄. (c) Normalized Fe K-edge XANES spectra for alluaudite Li_xFePO₄ 159

Figure 5.1.8 (a) Galvanostatic curves of alluaudite LiFePO₄ during 25 cycles at C/20 (inset: cyclability of alluaudite LiFePO₄ during 25 cycles at C/20), (b) *ex situ* XRD patterns of *a*-Li_xFePO₄ ($0 \leq x \leq 0.8$), (c) charge profile of *a*-Li_xFePO₄ ($0 \leq x \leq 0.8$) for *ex situ* XRD, (d) discharge curves of alluaudite LiFePO₄ as a function of C rate from C/20 to 3C (charging with CCCV mode (C/20 rate and 5 hour holding at 4.5V)) 160

Chapter 1. Introduction

Exhaustion of fossil fuels and environmental problems, such as especially CO₂ emission, have provoked profound attention in renewable green energy.[1] Over several decades, many environmental-friendly energy sources have been studied extensively. As illustrated in Figure 1.1, energy generation from geothermal energy, wind energy, hydro energy, ocean energy, and solar energy to electric energy offers green energy without any air-pollution. For the effective use of the renewable energy into our society, it is indispensable to store and release the energy with high efficiency. Therefore, the development of energy storage system is the first task to use the green renewable energy. Many researchers have studied the optimal energy storage systems for a long time.

Among many candidates, lithium (Li)-ion batteries (LIB) has attracted as the most potential energy storage system in the current worldwide battery market due to their outstanding energy and power capability.[2-3] Figure 1.2 shows that LIB has bigger energy density than other energy storage system. Moreover, it has excellent energy efficiency as well as good cyclability, compared to other energy storage system. Since Sony launched the first version of commercialized in 1991, the market share of LIB is overwhelming in small and light battery market for portable electronics (e.g.,

cellular phone, digital camera, and laptop). Recently, demand for eco-friendly driving has been skyrocketed and the use of LIB has expanded from portable electronics to large scale applications, in particular, electric vehicles (EVs). The important issues of LIB as the energy storage system for EVs are production cost and safety above everything else. Unfortunately, the most widely used LIB cathode material, LiCoO_2 , is not suitable for EVs due to its high production cost and low safety, despite of its high energy/power density and excellent cycle life.

Currently, phosphate materials have been considered as the alternative material to be suitable for EVs. Polyanion in phosphate materials make their structure stable with P-O strong covalent bonding during charge/discharge as shown in Figure 1.3.[4-5] Moreover, their high theoretical capacity and potentially low production cost are attractive enough to be used as the energy storage system for large-scale applications. In this thesis, the study on the phosphates, such as olivine, NASICON, and alluaudite, are investigated for application as cathode materials for Li rechargeable battery.

Chapter 2 consists of three parts related to the study of olivine cathode materials. First part is the improvement of electrochemical performance of olivine LiMnPO_4 . Olivine LiMnPO_4 is considered as the best candidate among all olivine cathode materials due to its high redox potential ($\sim 4.1\text{V vs.}$

Li⁺/Li), low production cost, and high safety. However, the poor electrochemical performance of LiMnPO₄ in mild operation due to its sluggish kinetics is a major drawback for its commercialization.[5-11] We demonstrated that the presence of Fe and Mg in LiMnPO₄ framework provide multiple nucleation site, unlike pristine LiMnPO₄ that has only one nucleation site. Compared to pristine LiMnPO₄, the electrochemical properties of LiFe_{0.05}Mg_{0.05}Mn_{0.9}PO₄ are shown to be remarkably improved by nucleation enhancers during (de)lithiation. Second part is the study on particle size effect of thermal stability of olivine LiMnPO₄. The effect of particle size on phase stability of the delithiated phase Li_xMnPO₄ was investigated using temperature-controlled *in situ* XRD. Due to the sluggish kinetics, nano-sizing is essential to use olivine LiMnPO₄ as the cathode material for Li rechargeable battery in mild operation condition,[12, 13] thus the study of the thermal characteristic of the nano-size LiMnPO₄ becomes more important. This study reports that the Li_xMnPO₄ of small particle size (~50 nm) undergoes phase transformation into Mn₃(PO₄)₂ with an amorphous P-rich phase in contrast to that of large particle size (from 200nm to 1μm). The third part is the study on thermal stability of binary olivine LiFe_{1-x}Mn_xPO₄ ($x = 0, 0.25, 0.5, 0.75, \text{ and } 1$) using temperature controlled *in situ* XRD. To counterbalance high rate-capability and cyclability of LiFePO₄

and high voltage of LiMnPO_4 , binary olivine $\text{LiFe}_{1-x}\text{Mn}_x\text{PO}_4$ has attracted as the most potential cathode materials of Li rechargeable battery for large-scale application such as EVs.[6, 14-15] Recent works have shown that the electrochemical properties of binary $\text{LiFe}_{1-x}\text{Mn}_x\text{PO}_4$ cathodes are sensitively dependent on the Fe/Mn ratio in the material.[14-17] Therefore, we supposed that Fe/Mn ratio in binary $\text{LiFe}_{1-x}\text{Mn}_x\text{PO}_4$ may influence the thermal stability of binary $\text{LiFe}_{1-x}\text{Mn}_x\text{PO}_4$. Since the safety and stability of the battery is strongly influenced by the phase stability of the cathode at different SOC's and temperatures, this work can provide useful information in determining the optimal composition of binary $\text{LiFe}_{1-x}\text{Mn}_x\text{PO}_4$ cathodes.

In chapter 3, $\text{Li}_3\text{V}_2(\text{PO}_4)_3$ /conducting polymer composite is successfully fabricated to improve the electrochemical performance of $\text{Li}_3\text{V}_2(\text{PO}_4)_3$. monoclinic $\text{Li}_3\text{V}_2(\text{PO}_4)_3$ has much attraction as a prospective candidate for use as the potential cathode material in lithium ion batteries due to the high thermal stability induced by strong P-O bonds and three-dimensional solid framework in polyanion $(\text{PO}_4)^{3-}$, higher redox potential, and its two independent lithium sites with a high theoretical capacities.[18-21] However, the low electrical conductivity of monoclinic $\text{Li}_3\text{V}_2(\text{PO}_4)_3$ ($2.4 \times 10^{-7} \text{ S cm}^{-1}$ at 25°C) was a major drawback for its high current-rate performance.[18, 20] In the past few years, carbon-coating were usually used for improvement of the

low conductivity.[22,23] However, this carbon-coating is formed at high temperature in an inert or reducing atmosphere and accompanies the formation of non-environmental friendly products such as volatile organic compounds, CO, and CO₂. Conductive polymers are attractive materials in covering crystallite surfaces in terms of improving not only mechanical flexibility but also electrical conductivity to improve Li ions diffusion.[24,25] Also, they can be coated under mild processing conditions such as low temperature synthesis to prevent formations of harmful gases, compared to the carbon coating using organic compound. [26] As inspired this, we fabricate the Li₃V₂(PO₄)₃ composite with the conducting polymer, poly(3,4-ethylene-dioxythiophene) (=PEDOT) for highly improved electrochemical performances. PEDOT coating has significantly improved rate capability and cyclability without any conductive carbon, compared to pristine Li₃V₂(PO₄)₃ mixed with conductive carbon.

In chapter 4, novel non-olivine LiFePO₄ with an alluaudite structure was successfully prepared, and its structure was investigated in detail through combined Neutron diffraction and X-ray diffraction analyses. Alluaudite compounds have the general formula X(1)X(2)M(1)M(2)₂(PO₄)₃, in which X and M are different cation species.[27] The structure is comprised of infinite chains of edge-sharing M(2)O₆ octahedra, linked by distorted M(1)O₆

octahedra. M(1) and M(2) are occupied by Fe, and X(1) and X(2) are filled with either Na or Li in the targeted structure. We attempted to prepare a novel $\text{Na}_2\text{Fe}_3(\text{PO}_4)_3$ ($= \text{Na}_{0.67}\text{FePO}_4$), as a starting material for the alluaudite LiFePO_4 . Hatert *et al.* reported that the alluaudite structure had three additional sites in which cations can be inserted and extracted.[28] These sites are located in the channels at crystallographic positions that are different from those of the X(1) and X(2) sites, implying the feasibility of further insertion of cations into the channel.[28] Also, the presence of Fe^{3+} in the alluaudite structure enables the additional Li^+ or Na^+ ions to be intercalated.[29, 30] Therefore, we supposed that alluaudite LiFePO_4 could be synthesized from $\text{Na}_{0.67}\text{FePO}_4$ using the ion-exchange from Na to Li and an additional lithiation process. Almost all of the lithium ions in alluaudite LiFePO_4 could be reversibly extracted and inserted at a reasonably fast rate, qualifying it as another possible iron-based cathode for Li rechargeable batteries. The electrochemical and structure information of alluaudite LiFePO_4 was compared with those of well-known olivine LiFePO_4 and remarkable difference between alluaudite LiFePO_4 and olivine LiFePO_4 was observed in many experiments.

This thesis deals with the various phosphate materials such as olivine, NASICON, and alluaudite by using various experiments. We believe that

this thesis can provide the fundamental study of phosphate electrode to be used as the new-generation cathode material of Li rechargeable battery for large-scale applications.

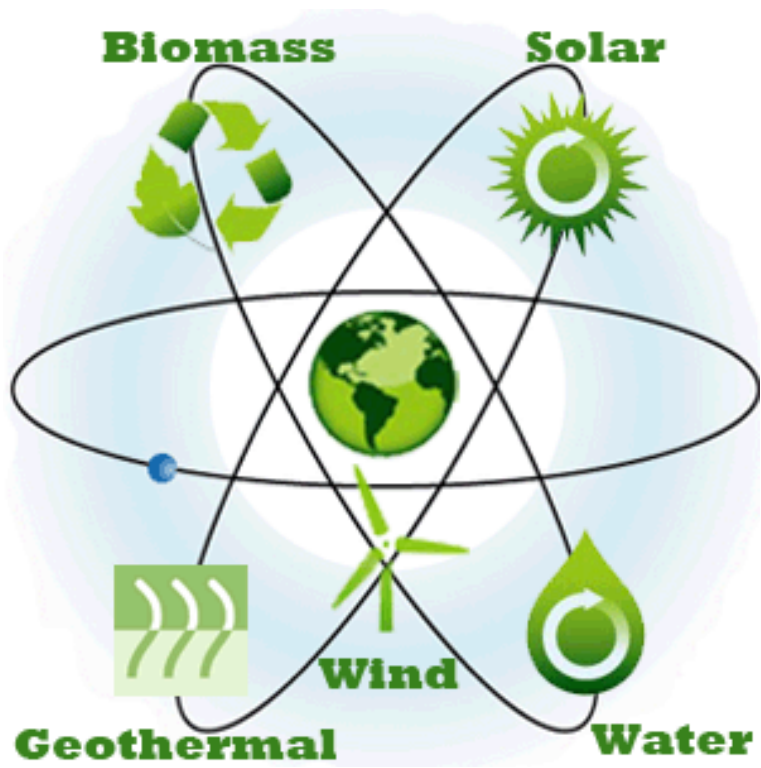


Figure 1.1 Renewable energy sources

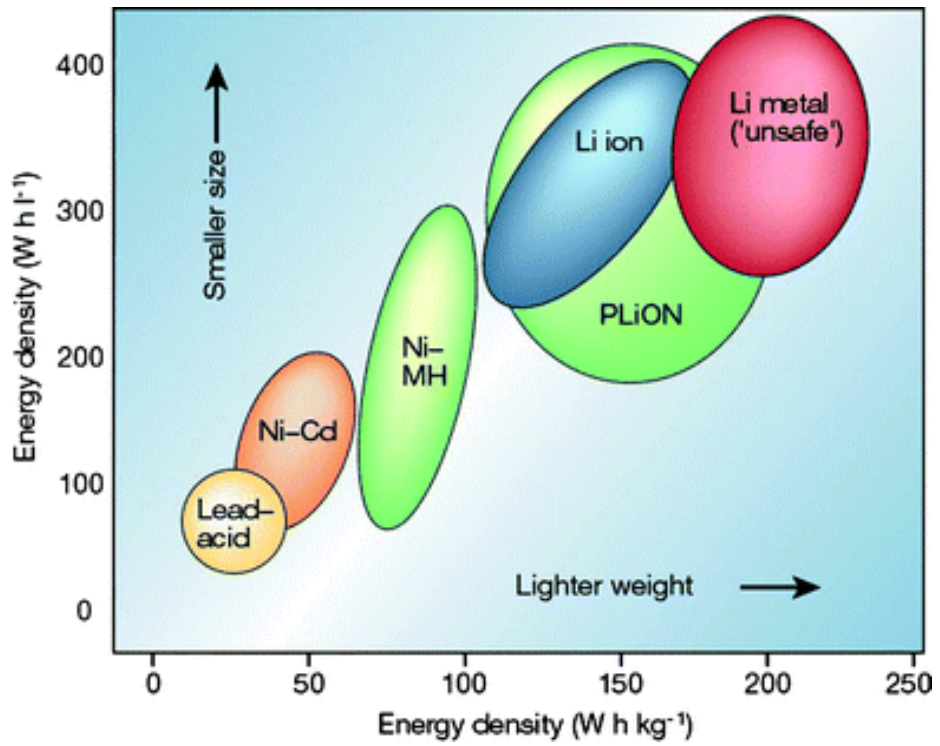


Figure 1.2 Comparison of various battery systems[2]

1.1 Reference

- [1] I. Dincer, *Renew. Sust. Energy Rev.*, **4**, 157 (2000).
- [2] J. -M. Tarascon and M. Armand, *Nature*, **414**, 359 (2001).
- [3] M. Armand and J. -M. Tarascon, *Nature*, **451**, 652 (2008).
- [4] S. Y. Chung, J. T. Bloking and Y. M. Chiang, *Nat. Mater.*, **1**, 123-128 (2002).
- [5] A. K. Padhi, K. S. Nanjundaswamy, C. Masquelier, S. Okada and J. B. Goodenough, *J. Electrochem. Soc.*, **144**, 1609-1613 (1997).
- [6] M. Yonemura, A. Yamada, Y. Takei, N. Sonoyama, and R. Kanno, *J. Electrochem. Soc.*, **151**, A1352 (2004)
- [7] A. Yamada, M. Hosoya, S.-C. Chung, Y. Kudo, K. Hinokuma, K.-Y. Liu, and Y. Nishi, *J. Power Sources*, **119–121**, 232 (2003).
- [8] F. Zhou, M. Cococcioni, K. Kang, and G. Ceder, *Electrochem. Commun.*, **6**, 1144 (2004).
- [9] C. Delacourt, L. Laffont, R. Bouchet, C. Wurm, J. B. Leriche, M. Morcrette, J. M. Tarascon, and C. Masquelier, *J. Electrochem. Soc.*, **152**, A913 (2005).
- [10] G. H. Li, H. Azuma, and M. Tohda, *Electrochem. Solid-State Lett.*, **5**, A135 (2002).
- [11] D. W. Choi, D. H. Wang, I. T. Bae, J. Xiao, Z. M. Nie, W. Wang, V. V.

- Viswanathan, Y. J. Lee, J. G. Zhang, G. L. Graff, et al., *Nano Lett.*, **10**, 2799 (2010).
- [12] R. Malik, D. Burch, M. Bazant, and G. Ceder, *Nano Lett.*, **10**, 4123 (2011).
- [13] T. Drezen, N.-H. Kwon, P. Bowen, I. Teerlinck, M. Isono, and I. Exnar, *J. Power Source*, **174**, 949-953 (2007).
- [14] A. Yamada, Y. Kudo and K. Y. Liu, *J. Electrochem. Soc.*, **148**, A747-A754 (2001).
- [15] K. Saravanan, J. J. Vittal, M. V. Reddy, B. V. R. Chowdari and P. Balaya, *J. Solid State Electrochem.*, **14**, 1755-1760 (2010).
- [16] S. M. Oh, H. G. Jung, C. S. Yoon, S. T. Myung, Z. H. Chen, K. Amine and Y. K. Sun, *J. Power Sources*, **196**, 6924-6928 (2011).
- [17] B. Zhang, X. J. Wang, H. Li and X. J. Huang, *J. Power Sources*, **196**, 6992-6996 (2011).
- [18] H. Huang , S. C. Yin , T. Kerr , N. Taylor , L. F. Nazar , *Adv. Mater.*, **14**, 1525 (2002).
- [19] M. M. Ren , Z. Zhou , X. P. Gao , W. X. Peng , J. P. Wei , *J. Phys. Chem. C*, **112**, 5689-5693 (2008).
- [20] H. D. Liu , P. Gao , J. H. Fang , G. Yang , *Chem. Commun.*, **47**, 9110-9112 (2011) .

- [21] A. R. Cho, J. N. Son, V. Aravindan, H. Kim, K. S. Kang, W. S. Yoon, W. S. Kim, Y. S. Lee, *J. Mater. Chem.*, **22**, 6556-6560 (2012) .
- [22] Y.-U. Park, J. Kim, H. Gwon, D. H. Seo, S. W. Kim, K. Kang, *Chem. Mater.*, **22** , 2573-2581 (2010) .
- [23] C. M. Doherty, R. A. Caruso, B. M. Smarsly, P. Adelhelm, C. J. Drummond, *Chem. Mater.*, **21**, 5300-5306 (2009).
- [24] A. V. Murugan , T. Muraliganth , A. Manthiram , *Electrochem. Commun.*, **10**, 903-906 (2008).
- [25] K. S. Park, S. B. Schougaard, J. B. Goodenough, *Adv. Mater.*, **19**, 848-851 (2007).
- [26] D. Lepage, C. Michot, G. X. Liang, M. Gauthier, S. B. Schougaard, *Angew. Chem. Int. Ed.*, **50** , 6884-6887 (2011).
- [27] P. B. Moore, *Am. Mineral.*, **56**, 1955-1975 (1971).
- [28] F. Hatert, P. Keller, F. Lissner, D. Antenucci and A. M. Franolet, *Eur. J. Mineral.*, **12**, 847-857 (2000).
- [29] K. Trad, D. Carlier, L. Croguennec, A. Wattiaux, M. B. Amara and C. Delmas, *Chem. Mater.*, **22**, 5554-5562 (2010).
- [30] K. Trad, D. Carlier, L. Croguennec, A. Wattiaux, M. B. Amara and C. Delmas, *Inorg. Chem.*, **49**, 10378-10389 (2010).

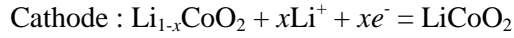
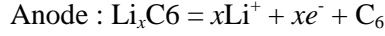
Chapter 2. General Background

2.1 Lithium rechargeable battery

Li rechargeable battery defines a transducer that converts electrical energy into chemical energy and *vice versa*. Due to the best energy densities, no memory effect, and negligible loss of the charge while it is not in use, Li rechargeable battery has been widely used as the energy storage system for portable electronics.[1] However, its common electrochemical performance in high current rate, high production cost, and considerable safety problems have considered the drawbacks for the bulk energy storage system of large-scale applications such as electric vehicles.

Figure 2.1.1 explains the basic operation principles of Li rechargeable battery. It consists of an anode, a cathode, and an electrolyte. During charge, the Li ions are extracted from the cathode through electrolyte, while Li ions are inserted into the anode, thus energy is stored in the Li recharge battery. During discharge, the Li ions are extracted from the anode through electrolyte, while Li ions are inserted into the cathode, thus energy is released from the Li recharge battery. Meanwhile, the electrolyte also provides for the only ionic transport without any electronic transport. The electrochemical reaction mechanism in conventional Li rechargeable battery that consist of graphite (as the anode) and LiCoO_2 (as the cathode) is

explained as follow.



The operation voltage is determined by the difference of chemical potential between anode and cathode as written by

$$V = -(\mu_{\text{Li}}^{\text{Cathode}} - \mu_{\text{Li}}^{\text{anode}})/nF$$

Where V is operation voltage, μ_{Li} is chemical potential of cathode and anode, n is number of electrons, and F is Faraday's constant. For a high energy density,[2, 3] large gap of chemical potential between anode and cathode is essential. Therefore, the materials widely used as the anode material for Li rechargeable battery have high chemical potential, such as Li metal, Li-alloying compounds, and Li-conversion compounds. Cathode needs low chemical potential, thus transition metal oxides, compounds containing transition metal and polyanion such as phosphate, silicate, and sulfate have been considered as the optimal cathode materials for Li rechargeable battery.

2.2 Phosphate Electrode

2.2.1 Olivine Electrode

The lithium transition metal phosphate LiMPO_4 ($M = \text{Fe, Mn, Co, Ni}$) with olivine structure has been highlighted as the best candidate of cathode materials for EVs due to its remarkable stability in harsh operating conditions, non-toxicity, and potentially low production cost.[4, 5] Figure 2.2.1 shows the structure of olivine. Transition metal (M) ions exist at octahedral sites and these octahedra MO_6 are corner-sharing with three tetrahedra PO_4 and edge-sharing with one PO_4 . M ions in MO_6 are slightly shifted toward opposite side of edge-shared PO_4 because of the electrostatic repulsion between M ion and P ion. Li ions form linear chains of edge sharing octahedra along the b axis. Along the one-dimensional channel, Li ions diffuse from the octahedral site to adjacent octahedral site through intermediate tetrahedral site.[6-8]

LiFePO_4 , proposed by Goodenough et al. in 1997,[5] has been attracted as the best candidate of cathode material for large-scale application. This material is the first cathode material with potentially low production cost by naturally abundant Fe , non-toxicity, environmentally benign, and high safety by high structural stability due to strong P-O covalent bonds that could have a major impact in electrochemical energy storage. For LiFePO_4 , the discharge potential is about $\sim 3.4\text{V}$ vs. Li^+/Li and no obvious capacity fading was

observed even after several hundred cycles.[9-11] Its capacity approaches 170 mAh g⁻¹, higher than that obtained by LiCoO₂ and comparable to stabilized LiNiO₂, and moreover, it is very stable during discharge/recharge. Since its discovery, many research groups have tried to improve the performance of this material. Since this material has a low conductivity at room temperature (10⁻⁹ S cm⁻² at 25°C), the methods to improve the conductivity of LiFePO₄ was extensively studied over several decades. The first suggested method is carbon coating. Many researches showed that carbon coating significantly improve the electrochemical performance of LiFePO₄. [12-14] Another approach to improve the properties of LiFePO₄ is aliovalent doping. Chang *et al.* showed remarkably improved electrochemical performance of LiFePO₄ when small amount of elements such as Mg²⁺, Al³⁺, Ti⁴⁺, Zr⁴⁺, Nb⁵⁺ and W⁶⁺ was doped into the structure.[4] Also, surface coating was known to be able to improve the electrochemical performance of LiFePO₄. Ceder *et al.* showed ultrafast charging and discharging of LiFePO₄ by creating a fast ion-conducting surface phase through controlled off-stoichiometry.[9] Surprisingly, this modified LiFePO₄ showed power capability of 170kW kg⁻¹ at a 400C rate and 90kW kg⁻¹ at a 200C rate. (1C = 180mA g⁻¹). However, its low operation voltage (~3.4V) is relative lower than other commercial cathode materials for Li rechargeable battery, thus the energy density of

LiFePO₄ is also low. Therefore, intensive research has been focused on new olivine electrode materials that have a high energy density.

LiMnPO₄ is considered to be the best candidate among all olivine cathode materials due to the Mn²⁺/Mn³⁺ redox potential of ~4.1 V vs. Li⁺/Li, which is higher than the Fe³⁺/Fe²⁺ redox potential of LiFePO₄; it is suitable for the electrolytes that are presently used in Li rechargeable batteries, and it is low in cost and high in safety.[15-17] However, the sluggish kinetics of Li diffusion in LiMnPO₄ is major drawback for its utilization. Several researchers reported that homogeneous carbon coating can improve the electrochemical performance of LiMnPO₄. Li *et al.* successfully demonstrated reversible lithiation and delithiation from carbon coated LiMnPO₄ composite cathodes, in which 9.8wt% carbon was homogeneously mixed by a solid state route followed by ball milling.[18] Also, Exnar *et al.* reported that uniformly carbon coated LiMnPO₄ nanoparticle by polyol method can have significantly improved electrochemical performance compared to pristine LiMnPO₄. [17]

LiCoPO₄ has even higher redox potential (~4.8V vs. Li⁺/Li) and higher energy density than LiFePO₄ and LiMnPO₄. However, too high operation voltage of LiCoPO₄ is not suitable for the electrolyte that is presently used in Li rechargeable battery and the high production cost of LiCoPO₄ is a critical problem for the commercialization.[19] Moreover, LiCoPO₄ has poor

structural stability even at low temperature near 100°C.[20]

2.2.2 NASICON Electrode

The general formula of NASICON (Na Super Ionic Conductor) structure is $A_3MM'(PO_4)_3$. The high structural stability induced by strong P-O covalent bonding in PO_4 tetrahedra ensures the safety of NASICON in harsh condition. Among many NASICON materials, $Li_3V_2(PO_4)_3$ was considered as a prospective candidate for use as the cathode in LIBs due to its overwhelming advantages, such as having the highest theoretical capacity (197mAh g^{-1}) among the various phosphate based polyanion framework materials.[21-24] $Li_3V_2(PO_4)_3$ exhibits two different frameworks, the rhombohedral phase and the monoclinic phase.[25-26]

As shown in Figure 2.2.2(a), the rhombohedral $Li_3V_2(PO_4)_3$ is formed from corner-sharing PO_4 tetrahedra and VO_6 octahedra that create the ‘lantern’ units, which are assembled into a three-dimensional $[V_2(PO_4)_3]$ framework. This material shows that 2 Li^+ ions in a single tetrahedrally coordinated site are deintercalated from the structure at $\sim 3.8\text{V}$ vs. Li^+/Li and is only accessible *via* ion-exchange of the corresponding sodium phase $Na_3V_2(PO_4)_3$.[26]

The monoclinic $Li_3V_2(PO_4)_3$ has the three-dimensional network which consist of slightly distorted vanadium octahedra (VO_6) and phosphorus tetrahedra (PO_4) linked together via oxygen to form a (M-O-P-O) bonding arrangement, as shown in Figure 2.2.2(b) So-called “lantern’ unit $V_2P_3O_{12}$ are

alternately oriented perpendicular to other units, thus monoclinic phase create a closer packing than rhombohedral phase.[21] Monoclinic $\text{Li}_3\text{V}_2(\text{PO}_4)_3$ has been considered as an attractive cathode material for LIBs, because an average 4.0 V extraction/reinsertion voltage can be obtained between 3.0 and 4.3 V as well as high theoretical capacities ($\sim 133\text{mAh g}^{-1}$).[21-24] However, the intrinsic low electric conductivity is a major drawback to limit its high electrochemical performance.[21, 23] Many research groups have tried to improve the performance of this material. Nazar *et al.* reported that nanostructured composite monoclinic $\text{Li}_3\text{V}_2(\text{PO}_4)_3/\text{carbon}$ showed a significantly improved high specific capacity, even when cycled at high current rate 5C ($1\text{C} = 133\text{mA g}^{-1}$). At a rate of 5C, 95% theoretical capacity is still achieved.[21] Also, Yang *et al.* reported that the $\text{Li}_3\text{V}_2(\text{PO}_4)_3/\text{graphene}$ nanocomposite showed significantly improved electrochemical performance compared to pristine $\text{Li}_3\text{V}_2(\text{PO}_4)_3$, because minor amount of graphene sheets form an electronic conducting network. When operated at 5C and 20C discharge rates ($1\text{C} = 133\text{mA g}^{-1}$), the specific discharge capacities are 118mAh g^{-1} and 109mAh g^{-1} (89% and 82% of the ideal capacity), respectively [23]

2.2.3 Alluaudite Electrode

As shown in Figure 2.2.3, the natural alluaudite crystal structure determined by Moore in 1971 has monoclinic $C2/c$ space group and the general structural formula $X_2X_1M_1M_2_2(PO_4)_3$, in which X and M cations are written according to decreasing size.[27] The structure consists of infinite chains formed by a succession of M2 octahedral pairs linked by highly distorted M1 octahedra. Equivalent chains are connected by phosphate tetrahedra to form sheets oriented perpendicular to [010] direction. Equivalent sheets are hold together by PO_4 tetrahedra to form a three-dimensional architecture with two sets of tunnels in the c direction. More recent structural refinement of the alluaudite structure clearly demonstrates the existence of three cationic sites that were not reported by Moore (1971). These sites are located in the channels at crystallographic positions which are different from those of the X1 and X2 sites. Based on detailed structural studies, Hatert *et al.* proposed a new general formula, $(A_2A_2')(A_1A_1'A_12'')M_1M_2_2(PO_4)_3$, for alluaudite-type compounds. [28] Whereas the M sites must be filled, the A sites in the tunnels could be empty or partially occupied. Over several decades, several alluaudite compounds were reported.

In 2002, Richardson *et al.* firstly reported that alluaudite materials ($NaFe_3(PO_4)_3$ and $Li_xNa_{2-x}FeMn_2(PO_4)_3$) could be used as the cathode material

for Li rechargeable battery. However, their reversible capacities appear to be very limited.[29] After that, Delmas *et al.* proposed that alluaudite $\text{NaMnFe}_2(\text{PO}_4)_3$ ($=(\text{Na}_{0.81})_{\text{A}1}(\text{Na}_{0.19})_{\text{A}2}(\text{Mn}^{2+}_{0.87}\text{Fe}^{2+}_{0.13})_{\text{M}1}(\text{Fe}^{3+}_{1.87}\text{Mn}^{3+}_{0.13})_{\text{M}2}(\text{PO}_4)_3$.) could be possible to use as the positive electrode in Li and Na rechargeable batteries. The iron manganese sodium phosphate $\text{NaMn}^{2+}\text{Fe}^{3+}_2(\text{PO}_4)_3$ has a theoretical total capacity close to that of LiFePO_4 ($\sim 170\text{mAh g}^{-1}$) if it could be cycled between the end members $\text{Mn}^{3+}\text{Fe}^{3+}_2(\text{PO}_4)_3$ and $\text{Na}(\text{Na},\text{Li})_2\text{Mn}^{2+}\text{Fe}^{2+}_2(\text{PO}_4)_3$. Approximately 1.5Li^+ ions could be intercalated during the first discharge with an average voltage around $\sim 2.5\text{V}$ and about 1.2Li^+ ions could be extracted during the following charge from 1.5V to 4.5V . [30, 31]

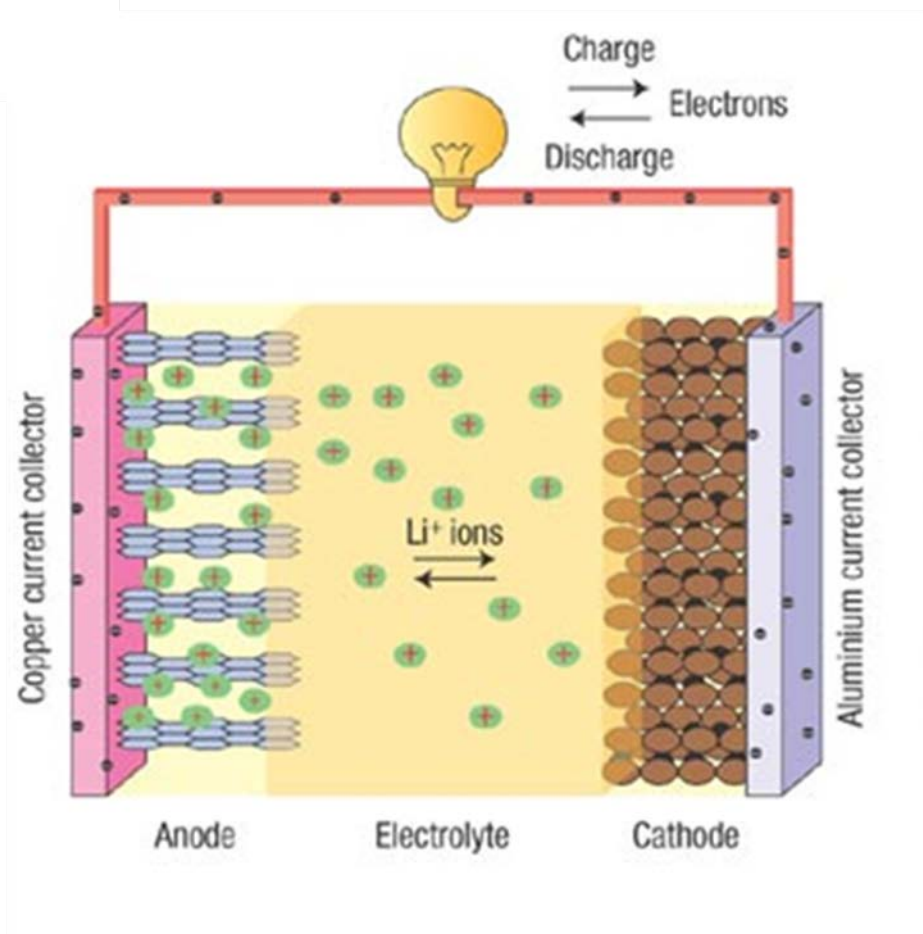


Figure 2.1.1. Cell structure and principles of Li rechargeable Battery. The charge and discharge cycles are achieved through the exchange of lithium ions between the positive and negative electrodes.

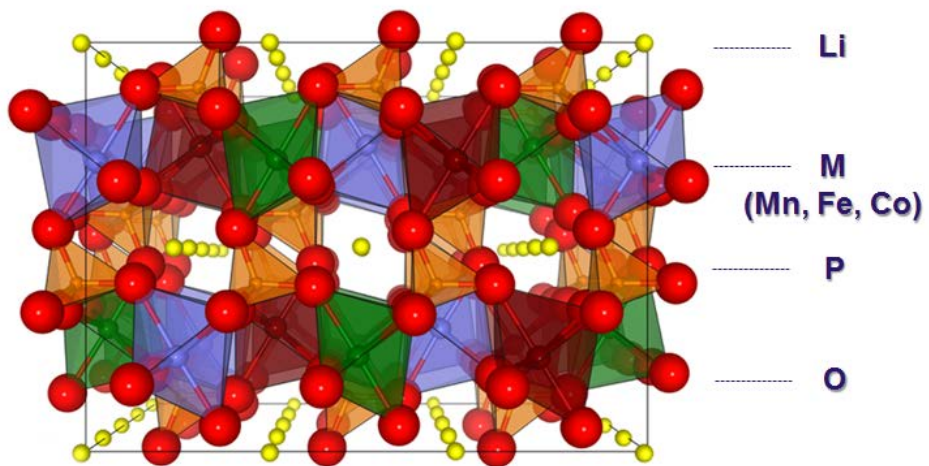


Figure 2.2.1. Structures of Olivine LiMPO_4 (M = Fe, Mn, Co, Ni)

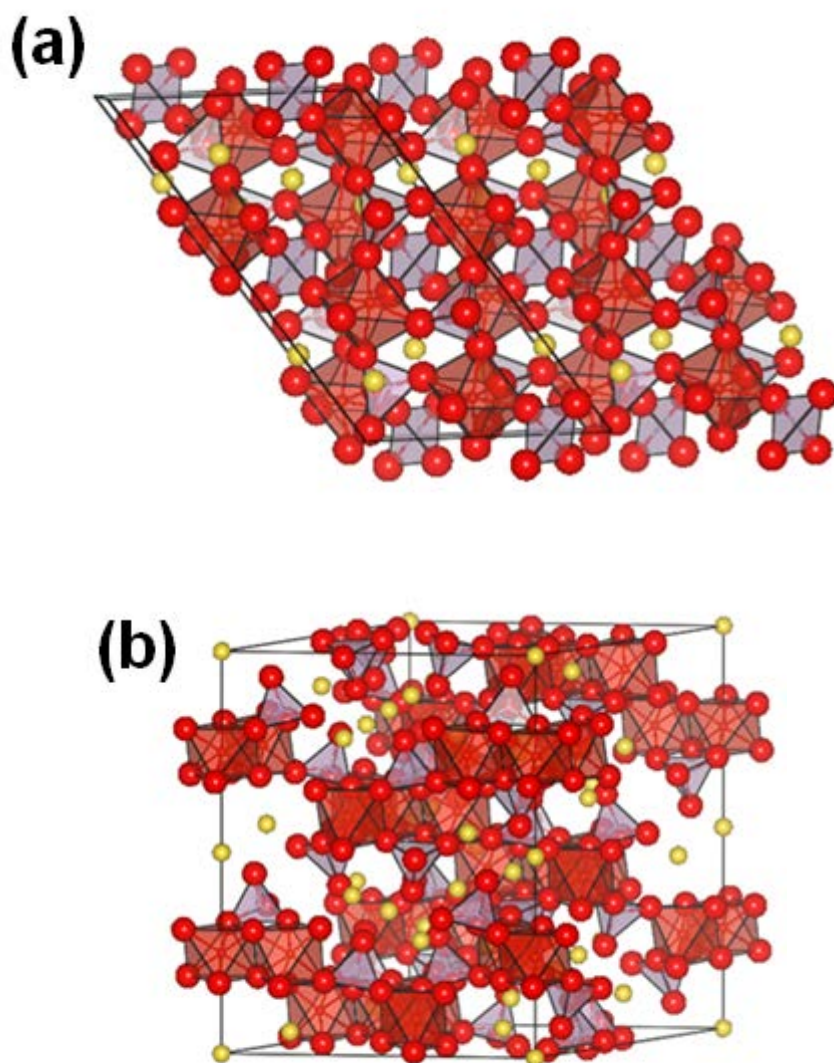


Figure 2.2.2. Structures of (a) Rhombohedral $\text{Li}_3\text{V}_2(\text{PO}_4)_3$ and (b) Monoclinic $\text{Li}_3\text{V}_2(\text{PO}_4)_3$.

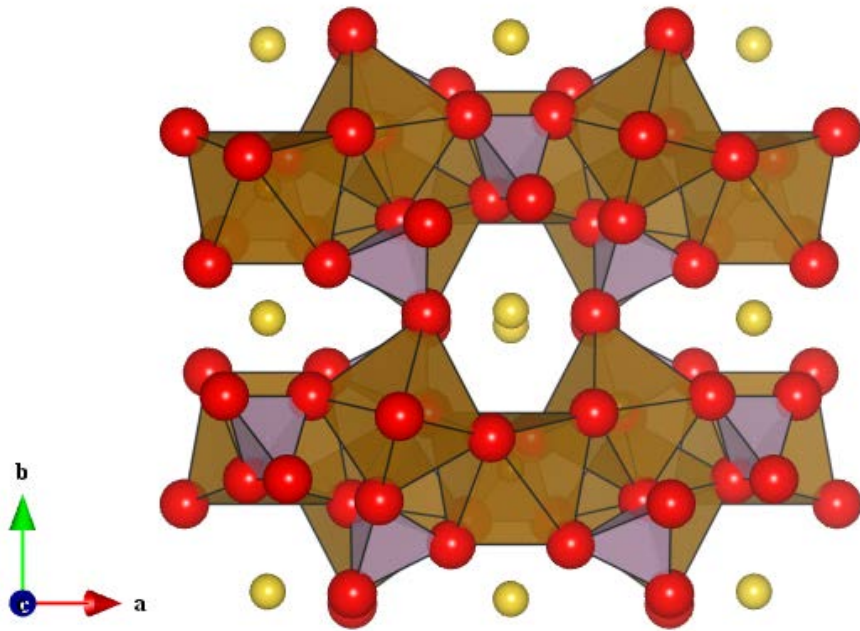


Figure 2.2.3. General alluaudite structure.

2.3 Reference

- [1] T. Sasaki, Y. Ukyo, and P. Novak, *Nat. Mater.*, **12**, 569-575 (2013)
- [2] R. A. Huggins, *Advanced Battery: Materials Science Aspects*, Springer, New York (2009)
- [3] K. Kang, *Ph. D. Thesis*, Massachusetts Institute of Technology (2006).
- [4] S. Y. Chung, J. T. Bloking and Y. M. Chiang, *Nat. Mater.*, **1**, 123-128 (2002).
- [5] A. K. Padhi, K. S. Nanjundaswamy, C. Masquelier, S. Okada and J. B. Goodenough, *J. Electrochem. Soc.*, **144**, 1609-1613 (1997).
- [6] D. Morgan, A. Van der Ven, and G. Ceder, *Electrochem. Solid State Lett.*, **7**, A30 (2004)
- [7] S. Nishimura, G. Kobayashi, K. Ohoyama, R. Kanno, M. Yashima, and A. Yamada, *Nat. Mater.*, **7**, 707 (2008)
- [8] M. S. Islam, D. J. Driscoll, C. A. J. Fisher, and P. R. Slater, *Chem. Mater.*, **17**, 5085 (2005).
- [9] B. Kang and G. Ceder, *Nature*, **458**, 190 (2009).
- [10] J. M. Tarascon and M. Armand, *Nature*, **414**, 359 (2001).
- [11] S. Y. Chung, J. T. Bloking, and Y. M. Chiang, *Nat. Mater.*, **1**, 123 (2002)
- [12] Y. G. Wang, Y. R. Wang, E. J. Hosono, K. X. Wang and H. S. Zhou,

Angew. Chem., **47**, 7461-7465 (2008).

[13] C. M. Doherty, R. A. Caruso, B. M. Smarsly, P. Adelhelm, and C. J. Drummond, *Chem. Mater.*, **21**, 530-5306 (2009)

[14] P. P. Prosini, D. Zane, and M. Pasquali, *Electrochim. Acta*, **46**, 3517-3523 (2001)

[15] T. Drezen, N. H. Kwon, P. Bowen, I. Teerlinck, M. Isono, I. Exnar, *J. Power Sources*, **174**, 949-953 (2007).

[16] M. Yonemura, A. Yamada, Y. Takei, N. Sonoyama, R. Kanno, *J. Electrochem. Soc.*, **151**, A1352-A1356 (2004)

[17] S. K. Martha, B. Markovsky, J. Grinblat, Y. Gofer, O. Haik, E. Zinigrad, D. Aurbach, T. Drezen, D. Wang, G. Deghenghi, I. Exnar, *J. Electrochem. Soc.*, **156**, A541-A552 (2009).

[18] G. H. Li, H. Azuma, M. Tohda, *Electrochem. Solid State Lett.*, **5**, A135-A137 (2002).

[19] K. Amine, H. Yasuda, and M. Yamachi, *Electrochem. Solid State Lett.*, **3**, 178 (2000).

[20] N. N. Bramnik, K. Nikolowski, D. M. Trots, and H. Ehrenberg, *Electrochem. Solid State Lett.*, **11**, A89 (2008).

[21] H. Huang, S. C. Yin, T. Kerr, N. Taylor, L. F. Nazar, *Adv. Mater.*, **14**, 1525 (2002).

- [22] M. M. Ren, Z. Zhou, X. P. Gao, W. X. Peng, J. P. Wei, *J. Phys. Chem.C*, **112**, 5689-5693 (2008).
- [23] H. D. Liu, P. Gao, J. H. Fang, G. Yang, *Chem. Commun.*, **47**, 9110- 9112 (2011).
- [24] A. R. Cho, J. N. Son, V. Aravindan, H. Kim, K. S. Kang, W. S. Yoon, W. S. Kim, Y. S. Lee, *J. Mater. Chem.*, **22** , 6556-6560 (2012).
- [25] S.-C. Yin, H. Grondy, P. Strobel, M. Anne, and L. F. Nazar, *J. Am. Chem. Soc.*, **125**, 10402-10411 (2003).
- [26] J. Gaubicher, C. Wurm, G. Goward, C. Masquelier, and L. Nazar, *Chem. Mater.*, **12**, 3240-3242 (2000).
- [27] P. B. Moore, *Am. Mineral.*, **56**, 1955-1975 (1971).
- [28] F. Hatert, P. Keller, F. Lissner, D. Antenucci and A. M. Franolet, *Eur. J. Mineral.*, **12**, 847-857 (2000).
- [29] T. J. Richardson, *J. Power Sources*, **119**, 262-265 (2003).
- [30] K. Trad, D. Carlier, L. Croguennec, A. Wattiaux, M. B. Amara and C. Delmas, *Chem. Mater.*, **22**, 5554-5562 (2010).
- [31] K. Trad, D. Carlier, L. Croguennec, A. Wattiaux, M. B. Amara and C. Delmas, *Inorg. Chem.*, **49**, 10378-10389 (2010).

Chapter 3. Olivine Electrode

3.1 Nucleation enhancer for high power Mn based olivine cathode materials

3.1.1 Research Background

Olivine LiMPO_4 ($M = \text{Fe, Mn, Co, Ni}$) have been highlighted as potential cathode materials owing to their relatively high structural stability and high theoretical capacity ($\sim 170 \text{ mAh g}^{-1}$). [1-3] Among olivine structure materials, LiFePO_4 has been extensively studied as the potential cathode on the basis of its numerous appealing features such as potentially low cost and safety. [4-9] However, due to the intrinsic problem of low energy density resulting from a low $\text{Fe}^{2+}/\text{Fe}^{3+}$ redox potential of *ca.* 3.4V, new attention has been directed to LiMnPO_4 , which offers an operating potential of $\text{Mn}^{2+}/\text{Mn}^{3+}$ redox potential of *ca.* 4.1V. [2,10-14] Because the operating voltage of LiMnPO_4 is similar to that of LiCoO_2 , presently the most widely used cathode, it is anticipated that replacement of the cathode with this material can be accomplished without major difficulties at the battery system level. Also, the availability of Mn in nature corresponds with that of Fe. Therefore, intensive research efforts have been focused on this material. [13-30] However, despite these promising aspects, the inferior kinetic property of LiMnPO_4 remains a major obstacle toward its application. As a result, the theoretical electrochemical properties

of LiMnPO₄ have yet to be achieved, even under mild operation conditions.

Recently, our group demonstrated that the power capability of LiFe_{0.05}Co_{0.05}Mn_{0.9}PO₄ can be significantly improved over pristine LiMnPO₄ due to the role of Co and Fe in the structure.[15] In the present work, we further show that small amounts of co-doping of Fe-Mg can also serve as a nucleation enhancer in LiMnPO₄ framework. Unfavorable Fe³⁺-Mn²⁺ pairs during charging and unfavorable Mg²⁺-Mn³⁺ pairs during discharging can make Mn²⁺/Mn³⁺ transition more facile promoting the nucleation of the second phase. Compared to pristine LiMnPO₄, the electrochemical properties of LiFe_{0.05}Mg_{0.05}Mn_{0.9}PO₄ are shown to be remarkably improved by nucleation enhancers during (de)lithiation.

3.1.2 Experimental Section

LiMnPO₄ and LiFe_{0.05}Mg_{0.05}Mn_{0.9}PO₄ samples were prepared through a sol-gel synthesis. A stoichiometric amount of Li(CH₃COO)·2H₂O, Mn(CH₃COO)₂, Fe(CH₃COO)₂, Mg(CH₃COO)₂·4H₂O, and NH₄H₂PO₄ precursors was dissolved in deionized water with glycolic acid and HNO₃ to form the sol state. This solution was heated to 70°C for 12 h. The precursors were then fired at 350°C under an Ar condition for 3 h, reground, and manually pelletized. After preheating, we calcined the pellet at 520°C under an Ar condition for 3 h.

For the electrochemical characterization, the active materials were dry-ballmilled with 20wt % carbon black (Super-P) for 24 h. A slurry of 80wt% carbon-coated LiMnPO_4 and $\text{LiFe}_{0.05}\text{Mg}_{0.05}\text{Mn}_{0.9}\text{PO}_4$, 11wt% carbon black (Super-P), and 9wt% polyvinylidene fluoride dispersed in N-methyl-2-pyrrolidone (NMP) was prepared and cast on aluminum foil. NMP was evaporated at 70°C for 12h. Electrochemical cells were assembled in a CR2016 type coin cell with a Li counter electrode, separator (Celgard 2400), and 1M LiPF_6 electrolyte in a mixture of 1:1 ethyl carbonate/dimethyl carbonate in an Ar-filled glove box. The charge/discharge test was performed using a potentiostatgalvanostat (WonA Tech). Partially delithiated samples were prepared by carefully retrieving the electrode from coin cells at different charge states. The electrodes were washed with dimethyl carbonate and dried in a vacuum before being used in X-ray diffraction (XRD, Rigaku D/Max 2500) analyses. In the potentiostatic intermittent titration technique (PITT) measurements, a “staircase” voltage profile was used in which the cell voltage was raised in 5mV increments. The current versus time, $I(t)$, was measured at constant potential at 0.05-0.2 s intervals depending on the rate of current decay. Each individual titration was terminated when the absolute current reached a C/50 rate.

3.1.3 Results and Discussion

A schematic picture of proposed (de)lithiation mechanism in the olivine system doped with nucleation enhancers is illustrated in Figure 3.1.1.[15] When small amounts of Fe and Mg are substituted in Mn sites, the initial delithiation occurs by the oxidation of Fe^{2+} to Fe^{3+} because of the lower $\text{Fe}^{2+}/\text{Fe}^{3+}$ redox potential (~ 3.4 V) relative to the $\text{Mn}^{2+}/\text{Mn}^{3+}$ redox potential (~ 4.1 V) during charging. At this state, vacancies are likely to be more populated around Fe due to the attractive interaction of $\text{Fe}^{3+}-\text{V}_{\text{Li}}$ (effectively h^+-e^-). [15,31,32] Because Fe is dilute in this system, the generation of $\text{Fe}^{3+}-\text{V}_{\text{Li}}$ will result in $\text{Mn}^{2+}-\text{V}_{\text{Li}}$ (effectively e^-e^-) in neighbors. With further delithiation after full oxidation of Fe^{2+} to Fe^{3+} , Mn^{2+} in the $\text{Mn}^{2+}-\text{V}_{\text{Li}}$ neighbor will most likely be oxidized to Mn^{3+} because there is energetic gain in the transition from $\text{Mn}^{2+}-\text{V}_{\text{Li}}$ (e^-e^-) repulsion to $\text{Mn}^{3+}-\text{V}_{\text{Li}}$ (h^+-e^-) attraction. In contrast, the oxidation of Mn^{2+} , when solely surrounded by $\text{Mn}^{2+}-\text{Li}^+$ pairs, will not have energetic gain in the transition from $\text{Mn}^{2+}-\text{Li}^+$ (effectively e^-h^+) attraction to $\text{Mn}^{3+}-\text{V}_{\text{Li}}$ (h^+-e^-) attraction. Therefore, the $\text{Mn}^{2+}/\text{Mn}^{3+}$ transition will be initiated mostly from Fe-containing regions, where subsequently V_{Li} is further populated due to the attraction between M^{3+} and V_{Li} . This region will serve as nuclei of the delithiated phase in the charge process [Figure 3.1.1 (top)]. Because Fe is extensively spread in the framework, multiple nucleation sites of the delithiated phase can form within a single particle.

A similar effect can be expected during lithiation by substituting Mg into Mn sites. In a highly charged state with full oxidation of Fe^{3+} and Mn^{3+} , remaining Li^+ in the structure will be mostly populated around Mg^{2+} due to the effective repulsion between Li^+ and Fe^{3+} or Mn^{3+} . Because Mg is dilute in the Mn-rich structure, the presence of Li^+ - Mg^{2+} pairs will also introduce unfavorable Mn^{3+} - Li^+ (h^+ - h^+) pairs in the vicinity. With discharge, these unfavorable Mn^{3+} - Li^+ pairs can readily promote the $\text{Mn}^{3+}/\text{Mn}^{2+}$ transition near Mg^{2+} becoming Mn^{2+} - Li^+ (e^- - h^+) pairs [Figure 3.1.1 (bottom)]. This region with Mg^{2+} will initiate nucleation of the lithiated phase in the discharge process.

Motivated by this nucleation enhancer concept in Mn based olivine both at the charge and discharge processes, we have prepared Fe and Mg co-doped $\text{LiFe}_{0.05}\text{Mg}_{0.05}\text{Mn}_{0.9}\text{PO}_4$ and compared its property with the pristine LiMnPO_4 . [15] Figure 3.1.2 shows XRD patterns of the LiMnPO_4 and $\text{LiFe}_{0.05}\text{Mg}_{0.05}\text{Mn}_{0.9}\text{PO}_4$. All materials show standard diffraction patterns of the olivine *Pmnb* space group without any contamination or second phases. The Rietveld refinement tabulated in Table 3.1.1 reveals that the three lattice parameters of pure LiMnPO_4 are $a = 6.115 \text{ \AA}$, $b = 10.463 \text{ \AA}$, and $c = 4.755 \text{ \AA}$, which agree well with previous reports.[29] Those of $\text{LiFe}_{0.05}\text{Mg}_{0.05}\text{Mn}_{0.9}\text{PO}_4$ are $a = 6.087 \text{ \AA}$, $b = 10.420 \text{ \AA}$, and $c = 4.736 \text{ \AA}$. A slight difference in the lattice parameters between LiMnPO_4 and $\text{LiFe}_{0.05}\text{Mg}_{0.05}\text{Mn}_{0.9}\text{PO}_4$ was observed. This

is believed to be due to the differences of the ionic radii of Mn^{2+} , Fe^{2+} , and Mg^{2+} ($\text{Mn}^{2+} > \text{Fe}^{2+} > \text{Mg}^{2+}$) and indicates that Fe and Mg are well incorporated in the olivine crystal.[25] Mg^{2+} is found to be substituted mostly to the transition metal site (M2 site), not to the Li site (M1 site) from the Rietveld refinement, as shown in Table 3.1.2. The particle sizes and morphologies of the two samples are similar as shown in Figure 3.1.3, implying that the possible difference in electrochemical performance does not originate from external factors such as particle size. Also the carbon content analysis showed negligible difference between samples.

The electrochemical performances of the two samples in Li cells are compared in Figure 3.1.4. First, the rate capability of each sample is compared by charging the cells to 4.8V constant current and constant voltage (CCCV) mode, C/20 and 2 h holding and discharging at various rates. The cells were discharged at rates from C/5 to 3C as shown in Figure 3.1.4(a). It is clear that $\text{LiFe}_{0.05}\text{Mg}_{0.05}\text{Mn}_{0.9}\text{PO}_4$ can deliver significantly higher capacities than LiMnPO_4 at all current rates. At C/5, the specific capacity of $\text{LiFe}_{0.05}\text{Mg}_{0.05}\text{Mn}_{0.9}\text{PO}_4$ is approximately 140 mAh g^{-1} , whereas LiMnPO_4 can only deliver *ca.* 100 mAh g^{-1} . The *ca.* 4.1 V plateau is more clearly observed for $\text{LiFe}_{0.05}\text{Mg}_{0.05}\text{Mn}_{0.9}\text{PO}_4$, indicating enhanced kinetic behavior at this current rate. Furthermore, the discharge capacities of $\text{LiFe}_{0.05}\text{Mg}_{0.05}\text{Mn}_{0.9}\text{PO}_4$

at elevated current densities are significantly higher than those of LiMnPO_4 . While the polarization becomes appreciably bigger, therefore rapidly reducing the capacity of the pristine LiMnPO_4 at higher current rates, the polarization is comparably smaller for co-doped materials even at 3C. As a result, the discharge capacity of $\text{LiFe}_{0.05}\text{Mg}_{0.05}\text{Mn}_{0.9}\text{PO}_4$ at 3C is more than 2 times higher than that of LiMnPO_4 . It is notable that 10% substitution can dramatically enhance the power capability of LiMnPO_4 . A Ragone plot for comparison of performance (Figure 3.1.4(b)) shows that $\text{LiFe}_{0.05}\text{Mg}_{0.05}\text{Mn}_{0.9}\text{PO}_4$ retains higher energy density than LiMnPO_4 at all discharge rates. This clearly demonstrates that co-doping of Fe–Mg improves the kinetics of Mn based olivine cathode materials.

The cycle property of $\text{LiFe}_{0.05}\text{Mg}_{0.05}\text{Mn}_{0.9}\text{PO}_4$ is also investigated to check the stability of the electrode. Figures 3.1.4(c) and 3.1.4(d) show specific capacities and the charge-discharge profile at C/3 for 50 cycles. The results show that high capacity is stably retained at extended cycles. The discharge capacity in the first cycle of *ca.* 130 mAh g^{-1} only slightly decreases with further cycling. We suspect that the slight capacity fade during cycle is in part due to the instability of the electrolyte when exposed to high potential (4.8V) for a prolonged time.

To verify the mechanism of the enhanced rate performance of the electrode,

we attempted to perform structural analysis on partially delithiated samples using XRD and transmission electron microscopy. The two samples of $\text{Li}_{1-x}\text{Fe}_{0.05}\text{Mg}_{0.05}\text{Mn}_{0.9}\text{PO}_4$ were prepared at states of (i) and (ii) as denoted in Figure 3.1.5(a). At a state (i), the sample is electrochemically charged up to 4.0V, where Fe^{2+} ions are expected to be fully oxidized. About 30 mAh g^{-1} of Li is extracted from the $\text{LiFe}_{0.05}\text{Mg}_{0.05}\text{Mn}_{0.9}\text{PO}_4$ as shown in the profile. Because the charging voltage is lower than the equilibrium redox potential of $\text{Mn}^{2+}/\text{Mn}^{3+}$ (4.1V), the capacity is mainly attributed to the $\text{Fe}^{2+}/\text{Fe}^{3+}$ transition. However, in spite of the delithiation reaction observed at this state, the XRD study could not find any significant change in the pattern (data not shown here). It is possibly due to the small amount of Fe contents and the small size of the second phase nuclei. Instead, particles were further investigated by high resolution transmission electron microscopy (HRTEM). Figure 3.1.5(b) shows an image of partially delithiated $\text{Li}_{1-x}\text{Fe}_{0.05}\text{Mg}_{0.05}\text{Mn}_{0.9}\text{PO}_4$ at (i), showing clear lattice images. Fast Fourier transform (FFT) of the HRTEM image in Figure 3.1.5(c) reveals that a new phase has indeed arisen in a single particle of $\text{Li}_{1-x}\text{Fe}_{0.05}\text{Mg}_{0.05}\text{Mn}_{0.9}\text{PO}_4$ charged to 4.0V. The formation of a second phase at charging below 4.0V clearly indicates the existence of multiple nucleation sites provided by Fe redox couple for the Li^+ deintercalated phase. This observation is in good agreement with our previous paper.[15]

Additionally, the influence of Mg^{2+} was investigated by analyzing the sample at a (ii) state. At a state (ii), the sample is fully charged up to 4.8V, as denoted in Figure 3.1.5(a). Due to the $\text{Fe}^{2+}/\text{Fe}^{3+}$ transition at *ca.* 3.4V and the $\text{Mn}^{2+}/\text{Mn}^{3+}$ transition at *ca.* 4.1V, all Fe and Mn ions in the sample are expected to be in 3+ in the state (ii). While the similar XRD study on this sample did not find any significant change in the pattern, HRTEM reveals the existence of two phases. Figure 3.1.5(d) shows the continuous lattice images of a sample at (ii). The corresponding FFT of the HRTEM image in Figure 3.1.5(e) indicates that two phases coexist in a single particle. The lithiated phase is still present even in the fully charged sample at a scale visible to electron beam. We suspect that the presence of Mg in the matrix prevents full delithiation and provides initial sites for the growth of the lithiated phase. It should be noted that investigation of multiple particles yielded the same results.

We further pursued the evidence of facile and multiple nucleations in the co-doped sample by potentiostatic intermittent titration technique experiments. In Figure 3.1.6(a) and 3.1.6(b), the PITT voltage steps and corresponding current relaxation curves are compared for $\text{LiFe}_{0.05}\text{Mg}_{0.05}\text{Mn}_{0.9}\text{PO}_4$ and LiMnPO_4 electrodes. One noticeable observation is that the apparent plateau region significantly shrinks in the $\text{LiFe}_{0.05}\text{Mg}_{0.05}\text{Mn}_{0.9}\text{PO}_4$ compared with LiMnPO_4 .

In this plateau region, the current [$I(t)$] decreases rapidly to a very low value, and then reaches the limit value slowly. This behavior is typically observed in a two-phase reaction.[33,34] However, when we carefully examined the behavior of $I(t)$ at regions before and after the apparent plateaus by zooming in as shown in Figure 3.1.6(c) and 3.1.6(d), respectively, a somewhat unexpected phenomenon was observed. The current decay at each step showed a Cottrellian ($1/t^{1/2}$) dependence, which indicates that the process is a solid-solution insertion/extraction reaction.[33,34] This appears to be in contrast to the expected role of Fe and Mg as a nucleation enhancer at a first glance. However, considering that Fe and Mg are extensively distributed in the matrix, and therefore numerous nuclei with very small size (small enough not to be visible by XRD) will be formed and distributed extensively in a matrix, the distinction between solid solution and two phase can be blurred at this scale. The fact that the Cottrellian region significantly increased in the electrochemical profile below and above the equilibrium potential of $\text{Mn}^{2+}/\text{Mn}^{3+}$ (*ca.* 4.1 V) reflects that the codoping alters the nucleation behavior of the second phase in LiMnPO_4 framework by inducing “numerous small nucleation” in the matrix or “solid solution.”

3.1.4 Conclusion

The effects of nucleation enhancer on properties of Mn based olivine

cathode materials were investigated by co-doping Fe and Mg. The unfavorable $\text{Mn}^{2+}\text{-V}_{\text{Li}}$ (or $\text{Mn}^{3+}\text{-Li}^+$) pair neighbors created by local $\text{Fe}^{3+}\text{-V}_{\text{Li}}\text{-Mn}^{2+}$ (or $\text{Mg}^{2+}\text{-Li}^+\text{-Mn}^{3+}$) regions during Li^+ (de)intercalation promote the $\text{Mn}^{2+}/\text{Mn}^{3+}$ redox transition, where Fe^{3+} (in Li^+ deintercalation) and Mg^{2+} (in Li^+ intercalation) act as nucleation enhancers. Easier and more frequent nucleation aided by Fe and Mg co-doping enhanced the power capability of Mn based olivine cathode, as evidenced by superior electrochemical performance, a result that is not easily achieved using pristine LiMnPO_4 without nucleation enhancers. These results present a direction for future systematic investigation of nucleation enhancers in Mn based olivine cathode materials. We believe that our strategy can be further extended to electrode materials based on a two-phase reaction that have been excluded because of their sluggish kinetics.

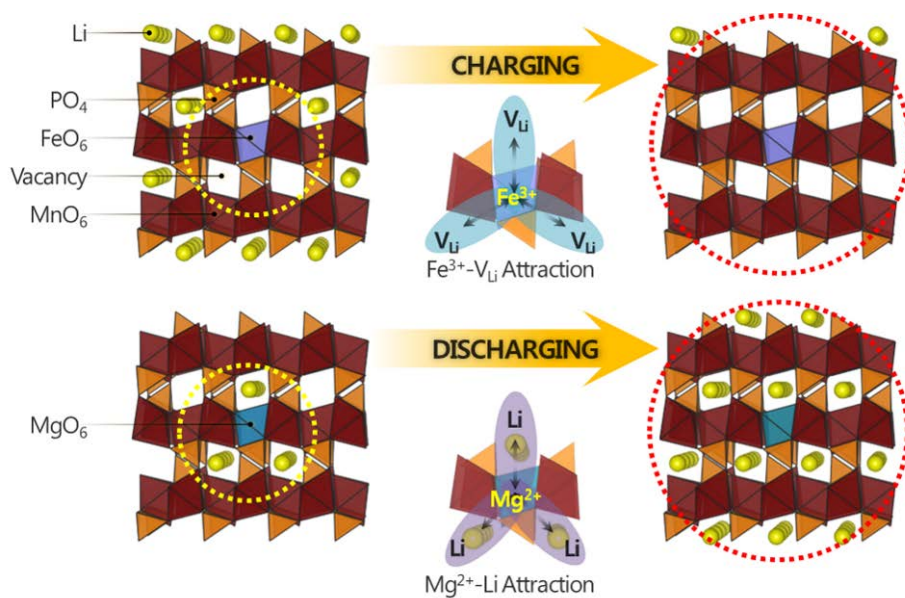


Figure 3.1.1 (Color online) Schematic illustration of the nucleation enhancing process in a multicomponent Mn based olivine cathode during charging and discharging (Yellow: Li, red: MnO₆, purple: FeO₆, blue: MgO₆, orange: PO₄, white: vacancy). Arrows are used to indicate the favorable interaction.

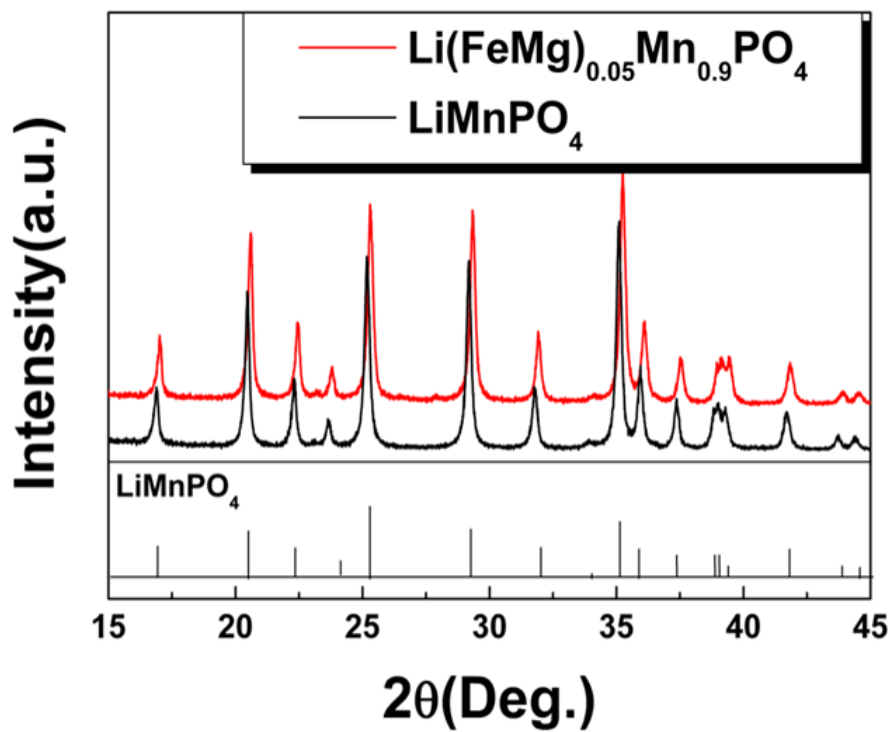


Figure 3.1.2 (Color online) XRD patterns and lattice parameter of LiMnPO_4 and $\text{LiFe}_{0.05}\text{Mg}_{0.05}\text{Mn}_{0.9}\text{PO}_4$ between $2\theta = 15^\circ$ and $2\theta = 45^\circ$

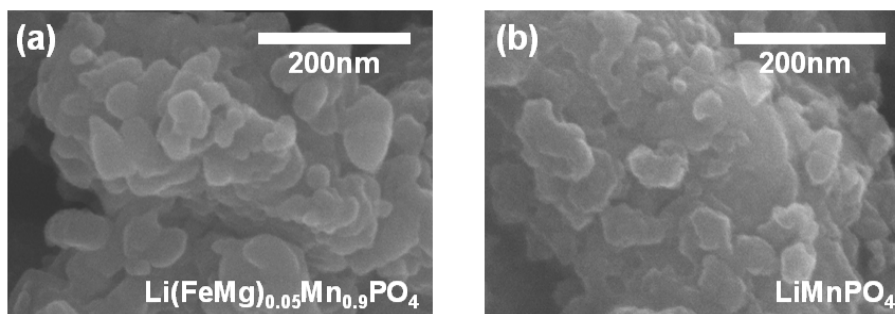


Figure 3.1.3 Scanning electron microscopy images of (a) LiMnPO_4 and (b) $\text{LiFe}_{0.05}\text{Mg}_{0.05}\text{Mn}_{0.9}\text{PO}_4$

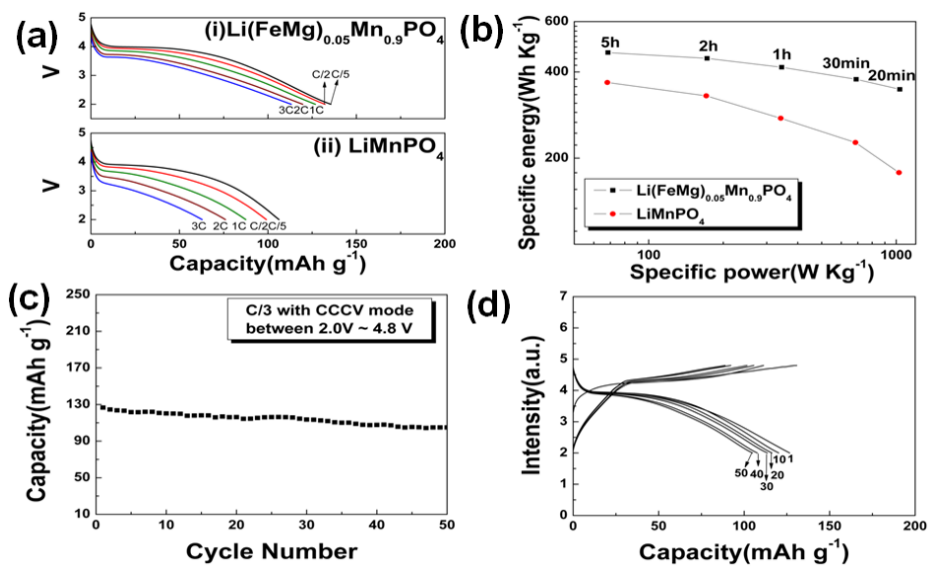


Figure 3.1.4 (Color online) (a) Rate capability of $\text{LiFe}_{0.05}\text{Mg}_{0.05}\text{Mn}_{0.9}\text{PO}_4$ and LiMnPO_4 from C/5 to 3C; 1C corresponds to about 171 mA g^{-1} , (b) The Ragone plot for LiMnPO_4 and $\text{LiFe}_{0.05}\text{Mg}_{0.05}\text{Mn}_{0.9}\text{PO}_4$, (c) Galvanostatic cyclability data of the 50 cycles for $\text{LiFe}_{0.05}\text{Mg}_{0.05}\text{Mn}_{0.9}\text{PO}_4$ between 4.8 and 2 V at a C/3 rate, (d) Corresponding charge/discharge curves of the 50 cycles for $\text{LiFe}_{0.05}\text{Mg}_{0.05}\text{Mn}_{0.9}\text{PO}_4$

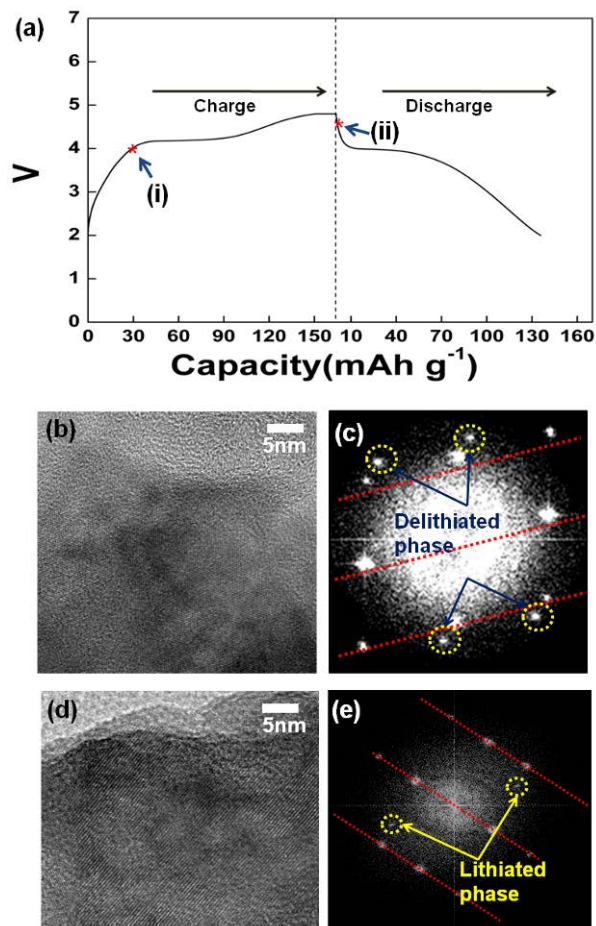


Figure 3.1.5 (Color online) (a) Charge/discharge profile of $\text{LiFe}_{0.05}\text{Mg}_{0.05}\text{Mn}_{0.9}\text{PO}_4$ [(i): the charge state of the examined $\text{Li}_{1-x}\text{Fe}_{0.05}\text{Mg}_{0.05}\text{Mn}_{0.9}\text{PO}_4$, (ii): the discharge state of the examined $\text{Li}_x\text{Fe}_{0.05}\text{Mg}_{0.05}\text{Mn}_{0.9}\text{PO}_4$], (b) Typical HRTEM image of a particle charged up to 0.4V, (c) Fourier transforms of the Figure 4(b) image [yellow circle: delithiated phase], (d) Typical HRTEM image of a particle charging up to 4.8V, and (e) Fourier transforms of the Figure 4(d) image [yellow circle: lithiated phase]

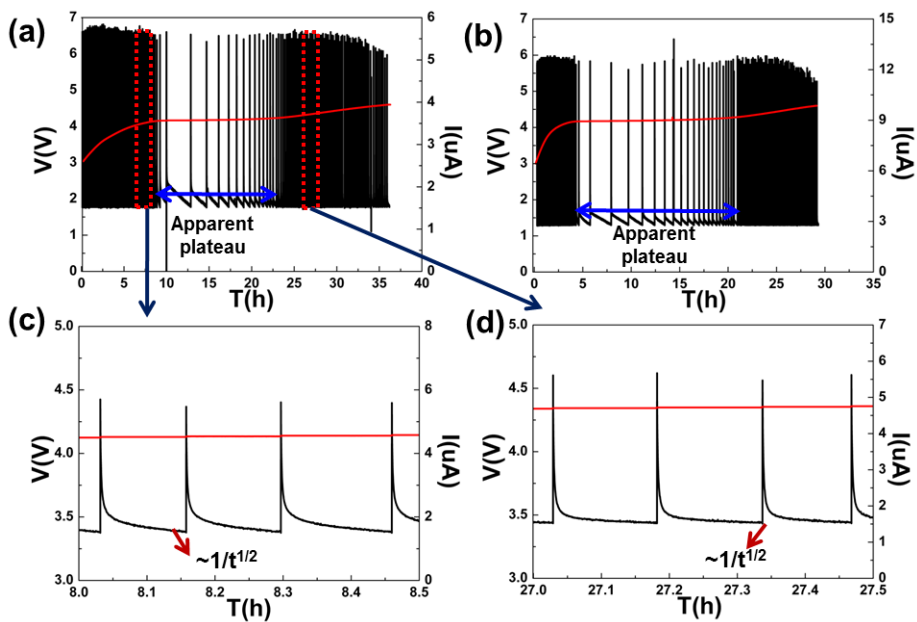


Figure 3.1.6 (Color online) PITT measurements upon charging of (a) $\text{LiFe}_{0.05}\text{Mg}_{0.05}\text{Mn}_{0.9}\text{PO}_4$ and (b) LiMnPO_4 from 3 to 4.6 V, and the zoomed PITT profiles of $\text{LiFe}_{0.05}\text{Mg}_{0.05}\text{Mn}_{0.9}\text{PO}_4$ (c) between 7 and 10 h and (d) between 21 and 26 h

	a (Å)	b (Å)	c (Å)
LiMnPO₄	6.115	10.463	4.755
LiFe_{0.05}Mg_{0.05}Mn_{0.9}PO₄	6.087	10.420	4.736

Table 3.1.1 Lattice parameters of LiMnPO₄ and LiFe_{0.05}Mg_{0.05}Mn_{0.9}PO₄ obtained by the Rietveld refinement

Name	Type	Occupancy (Theoretical)	Occupancy (Experimental)
Li1	Li⁺¹	1	0.9988
Li2	Li⁺¹	0	0.0012
Mg1	Mg⁺²	0	0.0012
Mg2	Mg⁺²	0.05	0.0488
Fe1	Fe⁺²	0.05	0.05
Mn1	Mn⁺²	0.9	0.9
P	P⁺⁵	1	1
O1	O⁻²	1	1
O2	O⁻²	1	1
O3	O⁻²	1	1
O4	O⁻²	1	1

Table 3.1.2 Site occupancies of $\text{LiFe}_{0.05}\text{Mg}_{0.05}\text{Mn}_{0.9}\text{PO}_4$ obtained by the Rietveld refinement

3.1.5 References

- [1] P. S. Herle, B. Ellis, N. Coombs, and L. F. Nazar, *Nature Mater.*, **3**, 147 (2004).
- [2] M. Yonemura, A. Yamada, Y. Takei, N. Sonoyama, and R. Kanno, *J. Electrochem. Soc.*, **151**, A1352 (2004).
- [3] S. Y. Chung, J. T. Bloking, and Y. M. Chiang, *Nature Mater.*, **1**, 123 (2002).
- [4] C. Delmas, M. Maccario, L. Croguennec, F. Le Cras, and F. Weill, *Nature Mater.*, **7**, 665 (2008).
- [5] B. Kang and G. Ceder, *Nature*, **458**, 190 (2009).
- [6] A. K. Padhi, K. S. Nanjundaswamy, C. Masquelier, S. Okada, and J. B. Goodenough, *J. Electrochem. Soc.*, **144**, 1609 (1997).
- [7] A. K. Padhi, K. S. Nanjundaswamy, and J. B. Goodenough, *J. Electrochem. Soc.*, **144**, 1188 (1997).
- [8] S. Nishimura, G. Kobayashi, K. Ohoyama, R. Kanno, M. Yashima, and A. Yamada, *Nat. Mater.*, **7**, 707 (2008).
- [9] C. Delacourt, P. Poizot, J.-M. Tarascon, and C. Masquelier, *Nat. Mater.*, **4**, 254 (2005).
- [10] A. Yamada, M. Hosoya, S.-C. Chung, Y. Kudo, K. Hinokuma, K.-Y. Liu, and Y. Nishi, *J. Power Sources*, **232**, 119-121 (2003).

- [11] F. Zhou, M. Cococcioni, K. Kang, and G. Ceder, *Electrochem. Commun.*, **6**, 1144 (2004).
- [12] C. Delacourt, L. Laffont, R. Bouchet, C. Wurm, J. B. Leriche, M. Morcrette, J. M. Tarascon, and C. Masquelier, *J. Electrochem. Soc.*, **152**, A913 (2005).
- [13] G. H. Li, H. Azuma, and M. Tohda, *Electrochem. Solid-State Lett.*, **5**, A135 (2002).
- [14] D. W. Choi, D. H. Wang, I. T. Bae, J. Xiao, Z. M. Nie, W. Wang, V. V. Viswanathan, Y. J. Lee, J. G. Zhang, G. L. Graff, *et al.*, *Nano Lett.*, **10**, 2799 (2010).
- [15] J. Kim, D. H. Seo, S. W. Kim, Y. U. Park, and K. Kang, *Chem. Commun.*, **46**, 1305 (2010).
- [16] T. Shiratsuchi, S. Okada, T. Doi, and J. Yamaki, *Electrochim. Acta*, **54**, 3145 (2009).
- [17] H. S. Fang, L. P. Li, Y. Yang, G. F. Yan, and G. S. Li, *Chem. Commun.*, 1118 (2008) (**DOI**: 10.1039/B716916G).
- [18] S. K. Martha, B. Markovsky, J. Grinblat, Y. Gofer, O. Haik, E. Zinigrad, D. Aurbach, T. Drezen, D. Wang, G. Deghenghi, *et al.*, *J. Electrochem. Soc.*, **156**, A541 (2009).
- [19] D. Y. Wang, H. Buqa, M. Crouzet, G. Deghenghi, T. Drezen, I. Exnar, N.

- H. Kwon, J. H. Miners, L. Poletto, and M. Graetzel, *J. Power Sources*, **189**, 624 (2009).
- [20]. Z. Bakenov and I. Taniguchi, *J. Power Sources*, **195**, 7445 (2010).
- [21] B. Kang and G. Ceder, *J. Electrochem. Soc.*, **157**, A808 (2010).
- [22]. K. Saravanan, J. J. Vittal, M. V. Reddy, B. V. R. Chowdari, and P. Balaya, *J. Solid State Electrochem.*, **14**, 1755 (2010).
- [23] D. Y. Wang, C. Y. Ouyang, T. Drezen, I. Exnar, A. Kay, N. H. Kwon, P. Gouerec, J. H. Miners, M. K. Wang, and M. Gratzel, *J. Electrochem. Soc.*, **157**, A225 (2010).
- [24] J. Xiao, W. Xu, D. W. Choi, and J. G. Zhang, *J. Electrochem. Soc.*, **157**, A142 (2010).
- [25] J. J. Chen, M. J. Vacchio, S. J. Wang, N. Chernova, P. Y. Zavalij, and M. S. Whittingham, *Solid State Ionics*, **178**, 1676 (2008).
- [26] H. Gwon, D. H. Seo, S. W. Kim, J. Kim, and K. Kang, *Adv. Funct. Mater.*, **19**, 3285 (2009).
- [27] D. H. Seo, H. Gwon, S. W. Kim, J. Kim, and K. Kang, *Chem. Mater.*, **22**, 518 (2010).
- [28] Y.-U. Park, J. Kim, H. Gwon, D. H. Seo, S. W. Kim, and K. Kang, *Chem. Mater.*, **22**, 2573 (2010).
- [29] S.-W. Kim, J. Kim, H. Gwon, and K. Kang, *J. Electrochem. Soc.*, **156**,

A635 (2009).

[30] C. Delacourt, P. Poizot, M. Morcrette, J. M. Tarascon, and C. Masquelier, *Chem. Mater.*, **16**, 93 (2004).

[31] F. Zhou, T. Maxisch, and G. Ceder, *Phys. Rev. Lett.*, **97**, 155704 (2006).

[32] R. Malik, F. Zhou, and G. Ceder, *Phys. Rev. B*, **79**, 214201 (2009).

[33] N. Meethong, Y. H. Kao, W. C. Carter, and Y. M. Chiang, *Chem. Mater.*, **22**, 1088 (2010).

[34] M. Jiang, B. Key, Y. S. Meng, and C. P. Grey, *Chem. Mater.*, **21**, 2733 (2009).

3.2 The Effect of Particle Size on Phase Stability of the Delithiated Li_xMnPO_4

3.1.1 Research Background

Recently, olivine-type LiMPO_4 ($M = \text{Fe, Mn, Co, Ni}$) compounds have been highlighted as a promising class of cathode materials in Li rechargeable batteries.[1-9] The strong covalent P-O bonds in the tetrahedral $(\text{PO}_4)^{3-}$ anion are believed to inhibit oxygen loss at a highly charged state and to contribute to the high structural stability and dependable safety of LiMPO_4 . This makes LiMPO_4 suitable for large applications such as electric vehicles (EV) and hybrid electric vehicles (HEV), where safety is one of the most important issues for commercialization. Among olivine-type LiMPO_4 , LiFePO_4 has been the most widely studied due to lower cost, safety, and significantly improved power.[3, 10-12] However, its intrinsic problem of low energy density, resulting from the low redox potential of $\text{Fe}^{2+}/\text{Fe}^{3+}$ (*ca.* 3.4V), is a major drawback to its use.[1-4] In this respect, LiMnPO_4 , which offers an operating potential of *ca.* 4.1 V ($\text{Mn}^{2+}/\text{Mn}^{3+}$ redox), is considered to be attractive and promising.[6, 8, 13-16] Accordingly, this material has been the subject of intensive research efforts.

Recently, the thermal behavior of Li_xMnPO_4 ($0 \leq x \leq 1$) and reported a phase distribution diagram of Li_xMnPO_4 ($0 \leq x \leq 1$) in the temperature range

between 25°C and 400°C. It was found that delithiated Li_xMnPO_4 ($0 \leq x \leq 1$), which consists of $_x\text{LiMnPO}_4$ and $(1-x)\text{MnPO}_4$, yields a decomposition product, $\text{Mn}_2\text{P}_2\text{O}_7$, while the fully lithiated LiMnPO_4 remains stable up to fairly high temperatures. In the present work, we intend to further study the effect of particle size on the thermal behavior of delithiated phase Li_xMnPO_4 ($x < 1$) and demonstrate that particle size apparently affects the phase stability of delithiated Li_xMnPO_4 ($x \approx 0$). Because nanosizing of LiMnPO_4 is indispensable to compensate for its intrinsic poor kinetic behavior,[9, 20] study of the thermal characteristic of the nanosize LiMnPO_4 becomes more important. This study reports that the Li_xMnPO_4 of small particle size (*ca.* 50nm) undergoes phase transformation into $\text{Mn}_3(\text{PO}_4)_2$ with an amorphous P-rich phase in contrast to that of large particle size (*ca.* 200 nm \sim *ca.* 1 μm).

3.2.2 Experimental Section

Three LiMnPO_4 samples with different particle sizes were synthesized using the conventional solid state synthesis by varying the calcination temperature (600°C, 700°C, and 800°C). Li_2CO_3 (Junsei Chemical, 98%), $\text{Mn}(\text{CH}_3\text{COO})_2 \cdot 4\text{H}_2\text{O}$ (Junsei Chemical, 98%), and $\text{NH}_4\text{H}_2\text{PO}_4$ (Fluka, 99%) with molar ratio of 0.5 : 1 : 1 were used as precursors. They were dispersed in acetone, and then thoroughly mixed by ball-milling. After evaporating the acetone, the precursor mixture was then fired at 350°C under Ar condition for

3hours. The mixture was then re-ground and manually pelletized using a disk-shaped mold. Each pellet was reheated at 600°C, 700°C, and 800°C under Ar condition for 10 hours.

To prepare Li_xMnPO_4 , each LiMnPO_4 was chemically delithiated by NO_2BF_4 (Aldrich, 95%) according to the following reaction:



NO_2BF_4 is a strong oxidizing agent with a high redox potential of $\text{NO}_2^+/\text{NO}_2$ at 5.1V vs. Li^+/Li . The composition of Li_xMnPO_4 was controlled by adjusting the reaction time between LiMnPO_4 and NO_2BF_4 which were at a molar ratio of 1:1 in acetonitrile (Aldrich, 98%) at 70°C in an Ar-filled glove box. As the particle size of LiMnPO_4 increases, delithiation process of LiMnPO_4 becomes harder. Therefore, LiMnPO_4 that has larger particle size needs more delithiation reaction time. The Li amount in Li_xMnPO_4 was finally analyzed by inductively coupled plasma atomic emission spectroscopy (ICPAES).

The crystal structure was determined by XRD (Rigaku D/Max 2500) with Cu K α radiation ($\lambda=1.54178\text{\AA}$) operating at 30 kV and 400 mA. For the temperature-dependent phase stability study, the sample was heated from 25°C to 450°C in vacuum during the XRD investigation. The heating rate was 5°C/min, the waiting time between heating and measurement was 3 min, and the scan speed was 1°/min. Structural refinements were performed by the

Rietveldmethod using a general structure analysis system (GSAS). The nano/microstructures were investigated by field-emission scanning electron microscopy (FESEM, Philips XL30SFEG).

3.2.3 Computational Details

The hypothetical $\text{Mn}_3(\text{PO}_4)_2$ structure used for the XRD study was calculated from first principles, starting from the $\text{Fe}_3(\text{PO}_4)_2$ structure.[21] First principles calculations were performed with the spin-polarized generalized gradient approximation (GGA) applying the Perdew-Burke-Ernzerhof exchange-correlation parametrization [22] to density functional theory (DFT). A plane-wave basis set and the projector-augmented wave (PAW) method was used as implemented in the Vienna *ab initio* simulation package (VASP).[23] PAW potentials have been widely used for battery materials and have shown good predictive capability.[9, 24-26] A plane-wave bases with a kinetic energy cutoff of 500eV were used, and appropriate *k*-point meshes were chosen to ensure that the total energy converged within 5meV per formula unit. The structure was fully relaxed with ferromagnetic ordering.

3.2.4 Results and Discussion

The thermal behavior of the delithiated Li_xMnPO_4 was investigated for samples having various particle sizes. Pristine LiMnPO_4 samples synthesized at 600°C, 700°C, and 800°C are shown in the SEM images of Figure 3.2.1. The

particle size of LiMnPO_4 increased with higher synthesis temperature. The size of particles obtained at 600°C was *ca.* 50nm; at 700°C , *ca.* 200 nm; and at 800°C , *ca.* $1\mu\text{m}$. The XRD patterns of three pristine LiMnPO_4 did not show significant difference among them (shown later).

First, we examined the large particle size LiMnPO_4 synthesized at 800°C (LiMnPO_4 -800, hereafter). Figure 3.2.2 shows the evolution of XRD patterns of Li_xMnPO_4 -800 ($0 \leq x \leq 1$) with the delithiation process. The XRD pattern of pristine LiMnPO_4 -800 confirms the olivine phase with *Pmb* space group.[8, 17] No noticeable contamination or second phase was found. The refined lattice parameters of the pristine LiMnPO_4 -800 are $a = 6.117\text{\AA}$, $b = 10.469\text{\AA}$, and $c = 4.757\text{\AA}$. Partially delithiated Li_xMnPO_4 is denoted as PD1, PD2, and PD3. (The amount of Li in the structure: PD1 > PD2 > PD3) As the delithiation process continued, typical two-phase behavior was observed as reported previously.[17, 18] Peaks of LiMnPO_4 gradually disappeared, while those of MnPO_4 started to appear and grow. The ICP-AES analyses of three samples (PD1, PD2, and PD3) reveals that Li amount of PD1, PD2 and PD3 are 0.86, 0.63, and 0.11, respectively.

Figure 3.2.3(a) illustrates the *in situ* XRD patterns of PD1 at various temperatures, from 200°C to 400°C in the 2θ range of 24° - 40° . XRD Peaks of a new phase start to appear and grow at the temperature between 200°C and

250°C by the decomposition of Li_xMnPO_4 . We can find that the new phases were $\text{Mn}_2\text{P}_2\text{O}_7$ by matching XRD peaks. The embossed XRD peak at *ca.* 29° which corresponds to the main XRD peak of $\text{Mn}_2\text{P}_2\text{O}_7$ supports this identification. The growth of XRD peaks related to $\text{Mn}_2\text{P}_2\text{O}_7$ becomes much clearer for PD2 and PD3, as shown in Figure 3.2.3(b) and 3.2.3(c). The XRD peaks at *ca.* 29° and *ca.* 34° in the PD2 and PD3 grew markedly between 200°C and 250°C indicating phase transition from MnPO_4 to $\text{Mn}_2\text{P}_2\text{O}_7$ at temperature range. These results correspond well with our previous report,[17] which showed that the delithiated phase underwent partial phase transformation into $\text{Mn}_2\text{P}_2\text{O}_7$, regardless of the Li content in Li_xMnPO_4 .

We also conducted similar experiments on LiMnPO_4 synthesized at 700°C (LiMnPO_4 -700, hereafter). Figure 3.2.4 shows the XRD patterns of Li_xMnPO_4 -700 with differing delithiated states ($0 \leq x \leq 1$). Pristine LiMnPO_4 -700 also showed no noticeable contamination or second phase and had almost identical lattice parameters ($a = 6.116\text{\AA}$, $b = 10.469\text{\AA}$, and $c = 4.756\text{\AA}$). The two phase reaction during delithiation was also observed. At fully delithiated MnPO_4 -700, no Li was detected from the analysis of ICP-AES.

Figure 3.2.5(a) shows the series of XRD patterns of partially delithiated Li_xMnPO_4 -700 at temperatures from 200°C to 400°C in the 2θ range of 24°-40°. Similar to the case of Li_xMnPO_4 -800, the peaks of *ca.* 29° and *ca.* 34°, which

are related to $\text{Mn}_2\text{P}_2\text{O}_7$, grew progressively at the temperature between 200°C and 250°C.[17, 18] We also found the same trend in the fully delithiated MnPO_4 -700, as shown Figure 3.2.5(b). Decomposition of MnPO_4 started between 200°C and 250°C with the appearance of the new non-olivine phase $\text{Mn}_2\text{P}_2\text{O}_7$. The thermal decomposition mechanism of both delithiated phases of LiMnPO_4 -700 and LiMnPO_4 -800 is consistent with previous results.[17, 18] It is noted that the particle size of LiMnPO_4 in the previous works[17, 18] was about 200nm thick and 1 μm long, compared to those of LiMnPO_4 -700 (200nm) and LiMnPO_4 -800 (1 μm) in this study.

Finally, the delithiation process of LiMnPO_4 synthesized at 600°C (LiMnPO_4 -600, hereafter) was monitored by XRD (Figure 3.2.6). Pristine LiMnPO_4 -600 also showed the standard diffraction pattern of olivine material ($a = 6.115\text{\AA}$, $b = 10.463\text{\AA}$, $c = 4.755\text{\AA}$) without any contamination or second phase. The two-phase reaction was also confirmed. At fully delithiated MnPO_4 -600, no Li was detected from the analysis of ICP-AES.

Figure 3.2.7(a) shows the *in situ* XRD patterns of fully delithiated MnPO_4 -600 at temperature range from 25°C to 450°C. While the MnPO_4 phase retained the original XRD pattern from 25°C to 250°C, decomposition into a new non-olivine phase started between 200°C and 250°C. The new phase with its main peak located at *ca.* 25° (denoted as * in the figure) exhibits a different

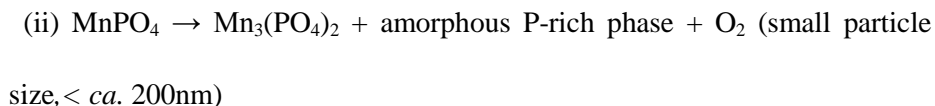
XRD pattern from that of $\text{Mn}_2\text{P}_2\text{O}_7$ (whose main XRD peak is at *ca.* 29°). We found that these new sets of XRD peaks were similar to the XRD pattern of $\text{Fe}_3(\text{PO}_4)_2$. [21] Because Fe ions do not exist in this material, we suggest that the new phase is the isostructural $\text{Mn}_3(\text{PO}_4)_2$, which has not been reported previously in the ICDD (International Centre for Diffraction Data). [27] To verify this assumption, we calculated the XRD pattern of the hypothetical $\text{Mn}_3(\text{PO}_4)_2$ from DFT calculations. The calculated lattice parameters of $\text{Mn}_3(\text{PO}_4)_2$ are $a = 6.23192\text{\AA}$, $b = 4.93574\text{\AA}$, $c = 10.7326\text{\AA}$. The XRD pattern of $\text{Mn}_3(\text{PO}_4)_2$ constructed from first principle calculations is consistent with the new set of XRD peaks resulting from the decomposition of MnPO_4 , as shown in Figure 3.2.7(b). When the temperature increased to 250°C , the peaks of $\text{Mn}_3(\text{PO}_4)_2$ started to appear in the XRD pattern with the decomposition of MnPO_4 -600. However, the decomposition of MnPO_4 to $\text{Mn}_3(\text{PO}_4)_2$ resulted in an imbalance of the Mn: P stoichiometry. Thus, another new non-olivine P-rich phase has to be formed. However, due to the broad characteristics of the peaks, it was hard to clearly define a new P-rich phase. This also indicates that amorphization of MnPO_4 and the new P-rich phase occur to some extent at the same time.

In partially delithiated Li_xMnPO_4 -600, the coexistence of two XRD patterns from fully lithiated LiMnPO_4 and fully delithiated MnPO_4 is observable due

to the two phase reaction in the delithiation of LiMnPO_4 . The decomposition of partially delithiated Li_xMnPO_4 -600 (a mixture of $x\text{LiMnPO}_4$ and $(1-x)\text{MnPO}_4$) upon heating was observed from 250°C , as shown Figure 3.2.7(c). We previously noted that large particle Li_xMnPO_4 ($x\text{LiMnPO}_4 + (1-x)\text{MnPO}_4$) decomposes into mixture $x\text{LiMnPO}_4 + (1-x)/2\text{Mn}_2\text{P}_2\text{O}_7$ regardless of the amounts of Li in Li_xMnPO_4 . [17] In the case of small particle Li_xMnPO_4 (partially delithiated Li_xMnPO_4 -600), it is similar that only the MnPO_4 phase decomposes regardless of the Li amount. However, decomposition products appear to be different. In Figure 3.2.7(d), we can confirm that partially delithiated Li_xMnPO_4 -600 decomposes into $\text{Mn}_3(\text{PO}_4)_2$ instead of $\text{Mn}_2\text{P}_2\text{O}_7$.

From the series of XRD results above, it was found that the delithiated phase of LiMnPO_4 having small particle size (*ca.* 50nm) displayed thermal characteristics different from those having the large particle size material. [17] Stable phases for the delithiated Li_xMnPO_4 upon heating are illustrated with respect to particle size in Figure 3.2.8. The temperature line for the phase transition of Li_xMnPO_4 is located between 200°C and 250°C regardless of the particle size of LiMnPO_4 . However, the phase transition into $\text{Mn}_3(\text{PO}_4)_2$ occurs for delithiated Li_xMnPO_4 having small particle size below 200nm, while that having particle size larger than 200nm yields $\text{Mn}_2\text{P}_2\text{O}_7$ on decomposition. The decomposition reaction of MnPO_4 at high temperature is

proposed to occur by the following reactions:



We believe that the reason for the different phase transformation behavior in MnPO_4 with the particle size is the surface energy term of the Gibbs free energy. The Gibbs free energy of a material with a finite size can be expressed as follows:

$$\text{Gibbs free energy} = \text{Bulk Energy} + \text{Surface Energy} + \text{Surface Tension}$$

Surface energy and surface tension depend on the particle size. Generally, surface tension is only relevant at a very small particle size ($\sim 2\text{nm}$ or less), and thus, it is negligible in this case. However, the surface energies can differ significantly. If each phase in (i) and (ii) contains different magnitude of the surface energy term, the relative difference of surface energies among them will alter the reaction path into either (i) or (ii) according to the particle size. In fact, this kind of phenomenon is not new; many oxides exhibit purely size-driven phase transitions at the nanoscale.[28, 29]

Simple calculation shows that surface energy term increases by *ca.* 50 meV/formula unit as the particle size reduces from $1\mu\text{m}$ to 50 nm assuming the average surface energy of MnPO_4 is comparable to that of LiMnPO_4

(0.892 J/m²).[30] Because particle size of delithiated phase, MnPO₄, did not change from that of LiMnPO₄ as shown in Figure 3.2.9, we suppose that the particle size reduction to 50nm will lead to the surface energy difference in the order of 50meV/formula unit of MnPO₄. In the previous report on the structurally similar LiCoPO₄, Co₂P₂O₇ was found as the decomposition product, whose energy differs by only less than 1 meV/formula unit above the convex hull formed by Co₃(PO₄)₂ and Co(PO₃)₂. [31] This clearly points out that 50meV/formula unit difference is big enough to cause different route of phase transition.

2.2.5 Conclusion

The effect of particle size on phase stability of the delithiated phase Li_xMnPO₄ was investigated using temperature-controlled *in situ* XRD. The delithiated Li_xMnPO₄ having large particle size decomposes into Mn₂P₂O₇ in accordance with previous work. However, when the particle size of LiMnPO₄ decreases from *ca.* 1μm to *ca.* 50nm, the delithiated Li_xMnPO₄ undergoes partial phase transformation into Mn₃(PO₄)₂ below 250°C. We believe that this change in the decomposition reaction is purely size-driven due to the surface energy term of the Gibbs free energy, as reported for other oxides.[28, 29] This work also implies that the safety characteristics of LiMnPO₄-based battery may differ depending on the particle size.

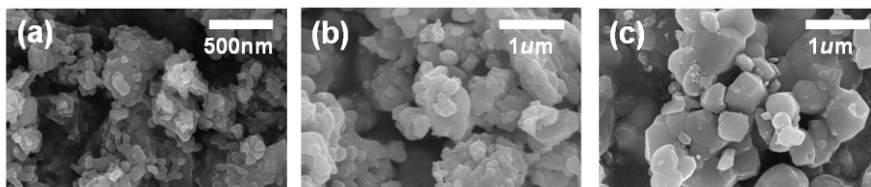


Figure 3.2.1 SEM images of three different pristine LiMnPO_4 synthesized at (a) 600°C , (b) 700°C and (c) 800°C

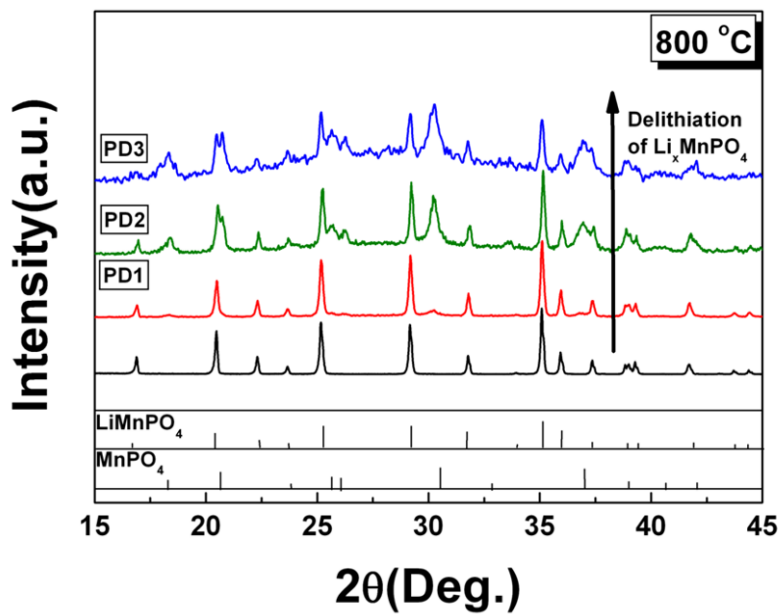


Figure 3.2.2 Evolution of XRD patterns of Li_xMnPO_4 -800 [$0 < x \leq 1$] with a delithiation process

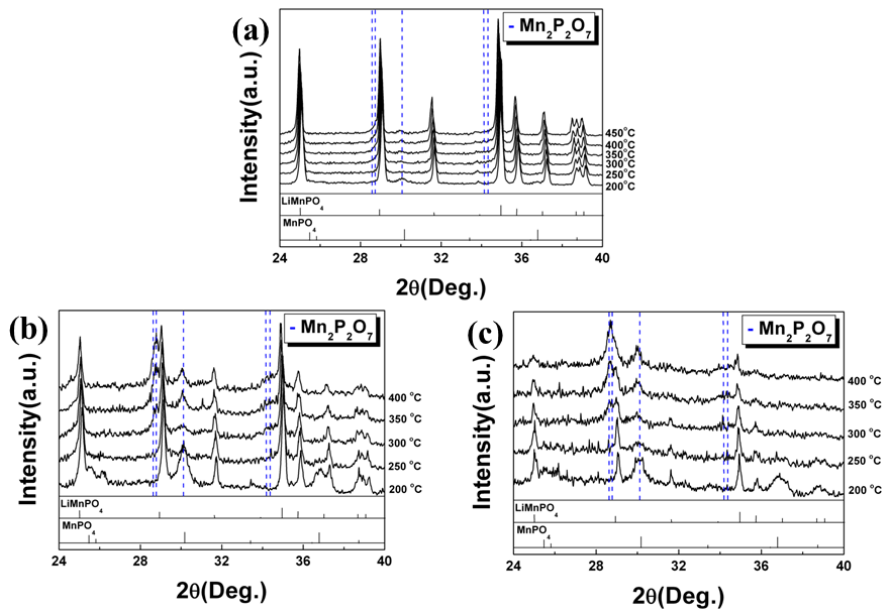


Figure 3.2.3 (a) *in-situ* XRD patterns of partially delithiated Li_xMnPO₄-800 (PD1) at high temperature from 200°C to 400°C around $2\theta = 24^\circ \sim 40^\circ$, (b) *in-situ* XRD patterns of more partially delithiated Li_xMnPO₄-800 (PD2) at high temperature from 200°C to 400°C around $2\theta = 24^\circ \sim 40^\circ$, and (c) *in-situ* XRD patterns of nearly fully delithiated Li_xMnPO₄-800 (PD3) at high temperature from 200°C to 400°C around $2\theta = 24^\circ \sim 40^\circ$. [Li amount in the structure: PD1 > PD2 > PD3]

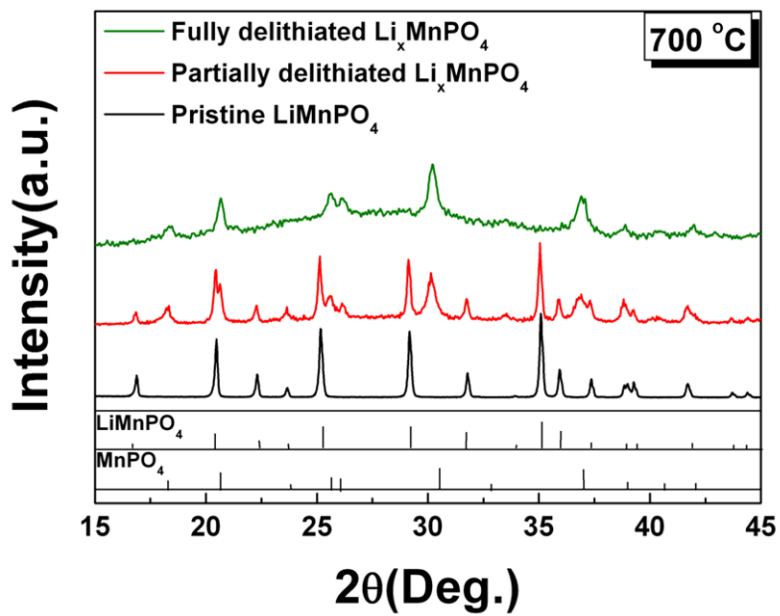


Figure 3.2.4 XRD patterns of Li_xMnPO_4 -700 [$0 \leq x \leq 1$]

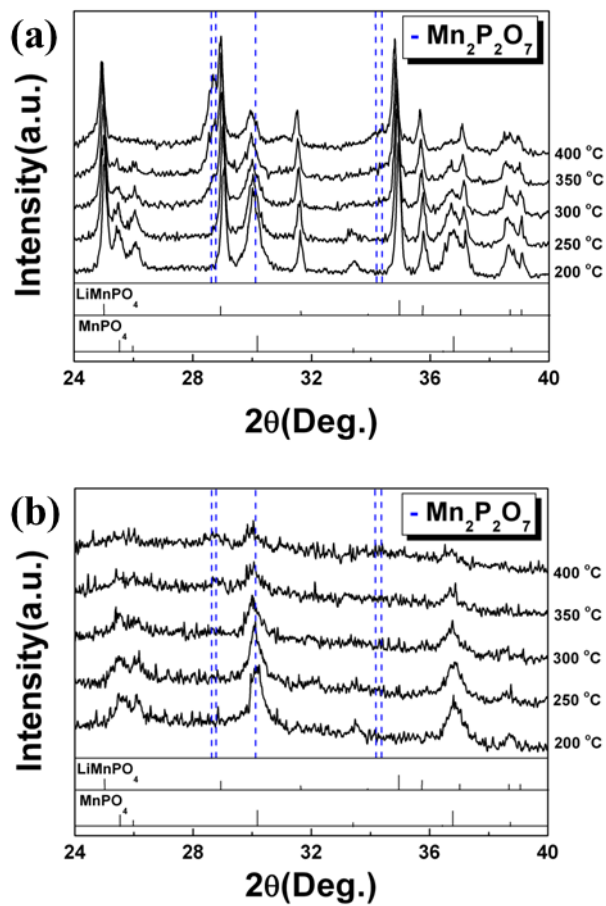


Figure 3.2.5 (a) *in-situ* XRD patterns of partially delithiated $\text{Li}_x\text{MnPO}_4\text{-700}$ at high temperature from 200°C to 400°C around $2\theta = 24^\circ \sim 40^\circ$, and (b) *in-situ* XRD patterns of fully delithiated $\text{Li}_x\text{MnPO}_4\text{-700}$ at high temperature from 200°C to 400°C around $2\theta = 24^\circ \sim 40^\circ$

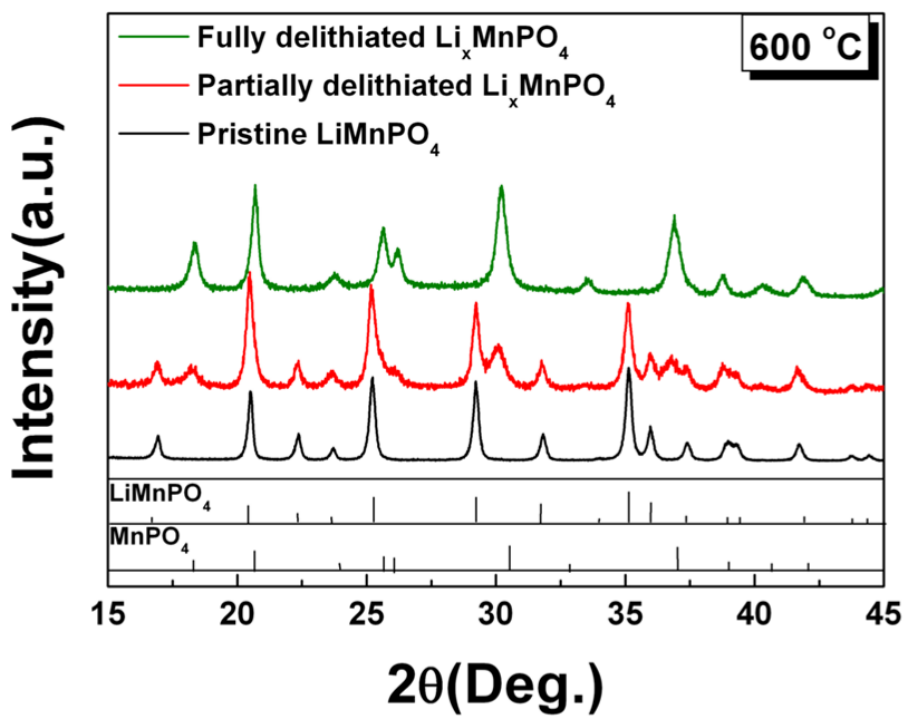


Figure 3.2.6 XRD patterns of Li_xMnPO_4 -600 [$0 \leq x \leq 1$]

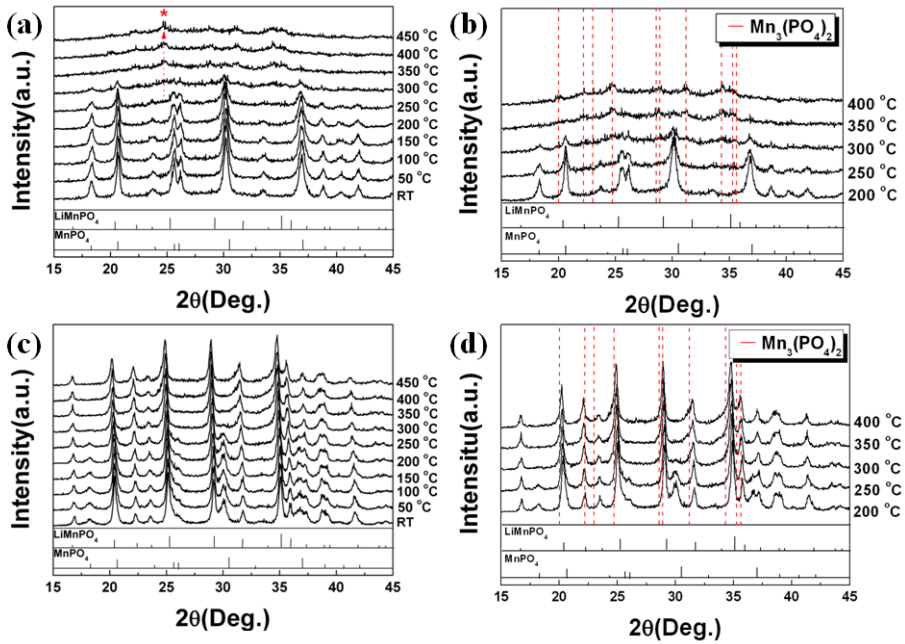


Figure 3.2.7 (a) *in-situ* XRD patterns of fully delithiated Li_xMnPO_4 -600 as temperature is increased up to 450°C around $2\theta = 15^\circ\sim 45^\circ$, (b) *in-situ* XRD patterns of fully delithiated Li_xMnPO_4 -600 at high temperature from 200°C to 400°C around $2\theta = 15^\circ\sim 45^\circ$, (c) *in-situ* XRD patterns of partially delithiated Li_xMnPO_4 -600 as temperature is increased up to 450°C around $2\theta = 15^\circ\sim 45^\circ$, and (d) *in-situ* XRD patterns of partial delithiated Li_xMnPO_4 -600 at high temperature from 200°C to 400°C around $2\theta = 15^\circ\sim 45^\circ$

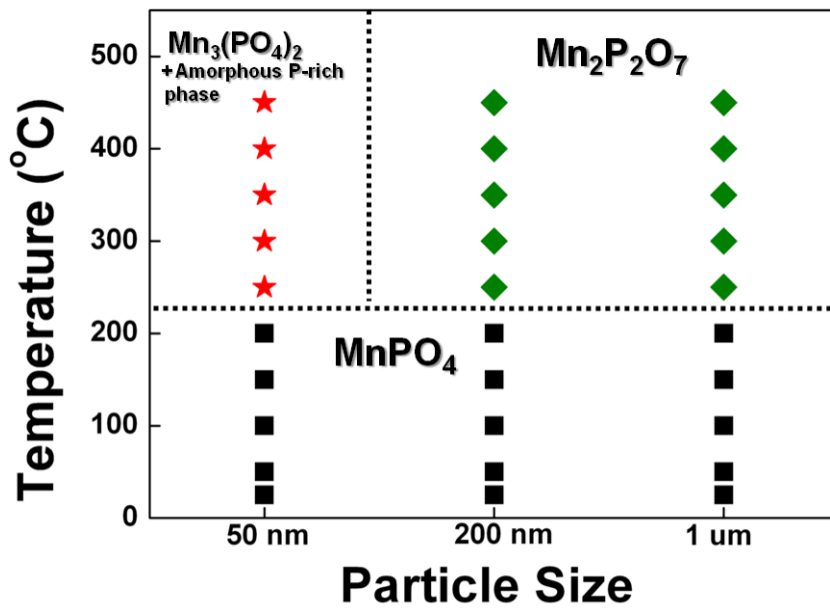


Figure 3.2.8 Phase stability of delithiated Li_xMnPO_4 as functions of particle size and temperature

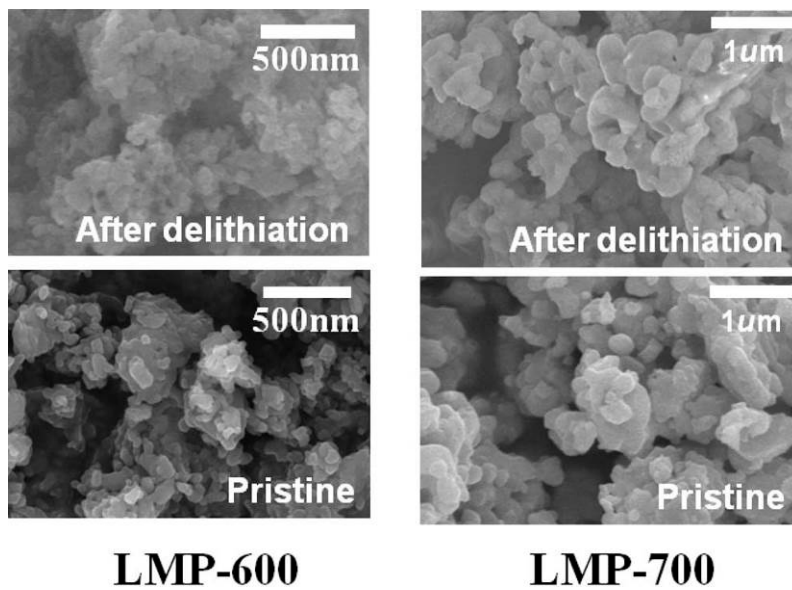


Figure 3.2.9 SEM images of pristine LiMnPO_4 and fully delithiated MnPO_4 synthesized at 600°C and 700°C (LMP-600 and 700)

3.2.6 References

- [1] A. K. Padhi, K. S. Nanjundaswamy, and J. B. Goodenough, *J. Electrochem. Soc.*, **144**, 1188 (1997).
- [2] H. Huang, S. C. Yin, and L. F. Nazar, *Electrochem. Solid State Lett.*, **4**, A170 (2001).
- [3] S. Y. Chung, J. T. Bloking, and Y. M. Chiang, *Nat. Mater.*, **1**, 123 (2002).
- [4] C. Delacourt, L. Laffont, R. Bouchet, C. Wurm, J. B. Leriche, M. Morcrette, J. M. Tarascon, and C. Masquelier, *J. Electrochem. Soc.*, **152**, A913 (2005).
- [5] A. Yamada, Y. Takei, H. Koizumi, N. Sonoyama, R. Kanno, K. Itoh, M. Yonemura, and T. Kamiyama, *Chem. Mat.*, **18**, 804 (2006).
- [6] J. Kim, D.-H. Seo, S. W. Kim, Y. U. Park, and K. Kang, *Chem. Commun.*, **46**, 1305 (2010).
- [7] Y.-U. Park, J. Kim, H. Gwon, D.-H. Seo, S.W. Kim, and K. Kang, *Chem. Mater.*, **22**, 2573 (2010).
- [8] J. Kim, Y. U. Park, D.-H. Seo, J. Kim, S.W. Kim, and K. Kang, *J. Electrochem. Soc.*, **158**, A250 (2011).
- [9] D.-H. Seo, H.Gwon, S.W. Kim, J. Kim, and K. Kang, *Chem. Mater.*, **22**, 518 (2010).
- [10] P. S. Herle, B. Ellis, N. Coombs, and L. F. Nazar, *Nat. Mater.*, **3**, 147

(2004).

[11] S. Y. Chung, J. G. Kim, Y. M. Kim, and Y. B. Lee, *Adv. Mater.*, **23**, 1398 (2011).

[12] Y. M. Wu, Z. H. Wen, and J. H. Li, *Adv. Mater.*, **23**, 1126 (2011).

[13] G. H. Li, H. Azuma, and M. Tohda, *Electrochem. Solid State Lett.*, **5**, A135 (2002).

[14] M. Yonemura, A. Yamada, Y. Takei, N. Sonoyama, and R. Kanno, *J. Electrochem. Soc.*, **151**, A1352 (2004).

[15] H. Gwon, D.-H. Seo, S. W. Kim, J. Kim, and K. Kang, *Adv. Funct. Mater.*, **19**, 3285 (2009).

[16] S. K. Martha, B. Markovskiy, J. Grinblat, Y. Gofer, O. Haik, E. Zinigrad, D. Aurbach, T. Drezen, D. Wang, G. Deghenghi, and I. Exnar, *J. Electrochem. Soc.*, **156**, A541 (2009).

[17] S.-W. Kim, J. Kim, H. Gwon, and K. Kang, *J. Electrochem. Soc.*, **156**, A635 (2009).

[18] G. Y. Chen and T. J. Richardson, *J. Power Sources*, **195**, 1221 (2010).

[19] S. P. Ong, A. Jain, G. Hautier, B. Kang, and G. Ceder, *Electrochem. Commun.*, **12**, 427 (2010).

[20] R. Malik, D. Burch, M. Bazant, and G. Ceder, *Nano Lett.*, **10**, 4123 (2011).

- [21] J. K. Warner, A. K. Cheetham, A. G. Nord, R. B. Vondreele, and M. Yethiraj, *J. Mater. Chem.*, **2**, 191 (1992).
- [22] J. P. Perdew, K. Burke, and M. Ernzerhof, *Phys. Rev. Lett.*, **77**, 3865 (1996).
- [23] G. Kresse and J. Furthmuller, *Comput. Mater. Sci.*, **6**, 15 (1996).
- [24] K. Kang, Y. S. Meng, J. Breger, C. P. Grey, and G. Ceder, *Science*, **311**, 977 (2006).
- [25] K. Kang, D. Morgan, and G. Ceder, *Phys. Rev. B*, **79**, 014305 (2009).
- [26] F. Zhou, K. S. Kang, T. Maxisch, G. Ceder, and D. Morgan, *Solid State Commun.*, **132**, 181 (2004).
- [27] <http://www.icdd.com>.
- [28] A. Navrotsky, *Geochem. Trans.*, **4**, 34 (2003).
- [29] A. Navrotsky, C. C. Ma, K. Lilova, and N. Birkner, *Science*, **330**, 199 (2010).
- [30] L. Wang, F. Zhou, and G. Ceder, *Electrochem. Solid State Lett.*, **11**, A94 (2008).
- [31] S. P. Ong, First Principles Design and Investigation of Lithium-Ion Battery Cathodes and Electrolytes, in *Department of Materials Science and Engineering*, Massachusetts Institute of Technology (2011).

3.3 Thermal stability of Fe-Mn binary olivine cathode for Li rechargeable battery

3.3.1 Research Background

Lithium transition metal phosphate LiMPO_4 ($M = \text{Mn, Fe, Co, Ni}$) with an olivine structure is one of the most promising cathode candidates for lithium rechargeable batteries.[1-7] As the need for cheap, stable, and safe energy storage becomes unprecedentedly high due to the development of various types of electric vehicles and the large-scale energy storage systems for renewable energy sources, lithium ion batteries based on LiMPO_4 cathodes are attracting much attention. In particular, naturally abundant Fe or Mn containing olivine LiMPO_4 has been most thoroughly investigated.[8-11] The stable nature of the olivine-type structure with a $(\text{PO}_4)^{3-}$ poly-anion and a strong P-O covalent bond provides an excellent cycle-life in a safe manner. Moreover, a very high power capability has been demonstrated for LiFePO_4 cathodes.[3, 12-14] However, single component LiFePO_4 suffers from the intrinsic low energy density due to its relatively low $\text{Fe}^{2+}/\text{Fe}^{3+}$ redox potential (*ca.* 3.4 V vs. Li^+/Li).[4, 6, 15, 16] On the other hand, LiMnPO_4 can theoretically deliver a higher energy density due to the high redox potential of $\text{Mn}^{2+}/\text{Mn}^{3+}$ (*ca.* 4.1V vs. Li^+/Li), while its power capability is significantly reduced. To counterbalance such an effect, binary $\text{Li}(\text{Fe, Mn})\text{PO}_4$ olivine

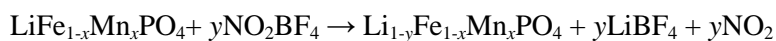
cathodes have been explored by researchers.[8, 9, 12] Recent works have shown that the electrochemical properties of binary Li(Fe, Mn)PO₄ cathodes are sensitively dependent on the Fe/Mn ratio in the material.[8-11] Power capability, energy density, and even the charge/discharge mechanism (one-phase vs. two-phase) vary with different Fe/Mn ratios clearly indicating that the optimal composition of Fe/Mn in the binary Li(Fe, Mn)PO₄ needs to be determined.[2, 8, 17-19]

In the present work, the phase stability of binary LiFe_{1-x}Mn_xPO₄ [x = 0, 0.25, 0.5, 0.75, 1] was investigated with different Li compositions and temperatures with temperature-controlled *in situ* XRD. Since the safety and stability of the battery is strongly influenced by the phase stability of the cathode at different SOCs and temperatures, this work can provide useful information in determining the optimal composition of binary Li(Fe, Mn)PO₄ cathodes. Earlier work on the thermal stability of single component LiFePO₄ and LiMnPO₄ with experiments and computation[20-23] showed that both LiFePO₄ and LiMnPO₄ remains stable up to fairly high temperatures, however, partially or fully delithiated Li_xMnPO₄ decomposes at *ca.* 200°C with O₂ evolution and heat generation in the process, while delithiated FePO₄ is stable until *ca.* 500°C.[20-22] In this study, we were able to confirm the higher stability of FePO₄ compared to MnPO₄, and

further demonstrate the difference in the relative stabilities of the phases in delithiated $\text{LiFe}_{1-x}\text{Mn}_x\text{PO}_4$ with comparative analyses of the *in situ* XRD patterns using different Fe/Mn ratios in LiMPO_4 .

3.3.2 Experimental Section

$\text{LiFe}_{1-x}\text{Mn}_x\text{PO}_4$ powder was synthesized using the conventional solid-state synthesis. Li_2CO_3 (Junsei Chemical, 98%), $\text{Mn}(\text{CH}_3\text{COO})_2 \cdot 4\text{H}_2\text{O}$ (Junsei Chemical, 98%), $\text{FeC}_2\text{O}_4 \cdot 2\text{H}_2\text{O}$ (Sigma Aldrich, 98%), and $\text{NH}_4\text{H}_2\text{PO}_4$ (Fluka, 98%) with molar ratios of $0.5 : x : 1-x : 1$ ($x = 0, 0.25, 0.5, 0.75, \text{ and } 1$) were used as precursors. They were dispersed into acetone, thoroughly mixed, and ground by wet ball-milling. After evaporating the acetone, the precursors were then fired at 350°C under Ar conditions for 3 hours. The mixture was then re-ground and manually pelletized using a disk-shaped mold. After pre-heating, we calcined the pellets at 600°C under Ar conditions for 10 hours. To prepare the $\text{LiFe}_{1-x}\text{Mn}_x\text{PO}_4$ samples, the synthesized $\text{LiFe}_{1-x}\text{Mn}_x\text{PO}_4$ was chemically delithiated by NO_2BF_4 (Aldrich, 95%) according to the following reaction.



NO_2BF_4 is a strong oxidizing agent with a high redox potential of $\text{NO}_2^+/\text{NO}_2$ at 5.1V vs. Li^+/Li . The composition of $\text{LiFe}_{1-x}\text{Mn}_x\text{PO}_4$ was controlled by governing the time of the reaction between the $\text{LiFe}_{1-x}\text{Mn}_x\text{PO}_4$ and NO_2BF_4

with a molar ratio of 1 : 1 in acetonitrile (Aldrich, 98%) in an Ar-filled glove box. The stoichiometry of the delithiated compound was determined by inductively coupled plasma-atomic emission spectroscopy (ICP-AES). The atomic ratios of Li, Fe, and Mn in as prepared, partially delithiated, and fully delithiated $\text{Li}_{1-y}\text{Fe}_{1-x}\text{Mn}_x\text{PO}_4$ ($x = 0, 0.25, 0.5, 0.75, \text{ and } 1; 0 \leq y \leq 1$) are summarized in Table 3.3.1. The crystal structure was determined by XRD (Rigaku D/Max 2500) with Cu K α radiation ($\lambda = 1.54178\text{\AA}$) operating at 30kV and 400mA. For the temperature-dependent phase stability study, samples were heated from 25°C to 700°C in a vacuum during the XRD investigation. The heating rate was 5°C min⁻¹; the waiting time between heating and measurement was 3min, and the scan speed was 1° min⁻¹. Structural refinements were done by the Rietveld method with a general structure analysis system (GSAS).

3.3.3 Computational Details

The hypothetical $(\text{Fe}_{1-x}\text{Mn}_x)_3(\text{PO}_4)_2$ and $(\text{Fe}_{1-x}\text{Mn}_x)_2\text{P}_2\text{O}_7$ ($x = 0.25, 0.5, \text{ and } 0.75$) structures were calculated from the first principles, starting from the $\text{Fe}_3(\text{PO}_4)_2$ and $\text{Fe}_2\text{P}_2\text{O}_7$ structures.[26] Calculations were done on the entire Fe/Mn ordered configurations to find the most stable structure of the solid solution. The spinpolarized generalized gradient approximation (GGA) was applied with the Perdew–Burke–Ernzerhof exchange-correlation

parameterization [27] for the density functional theory (DFT). A plane-wave basis set and the projector-augmented wave (PAW) method were used as implemented in the Vienna ab initio simulation package (VASP).[28] PAW potentials have been widely used for battery materials and have shown good predictive capability.[29–32] Planewave bases with a kinetic energy cutoff of 500 eV were used, and appropriate k-point meshes were chosen to ensure that the total energy converged within 5 meV per formula unit.

3.3.4 Results and Discussion

The XRD patterns of the as-prepared $\text{LiFe}_{1-x}\text{Mn}_x\text{PO}_4$ [$x = 0, 0.25, 0.5, 0.75, 1$] are shown in Figure 3.3.1. Phase-pure olivine materials were identified from the powder XRD measurements. No noticeable impurity or second phase was observed in the XRD pattern of each sample. The solid solution between LiMnPO_4 and LiFePO_4 was confirmed at $0 \leq x \leq 1$ of $\text{LiFe}_{1-x}\text{Mn}_x\text{PO}_4$ with continuous variations in the lattice parameters a , b , and c as tabulated in Table. 3.3.2.[2, 17] The small difference in lattice parameters among $\text{LiFe}_{1-x}\text{Mn}_x\text{PO}_4$ was caused by the different ionic radii of Mn^{2+} and Fe^{2+} ($\text{Mn}^{2+} > \text{Fe}^{2+}$) and their composition ratio in the materials.[7, 29, 31]

The thermal stability of the as-prepared $\text{LiFe}_{1-x}\text{Mn}_x\text{PO}_4$ series was first examined. Figure 3.3.2 shows the XRD patterns of each $\text{LiFe}_{1-x}\text{Mn}_x\text{PO}_4$ measured from 25°C to 700°C. No noticeable phase transformation was

observed up to 700°C. Only the thermal expansion of the olivine crystal $\text{LiFe}_{1-x}\text{Mn}_x\text{PO}_4$ was detected from the shift of the XRD peaks at elevated temperatures. The quantitative analysis of the lattice parameter change from the Rietveld refinement is shown in Figure 3.3.3 with the thermal coefficients tabulated in Table 3.3.3. Linear thermal coefficients of a , b , and c lattices and the volumes' thermal coefficients of the $\text{Li}_{1-y}\text{Fe}_{1-x}\text{Mn}_x\text{PO}_4$ samples were all within the same orders of magnitude.

The delithiated samples of $\text{Li}_{1-y}\text{Fe}_{1-x}\text{Mn}_x\text{PO}_4$ were prepared from the chemical method as described in the experimental section. It was observed that the delithiation process generally took longer with higher contents of Mn in the sample, which is in agreement with the fact that Mn-rich olivine cathodes usually exhibit a low power capability.[16] The delithiation mechanism of $\text{Li}_{1-y}\text{Fe}_{1-x}\text{Mn}_x\text{PO}_4$ at 25°C was monitored by the XRD patterns, as shown in Figure 3.3.4. Similar to previous reports,[20, 21] the delithiation mechanism of the two-phase reaction was observed with the single component olivine (LiFePO_4 and LiMnPO_4). However, the binary component olivine showed a mixed behavior of one-phase and two-phase reactions. Delithiation of $\text{LiFe}_{0.5}\text{Mn}_{0.5}\text{PO}_4$ and $\text{LiFe}_{0.25}\text{Mn}_{0.75}\text{PO}_4$ exhibited the growth of a new phase ($\text{Fe}_{0.5}\text{Mn}_{0.5}\text{PO}_4$ and $\text{Fe}_{0.25}\text{Mn}_{0.75}\text{PO}_4$) accompanied with an apparent XRD peak shift of the mother phase ($\text{LiFe}_{0.5}\text{Mn}_{0.5}\text{PO}_4$ and

LiFe_{0.25}Mn_{0.75}PO₄).[17] In the case of LiFe_{0.75}Mn_{0.25}PO₄, the XRD peaks were continuously shifted with delithiation and no emerging new XRD peaks from the second phases was observed.

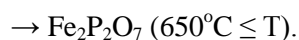
In the following sections, we evaluated the thermal characteristics of Li_{1-y}Fe_{1-x}Mn_xPO₄ using these prepared samples.

3.3.4.1 Revisit of Li_{1-y}FePO₄ and Li_{1-y}MnPO₄ (0 < y ≤ 1)

Figure 3.3.5(a) shows the *in situ* XRD patterns of fully delithiated FePO₄ with temperatures ranging from 25°C to 700°C. While the FePO₄ phase retained its original XRD pattern from 25°C to 450°C, it started to decompose into a new phase at 500°C. As shown in Figure 3.3.5(b), at 500 °C, a new phase with main peaks located at 25°, 29°, 31°, and 35° arose, which correspond to the typical XRD pattern of Fe₃(PO₄)₂.

The XRD peaks for Fe₃(PO₄)₂ disappeared at 600°C, and those of Fe₂P₂O₇ started to appear and grow at this temperature. Especially, the growth of Fe₂P₂O₇ was remarkably clear at *ca.* 29°, which is the main XRD peak of Fe₂P₂O₇. This observation agrees with the first principles study of thermal stability of FePO₄ by Ong *et al.* that reported a three-step decomposition: FePO₄ → 0.1(Fe₇(PO₄)₆ + Fe₃(P₂O₇)₂) → 0.167(Fe₃(PO₄)₂ + Fe₃(P₂O₇)₂) → 0.5Fe₂P₂O₇. [23] Although we did not observe the first step of the decomposition they predicted, the second and the final steps of the

decomposition indicate the sequential formation of $\text{Fe}_3(\text{PO}_4)_2$ and $\text{Fe}_2\text{P}_2\text{O}_7$ consistent with our observation. Nevertheless, we could not with certainty determine the $\text{Fe}_3(\text{P}_2\text{O}_7)_2$ phase. The decomposition of FePO_4 into $\text{Fe}_3(\text{PO}_4)_2$ would result in an imbalance of the Fe : P stoichiometry. Thus, another new P-rich phase has to be formed. However, it was not possible to clearly define a new P-rich phase indicating that amorphization had occurred to some extent at the phase transition. It should be noted that compositions with high phosphorous content are known to be very good glass formers.[32] Finally, from the above data, we propose that the decomposition mechanism of FePO_4 is as follows:



The *in situ* XRD results of the partially delithiated $\text{Li}_{0.6}\text{FePO}_4$ at temperatures ranging from 25°C to 700°C are shown in Figure 3.3.6(a). While fully lithiated LiFePO_4 exhibited a high thermal stability, it was observed that delithiated $\text{Li}_{0.6}\text{FePO}_4$ [= $0.6\text{LiFePO}_4 + 0.4\text{FePO}_4$ at 25°C] was

susceptible to phase transitions at high temperatures. Figure 3.3.6(b) shows the XRD patterns of $\text{Li}_{0.6}\text{FePO}_4$ from 300°C to 400°C. When the temperature was elevated to *ca.* 400°C, the XRD patterns of both LiFePO_4 and FePO_4 started to merge with the appearance of broad patterns for the solid solution phase.[20]

At the temperatures higher than *ca.* 600°C, the solid solution $\text{Li}_{0.6}\text{FePO}_4$ phase began to decompose into a non-olivine phases leaving the fully lithiated olivine phase (LiFePO_4) behind, as shown in Figure 3.3.6(c). The emerging of non-olivine peaks at *ca.* 30° becomes clear at or above 600°C. In addition, it should be noted that the solid solution $\text{Li}_{0.6}\text{FePO}_4$ pattern became very similar to that of LiFePO_4 at or above 600°C. The change in XRD patterns from solid solution to fully lithiated LiFePO_4 was easily observed at 2θ ranging between 37° and 40°. The comparison of the lattice parameter as a function of temperature in Figure 3.3.6(d) clearly demonstrates the formation of LiFePO_4 from the $\text{Li}_{0.6}\text{FePO}_4$ solid solution around 550°C~600°C. Besides the formation of fully lithiated LiFePO_4 in the XRD pattern, XRD peaks of non-olivine phases were observed at several points, shown in Figure 3.3.6(e). Previously, Delacourt *et al.* reported the partially delithiated $\text{Li}_{1-y}\text{FePO}_4$ decomposes into $\text{Fe}_7(\text{PO}_4)_6$ (PDF#35-0282).[20] However, except for the XRD peaks of *ca.* 29°, and 35°, the main

XRD peaks of $\text{Fe}_7(\text{PO}_4)_6$ did not correspond with those of non-olivine phases at 700°C . Instead, we observed that these XRD peaks were similar to those of reference $\text{Fe}_2\text{P}_2\text{O}_7$ (ICSD ID 16531) or those of decomposition product of FePO_4 at 700°C , which is equivalent to $\text{Fe}_2\text{P}_2\text{O}_7$. It means that the solid solution $\text{Li}_{0.6}\text{FePO}_4$ decomposes into a mixture of LiFePO_4 and $\text{Fe}_2\text{P}_2\text{O}_7$ at 600°C . Finally, we propose that the reaction mechanism of $\text{Li}_{0.6}\text{FePO}_4$ upon heating is as follows.

$\text{Li}_{0.6}\text{FePO}_4$ (two-phase of LiFePO_4 and FePO_4 , $25^\circ\text{C} \leq T < 400^\circ\text{C}$)

→ $\text{Li}_{0.6}\text{FePO}_4$ (solid solution, $400^\circ\text{C} \leq T < 600^\circ\text{C}$)

→ $\text{LiFePO}_4 + \text{Fe}_2\text{P}_2\text{O}_7$ ($600^\circ\text{C} \leq T$)

Figure 3.3.7(a) shows the *in situ* XRD patterns of fully delithiated MnPO_4 at temperatures between 25°C and 700°C . At low temperatures from 25°C to 200°C , no noticeable phase transition was observed. However, at temperatures above 200°C , the MnPO_4 phase decomposed into a new non-olivine phase. Figure 3.3.7(b) shows the XRD patterns of MnPO_4 from 200°C to 400°C . At this temperature range, $\text{Mn}_3(\text{PO}_4)_2$ (main peak at *ca.* 25°) was consistent with the previous report.[33] Similar to the decomposition of FePO_4 into $\text{Fe}_3(\text{PO}_4)_2$, the decomposition of MnPO_4 into $\text{Mn}_3(\text{PO}_4)_2$ would

also result in an imbalance of the Mn : P stoichiometry. We expect that an amorphous P-rich phase not detectable by XRD would have formed during the decomposition to compensate for the imbalance of composition. A further increase of the temperature completely amorphized the sample at 550°C followed by the formation of $\text{Mn}_2\text{P}_2\text{O}_7$ at 600°C, shown in Figure 3.3.7(c). From the above data, we propose that the decomposition mechanism of MnPO_4 upon heating is as follows:

MnPO_4 ($25^\circ\text{C} \leq T < 250^\circ\text{C}$)

→ $\text{MnPO}_4 + \text{Mn}_3(\text{PO}_4)_2 + \text{amorphous P-rich phase}$ ($250^\circ\text{C} \leq T < 300^\circ\text{C}$)

→ $\text{Mn}_3(\text{PO}_4)_2 + \text{amorphous P-rich phase}$ ($300^\circ\text{C} \leq T < 550^\circ\text{C}$)

→ Amorphous phase ($550^\circ\text{C} \leq T < 600^\circ\text{C}$)

→ $\text{Mn}_2\text{P}_2\text{O}_7$ ($600^\circ\text{C} \leq T$)

Figure 3.3.8(a) shows the *in situ* XRD patterns of the partially delithiated $\text{Li}_{0.5}\text{MnPO}_4$ from 25°C to 700°C. The coexistence of LiMnPO_4 and MnPO_4 was observable due to the two-phase reaction in the delithiation of LiMnPO_4 . The phase transition of partially delithiated $\text{Li}_{0.5}\text{MnPO}_4$ occurred from 250°C shown in Figure 3.3.8(b). Instead of forming a solid solution of $\text{Li}_{0.5}\text{MnPO}_4$ as observed for $\text{Li}_{0.6}\text{FePO}_4$, the fully delithiated phase ($=\text{MnPO}_4$) gradually

disappeared and the $\text{Mn}_3(\text{PO}_4)_2$ phase appeared at the expense of MnPO_4 . The formation of $\text{Mn}_3(\text{PO}_4)_2$ is consistent with the decomposition case of the fully delithiated MnPO_4 sample. At 550°C , $\text{Mn}_2\text{P}_2\text{O}_7$ was finally formed from $\text{Mn}_3(\text{PO}_4)_2$, shown in Figure 3.3.8(c). In summary, we propose that the decomposition mechanism of $\text{Li}_{0.5}\text{MnPO}_4$ at elevated temperatures is as follows:

$\text{Li}_{0.5}\text{MnPO}_4$ (two-phase of LiMnPO_4 and MnPO_4 , $25^\circ\text{C} \leq T < 250^\circ\text{C}$)

→ $\text{Li}_{0.5}\text{MnPO}_4 + \text{Mn}_3(\text{PO}_4)_2 + \text{amorphous P-rich phase}$ ($250^\circ\text{C} \leq T < 300^\circ\text{C}$)

→ $\text{LiMnPO}_4 + \text{Mn}_3(\text{PO}_4)_2 + \text{amorphous P-rich phase}$ ($300^\circ\text{C} \leq T < 550^\circ\text{C}$)

→ $\text{LiMnPO}_4 + \text{Mn}_2\text{P}_2\text{O}_7$ ($550^\circ\text{C} \leq T$)

3.3.4.2 Phase stability of Fe–Mn binary olivine at elevated temperatures

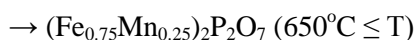
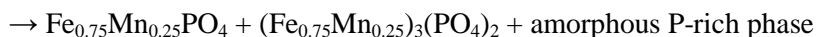
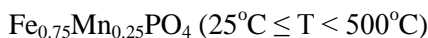
3.3.4.2.1 $\text{Li}_{1-y}\text{Fe}_{0.75}\text{Mn}_{0.25}\text{PO}_4$ ($0 < y \leq 1$).

Figure 3.3.9(a) shows the *in situ* XRD patterns of fully delithiated $\text{Fe}_{0.75}\text{Mn}_{0.25}\text{PO}_4$ at temperatures from 25°C to 700°C . From 25°C to 450°C , no other phase except for $\text{Fe}_{0.75}\text{Mn}_{0.25}\text{PO}_4$ was detected. However, $\text{Fe}_{0.75}\text{Mn}_{0.25}\text{PO}_4$ began to decompose into new non-olivine phases from 500°C . As shown in Figure 3.3.9(b), the peaks at *ca.* 25° , 29° , 31° , and 35° became embossed at 500°C . These peaks corresponded to the general XRD

patterns of $M_3(PO_4)_2$ ($M = Fe$ or Mn) from the ICSD (Inorganic Crystal Structure Database). At this point, it is not clear if $Fe_{0.75}Mn_{0.25}PO_4$ decomposed into a mixture of $Fe_3(PO_4)_2$ and $Mn_3(PO_4)_2$ or a solid solution $(Fe_{0.75}Mn_{0.25})_3(PO_4)_2$. However, it appears that the observed peaks do not exactly match with either of $Fe_3(PO_4)_2$ or $Mn_3(PO_4)_2$ but lie between those 2 patterns. This strongly implies that a solid solution, $(Fe_{0.75}Mn_{0.25})_3(PO_4)_2$, had formed. In order to confirm this, we did a DFT (Density Functional Theory) calculation on the $(Fe_{0.75}Mn_{0.25})_3(PO_4)_2$ to predict its crystal structure and generated an XRD pattern from the structure. The dotted line in Figure 3.3.9(b) is the XRD pattern for the hypothetical $(Fe_{0.75}Mn_{0.25})_3(PO_4)_2$, which perfectly agrees with the observation. Therefore, we suppose that $Fe_{0.75}Mn_{0.25}PO_4$ decomposed into $(Fe_{0.75}Mn_{0.25})_3(PO_4)_2$. As in the case of $FePO_4$ and $MnPO_4$, the decomposition of $Fe_{0.75}Mn_{0.25}PO_4$ into $(Fe_{0.75}Mn_{0.25})_3(PO_4)_2$ resulted in an imbalance of the (Fe, Mn) : P stoichiometry. Thus, the formation of amorphous P-rich phase is expected.

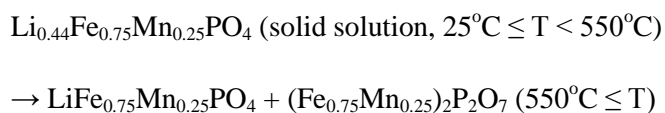
With a further increase of the temperature, new peaks at *ca.* 29° and 35° (characteristic of $M_2P_2O_7$ ($M = Fe$ or Mn) XRD pattern) dominantly grew with the disappearance of $(Fe_{0.75}Mn_{0.25})_3(PO_4)_2$ at $550^\circ C$. This behavior is analogous to the decomposition mechanism of $Fe_3(PO_4)_2$ to $Fe_2P_2O_7$ for $FePO_4$, but different from $MnPO_4$, which decomposes into $Mn_2P_2O_7$ after the

amorphization of the material. The observed XRD peaks also did not exactly match with either of $\text{Fe}_2\text{P}_2\text{O}_7$ or $\text{Mn}_2\text{P}_2\text{O}_7$. Instead, we calculated the crystal structure of the hypothetical $(\text{Fe}_{0.75}\text{Mn}_{0.25})_2\text{P}_2\text{O}_7$ from the DFT calculation and generated the XRD pattern. The calculated XRD pattern (dotted line in Figure 3.3.9(c)) perfectly agrees with the observed XRD pattern. Finally, from the above data on $\text{Fe}_{0.75}\text{Mn}_{0.25}\text{PO}_4$, we propose that the decomposition mechanism of $\text{Fe}_{0.75}\text{Mn}_{0.25}\text{PO}_4$ upon heating to 700°C is as follows:



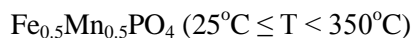
The thermal behavior of partially delithiated $\text{Li}_{0.44}\text{Fe}_{0.75}\text{Mn}_{0.25}\text{PO}_4$ was investigated with the temperature-controlled *in situ* XRD shown in Figure 3.3.10(a). Unlike the aforementioned single component olivines, the partial delithiation ($\text{Li} \approx 0.44$) of $\text{LiFe}_{0.75}\text{Mn}_{0.25}\text{PO}_4$ resulted in a single phase at

25°C.[17] Heating of this sample until 500°C did not induce any noticeable phase transformation demonstrating its high thermal stability. Only the thermal expansion of the olivine crystal $\text{Li}_{0.44}\text{Fe}_{0.75}\text{Mn}_{0.25}\text{PO}_4$ was observed as indicated by the shift of the XRD peaks at elevated temperatures. However, Figure 3.3.10(b) shows that the single phase $\text{Li}_{0.44}\text{Fe}_{0.75}\text{Mn}_{0.25}\text{PO}_4$ separated into fully lithiated olivine [$\text{LiFe}_{0.75}\text{Mn}_{0.25}\text{PO}_4$] and non-olivine phases from 550°C analogous to the behavior of the partially delithiated $\text{Li}_{1-y}\text{FePO}_4$. An abrupt shift of the XRD peaks was observed with increasing temperatures from 500°C to 600°C, which coincides with the formation of the $\text{M}_2\text{P}_2\text{O}_7$ (M = Fe, Mn) phase. The shifted XRD peaks corresponded to the fully lithiated $\text{LiFe}_{0.75}\text{Mn}_{0.25}\text{PO}_4$. The thermal decomposition at 550°C resulted in $\text{M}_2\text{P}_2\text{O}_7$ (M = Fe, Mn) with its XRD peaks different from either $\text{Fe}_2\text{P}_2\text{O}_7$ or $\text{Mn}_2\text{P}_2\text{O}_7$. These XRD peaks corresponded to the $(\text{Fe}_{0.75}\text{Mn}_{0.25})_2\text{P}_2\text{O}_7$ structure that we predicted from the DFT calculation in Figure 3.3.10(b). From the data above, we propose that the decomposition mechanism of $\text{Li}_{0.44}\text{Fe}_{0.75}\text{Mn}_{0.25}\text{PO}_4$ at elevated temperatures is as follows:



3.3.4.2.2 $\text{Li}_{1-y}\text{Fe}_{0.5}\text{Mn}_{0.5}\text{PO}_4$ [$0 < y \leq 1$]

The thermal behavior of fully delithiated $\text{Fe}_{0.5}\text{Mn}_{0.5}\text{PO}_4$ was monitored shown in Figure 3.3.11(a). The overall decomposition mechanism of $\text{Fe}_{0.5}\text{Mn}_{0.5}\text{PO}_4$ appeared to be similar to that of $\text{Fe}_{0.75}\text{Mn}_{0.25}\text{PO}_4$ except that the decomposition began at a relatively lower temperature of 350°C . Figure 3.3.11(b) shows that $\text{Fe}_{0.5}\text{Mn}_{0.5}\text{PO}_4$ decomposed into $(\text{Fe}_{0.5}\text{Mn}_{0.5})_3(\text{PO}_4)_2$ from 350°C . The emerging peaks in the XRD pattern at this temperature corresponded with the hypothetical $(\text{Fe}_{0.5}\text{Mn}_{0.5})_3(\text{PO}_4)_2$ structure from the DFT calculation. When the temperature rose to 550°C , new XRD peaks such as *ca.* 29° and *ca.* 35° started to grow. We also found that they were close to the calculated XRD peaks of the hypothetical $(\text{Fe}_{0.5}\text{Mn}_{0.5})_2\text{P}_2\text{O}_7$ structure predicted from the DFT calculation, shown in Figure 3.3.11(c). Thereafter, the $(\text{Fe}_{0.5}\text{Mn}_{0.5})_2\text{P}_2\text{O}_7$ phase grew at the expense of $\text{Fe}_{0.5}\text{Mn}_{0.5}\text{PO}_4$ and $(\text{Fe}_{0.5}\text{Mn}_{0.5})_3(\text{PO}_4)_2$. It should be noted that slightly higher Mn contents (25% vs. 50%) in binary olivines significantly lowers the decomposition temperature of the delithiated phase from 500°C to 350°C . Finally, we propose that reaction mechanism of $\text{Fe}_{0.5}\text{Mn}_{0.5}\text{PO}_4$ at elevated temperatures is as follows:



→ $\text{Fe}_{0.5}\text{Mn}_{0.5}\text{PO}_4 + (\text{Fe}_{0.5}\text{Mn}_{0.5})_3(\text{PO}_4)_2 + \text{amorphous P-rich phase}$ ($350^\circ\text{C} \leq T < 550^\circ\text{C}$)

→ $(\text{Fe}_{0.5}\text{Mn}_{0.5})_3(\text{PO}_4)_2 + \text{amorphous P-rich phase} + (\text{Fe}_{0.5}\text{Mn}_{0.5})_2\text{P}_2\text{O}_7$ ($550^\circ\text{C} \leq T < 600^\circ\text{C}$)

→ $(\text{Fe}_{0.5}\text{Mn}_{0.5})_2\text{P}_2\text{O}_7$ ($600^\circ\text{C} \leq T$)

Figure 3.3.12(a) shows the thermal behavior of the partially delithiated $\text{Li}_{0.4}\text{Fe}_{0.5}\text{Mn}_{0.5}\text{PO}_4$ phase from 25°C to 700°C . Dissimilar to the partially delithiated $\text{Li}_{0.44}\text{Fe}_{0.75}\text{Mn}_{0.25}\text{PO}_4$, which was a single phase at 25°C , the $\text{Li}_{0.4}\text{Fe}_{0.5}\text{Mn}_{0.5}\text{PO}_4$ exhibited a two-phase mixture of $\text{LiFe}_{0.5}\text{Mn}_{0.5}\text{PO}_4$ and $\text{Fe}_{0.5}\text{Mn}_{0.5}\text{PO}_4$. However, with a slight increase in the temperature, the two phases merged into a single phase shown in Figure 3.3.12(b). Once the solid solution phase of $\text{Li}_{0.4}\text{Fe}_{0.5}\text{Mn}_{0.5}\text{PO}_4$ was formed, its decomposition path (Figure 3.3.12(c)) became analogous to that of $\text{Li}_{0.44}\text{Fe}_{0.75}\text{Mn}_{0.25}\text{PO}_4$, where the mixture of the fully lithiated olivine phase and $\text{M}_2\text{P}_2\text{O}_7$ ($\text{M}=\text{Fe}, \text{Mn}$) appeared at 550°C . An abrupt shift of the XRD peaks (dotted area in Figure 3.3.12(a)) was observed with increasing temperatures from 500°C to 600°C , which coincide with the formation of the $\text{M}_2\text{P}_2\text{O}_7$ ($\text{M}=\text{Fe}, \text{Mn}$) phase. The shifted XRD peaks corresponded to the fully lithiated $\text{LiFe}_{0.5}\text{Mn}_{0.5}\text{PO}_4$. The DFT calculation confirmed that the XRD pattern of the decomposition

product, $M_2P_2O_7$, matched well with that of the hypothetical $(Fe_{0.5}Mn_{0.5})_2P_2O_7$. Overall, the thermal decomposition mechanism of $Li_{0.4}Fe_{0.5}Mn_{0.5}PO_4$ upon heating from 25°C to 700°C is proposed as the following reactions:

$Li_{0.4}Fe_{0.5}Mn_{0.5}PO_4$ (solid solution + two-phase reaction, $25^\circ C \leq T < 250^\circ C$)

→ $Li_{0.4}Fe_{0.5}Mn_{0.5}PO_4$ (solid solution, $250^\circ C \leq T < 550^\circ C$)

→ $LiFe_{0.5}Mn_{0.5}PO_4 + (Fe_{0.5}Mn_{0.5})_2P_2O_7$ ($550^\circ C \leq T$)

3.3.4.2.3 $Li_{1-y}Fe_{0.25}Mn_{0.75}PO_4$ [$0 < y \leq 1$]

Figure 3.3.13(a) shows the *in situ* XRD patterns of fully delithiated $Fe_{0.25}Mn_{0.75}PO_4$ at temperatures ranging from 25°C to 700°C. From 25°C to 250°C, noticeable changes in the XRD pattern were not observed similar to the other delithiated $Fe_{1-x}Mn_xPO_4$ samples. However, upon heating higher than 300°C, new XRD peaks appeared. As shown in Figure 3.3.13(b) and 3.3.13(c), $Fe_{0.25}Mn_{0.75}PO_4$ decomposed into the hypothetical $(Fe_{0.25}Mn_{0.75})_3(P_2O_7)_2$ whose structure was calculated from the DFT calculation. This behavior is consistent with the other $Fe_{1-x}Mn_xPO_4$. However, it should be noted that the decomposition temperature significantly decreased from 550°C to 300°C. This strongly suggests the disadvantage of

high Mn content binary olivines in terms of phase stability. In addition, it should be emphasized that the Mn effect on inferior thermal stability began to be observed when Mn \geq 50% for partially delithiated binary olivines, but for the fully delithiated phase, the effect was observed for higher contents of Mn (Mn \geq 75%).

Upon further heating higher than 550°C, $(\text{Fe}_{0.25}\text{Mn}_{0.75})_2\text{P}_2\text{O}_7$, the solid solution between $\text{Mn}_2\text{P}_2\text{O}_7$ and $\text{Fe}_2\text{P}_2\text{O}_7$, was formed, shown in Figure 3.3.13(d). The observed XRD pattern of $(\text{Fe}_{0.25}\text{Mn}_{0.75})_2\text{P}_2\text{O}_7$ corresponded with the XRD pattern of $(\text{Fe}_{0.25}\text{Mn}_{0.75})_2\text{P}_2\text{O}_7$ calculated from the DFT calculation. From the data above, the decomposition mechanism of $\text{Fe}_{0.25}\text{Mn}_{0.75}\text{PO}_4$ at elevated temperatures is proposed as the following reactions:

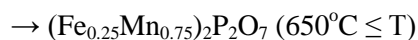
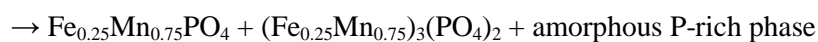
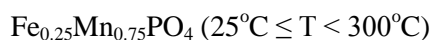


Figure 3.3.14(a) shows the thermal behavior of the partially delithiated $\text{Li}_{0.46}\text{Fe}_{0.25}\text{Mn}_{0.75}\text{PO}_4$ phase at temperatures ranging from 25°C to 700°C. The two-phase existence of $\text{LiFe}_{0.25}\text{Mn}_{0.75}\text{PO}_4$ and $\text{Fe}_{0.25}\text{Mn}_{0.75}\text{PO}_4$ was confirmed, which is different from the behavior of $\text{Li}_{1-y}\text{Fe}_{0.75}\text{Mn}_{0.25}\text{PO}_4$, but similar to that of $\text{Li}_{1-y}\text{Fe}_{0.5}\text{Mn}_{0.5}\text{PO}_4$. As in the case of $\text{Li}_{0.4}\text{Fe}_{0.5}\text{Mn}_{0.5}\text{PO}_4$, the two-phase mixture was converted to a single phase of $\text{Li}_{0.46}\text{Fe}_{0.25}\text{Mn}_{0.75}\text{PO}_4$ with a slight increase in temperature shown in Figure 3.3.14(b). However, the transition temperature increased from 250°C to 300°C. This indicates that the higher Mn content binary olivine prefers a two-phase separation more strongly. The fundamental reasons for the different phase behaviors of Mn- or Fe-rich olivine structures was discussed.[34] Once, the solid solution phase of $\text{Li}_{0.46}\text{Fe}_{0.25}\text{Mn}_{0.75}\text{PO}_4$ was formed, its decomposition path (Figure 3.3.14(c)) became analogous to that of $\text{Li}_{0.44}\text{Fe}_{0.75}\text{Mn}_{0.25}\text{PO}_4$ and $\text{LiFe}_{0.5}\text{Mn}_{0.5}\text{PO}_4$, where the mixture of the fully lithiated olivine phase and $\text{M}_2\text{P}_2\text{O}_7$ (M = Fe, Mn) appeared at 550°C. Additionally, the XRD peak location of the olivine phase in $\text{Li}_{0.44}\text{Fe}_{0.25}\text{Mn}_{0.75}\text{PO}_4$ at 600°C was identical to that of $\text{LiFe}_{0.25}\text{Mn}_{0.75}\text{PO}_4$ at 600°C. From the data on $\text{Li}_{0.46}\text{Fe}_{0.25}\text{Mn}_{0.75}\text{PO}_4$ mentioned above, we propose that the reaction mechanism of $\text{Li}_{0.46}\text{Fe}_{0.25}\text{Mn}_{0.75}\text{PO}_4$ is as follows:

$\text{Li}_{0.46}\text{Fe}_{0.25}\text{Mn}_{0.75}\text{PO}_4$ (solid solution + two-phase reaction, $25^\circ\text{C} \leq T < 300^\circ\text{C}$)

$\rightarrow \text{Li}_{0.46}\text{Fe}_{0.25}\text{Mn}_{0.75}\text{PO}_4$ (solid solution, $300^\circ\text{C} \leq T < 550^\circ\text{C}$)

$\rightarrow \text{LiFe}_{0.25}\text{Mn}_{0.75}\text{PO}_4 + (\text{Fe}_{0.25}\text{Mn}_{0.75})_2\text{P}_2\text{O}_7$ ($550^\circ\text{C} \leq T$)

3.3.4.2.4 Phase stability map of Fe–Mn binary olivine as a function of temperature and Li amount in the structure

From the extensive series of XRD results above, it was found that the $\text{Li}_{1-y}\text{Fe}_{1-x}\text{Mn}_x\text{PO}_4$ [$0 \leq x, y \leq 1$] displayed different thermal characteristics depending on the Fe/Mn and Li contents in the olivine structures. A summary of the stable phases for $\text{Li}_{1-y}\text{Fe}_{1-x}\text{Mn}_x\text{PO}_4$ [$0 \leq x \leq 1$] upon heating are shown in Figures 3.3.15 and 3.3.16 with respect to the Li and Fe/Mn contents. While the fully lithiated $\text{LiFe}_{1-x}\text{Mn}_x\text{PO}_4$ [$0 \leq x \leq 1$] phases were highly stable at high temperature, it was observed that delithiated phases were susceptible to partial phase transformation upon heating. In the phase stability map of fully delithiated phases $\text{Fe}_{1-x}\text{Mn}_x\text{PO}_4$ [$0 \leq x \leq 1$] (Figure 3.3.15), we observed that the thermal decomposition temperature of the fully delithiated phases generally declined by an increase in the Mn content in the olivine structure. A significant drop in the decomposition temperature was observed when the Mn content exceeded the Fe content in the olivine. In the phase stability map of partially delithiated phases $\text{Li}_{1-y}\text{Fe}_{1-x}\text{Mn}_x\text{PO}_4$ [$0 \leq x \leq$

1, $y \approx 0.6$] (Figure 3.3.16), the two-phase characteristic of $(1-y)\text{LiMPO}_4 + y\text{MPO}_4$ was lifted upon a slight increase in the temperature. In the case of Fe-rich binary olivines, a solid solution behavior was observed even at room temperature, while a higher Mn content in binary olivines exhibited a stronger two-phase preference. Contrary to the sensitivity of solid solution formation depending on the Fe/Mn content, the decomposition temperature into $\text{M}_2\text{P}_2\text{O}_7$ was similar among samples. Notable is that Fe-rich binary olivines exhibited a wider temperature window for the solid solution phase before decomposing into $\text{M}_2\text{P}_2\text{O}_7$.

3.3.5 Conclusion

In summary, the phase stability of $\text{Li}_{1-y}\text{Fe}_{1-x}\text{Mn}_x\text{PO}_4$ ($0 \leq x, y \leq 1$) during delithiation and lithiation was investigated as a function of the temperature, the Li composition, and the Fe or Mn amounts in the structure with temperature-controlled *in situ* XRD. Fully lithiated $\text{Li Fe}_{1-x}\text{Mn}_x\text{PO}_4$ ($0 \leq x \leq 1$) remained stable up to high temperatures ($>700^\circ\text{C}$). However, the thermal stability of delithiated $\text{Li}_{1-y}\text{Fe}_{1-x}\text{Mn}_x\text{PO}_4$ ($0 \leq x, y \leq 1$) was influenced sensitively by the Fe/Mn content in the structure. Furthermore, the delithiation mechanism (one-phase vs. two-phase reaction) was dependent on the Fe/Mn ratio. It was generally observed that higher Mn content binary olivine

materials exhibited inferior thermal stabilities in the charged states and a stronger preference for the two-phase behavior.

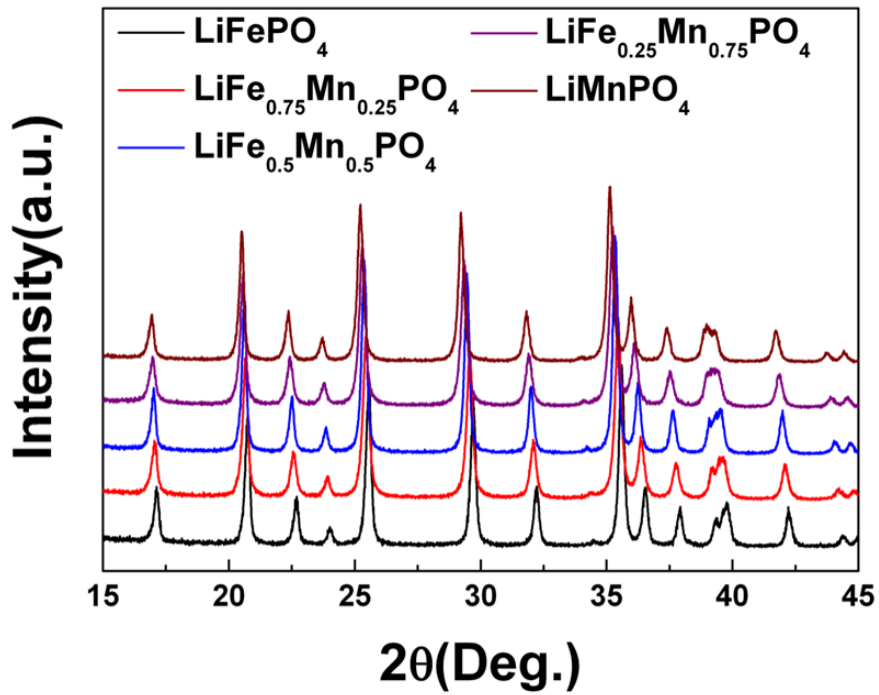


Figure 3.3.1 XRD patterns of as-prepared $\text{LiFe}_{1-x}\text{Mn}_x\text{PO}_4$ [$0 \leq x \leq 1$]

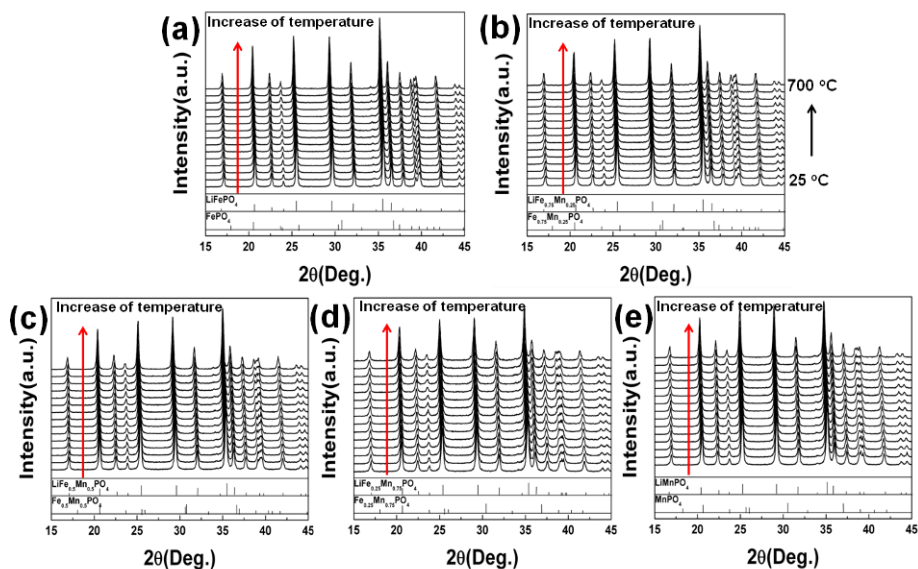


Figure 3.3.2 (a) *in-situ* XRD patterns of fully lithiated LiFePO_4 at temperature from 25°C to 700°C and at 2θ from 15° to 45° , (b) *in-situ* XRD patterns of fully lithiated $\text{LiFe}_{0.75}\text{Mn}_{0.25}\text{PO}_4$ at temperature from 25°C to 700°C and at 2θ from 15° to 45° , (c) *in-situ* XRD patterns of fully lithiated $\text{LiFe}_{0.5}\text{Mn}_{0.5}\text{PO}_4$ at temperature from 25°C to 700°C and at 2θ from 15° to 45° , (d) *in-situ* XRD patterns of fully lithiated $\text{LiFe}_{0.25}\text{Mn}_{0.75}\text{PO}_4$ at temperature from 25°C to 700°C and at 2θ from 15° to 45° , and (e) *in-situ* XRD patterns of fully lithiated LiMnPO_4 at temperature from 25°C to 700°C and at 2θ from 15° to 45° .

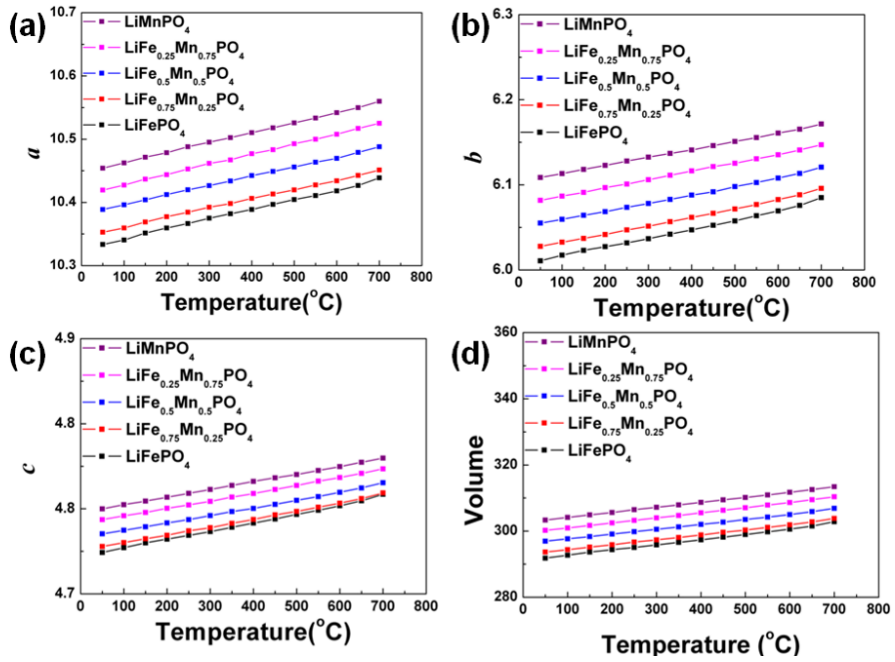


Figure 3.3.3 (a) Lattice parameter a , (b) Lattice parameter b , (c) Lattice parameter c , and (d) volume of $\text{LiFe}_{1-x}\text{Mn}_x\text{PO}_4$ [$0 \leq x \leq 1$] varied by temperature

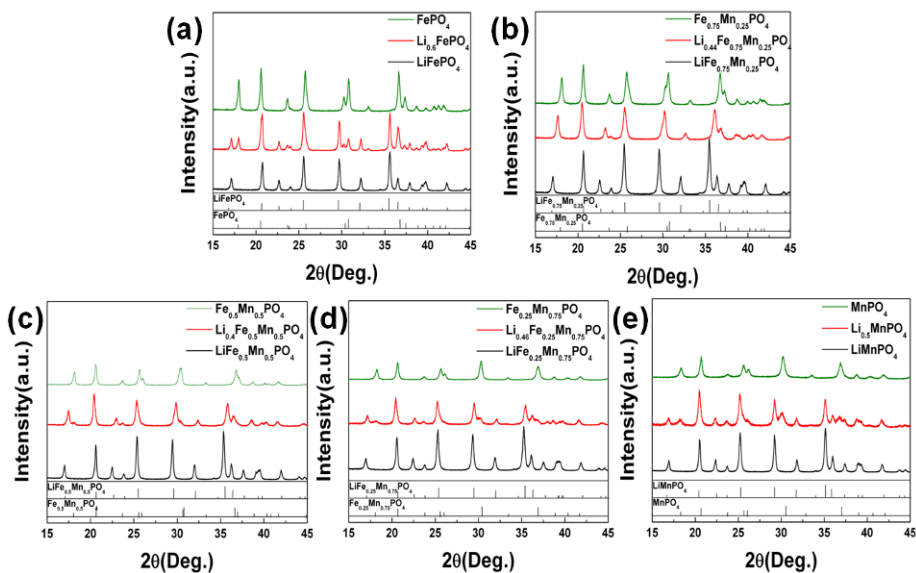


Figure 4 K. Kang *et al.*

Figure 3.3.4 (a) Evolution of XRD patterns of $\text{Li}_{1-y}\text{FePO}_4$ [$0 \leq y \leq 1$] with a delithiation process, (b) Evolution of XRD patterns of $\text{Li}_{1-y}\text{Fe}_{0.75}\text{Mn}_{0.25}\text{PO}_4$ [$0 \leq y \leq 1$] with a delithiation process, (c) Evolution of XRD patterns of $\text{Li}_{1-y}\text{Fe}_{0.5}\text{Mn}_{0.5}\text{PO}_4$ [$0 \leq y \leq 1$] with a delithiation process, (d) Evolution of XRD patterns of $\text{Li}_{1-y}\text{Fe}_{0.25}\text{Mn}_{0.75}\text{PO}_4$ [$0 \leq y \leq 1$] with a delithiation process, and (e) Evolution of XRD patterns of $\text{Li}_{1-y}\text{MnPO}_4$ [$0 \leq y \leq 1$] with a delithiation process

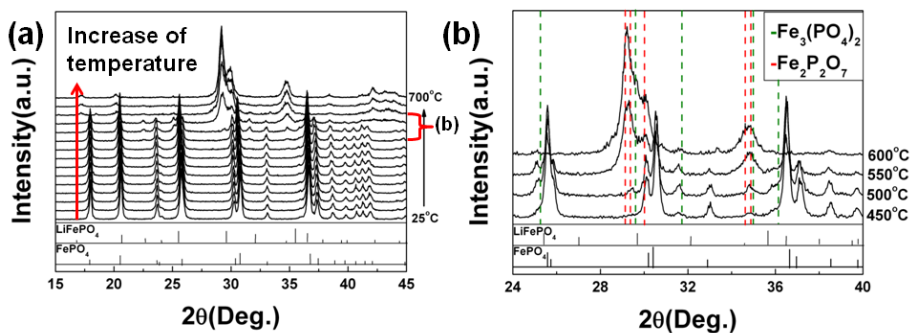


Figure 3.3.5 (a) *in-situ* XRD patterns of fully delithiated FePO₄ at temperature from 25°C to 700°C and at 2θ from 15° to 45° and (b) *in-situ* XRD patterns of fully delithiated FePO₄ at temperature from 450°C to 600°C and at 2θ from 24° to 40°

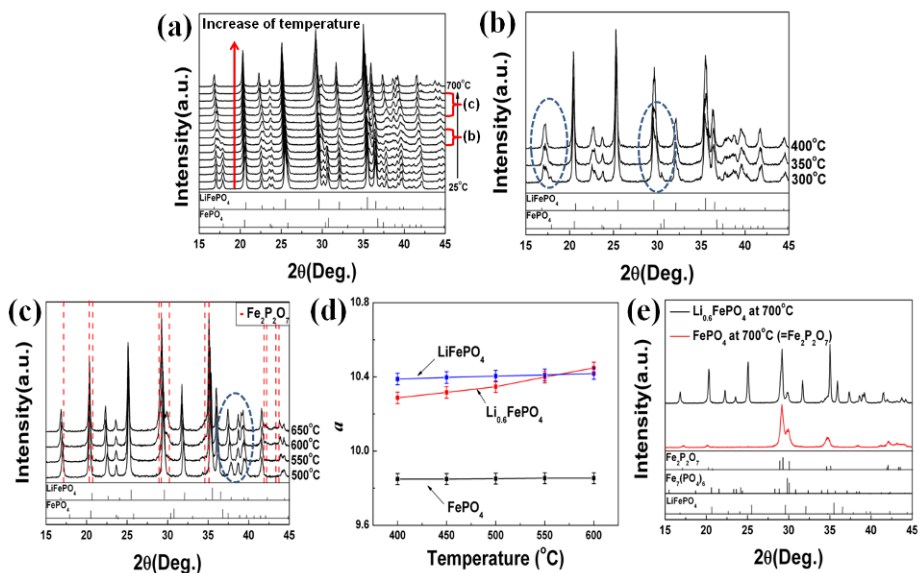


Figure 3.3.6 (a) *in-situ* XRD patterns of partially delithiated $\text{Li}_{0.6}\text{FePO}_4$ at temperature from 25°C to 700°C (2θ from 15° to 45°), (b) *in-situ* XRD patterns of partially delithiated $\text{Li}_{0.6}\text{FePO}_4$ at temperature from 300°C to 400°C (2θ from 15° to 45°), (c) *in-situ* XRD patterns of partially delithiated $\text{Li}_{0.6}\text{FePO}_4$ at temperature from 500°C to 650°C and at 2θ from 15° to 45°, (d) Comparison of lattice parameter a of $\text{Li}_{1-y}\text{FePO}_4$ [$y = 0, 0.4, \text{ and } 1$] varied by temperature and (e) XRD patterns of partially delithiated $\text{Li}_{0.6}\text{FePO}_4$ at 700°C compared with $\text{Fe}_2\text{P}_2\text{O}_7$ and $\text{Fe}_7(\text{PO}_4)_6$ among at 2θ from 15° to 45°

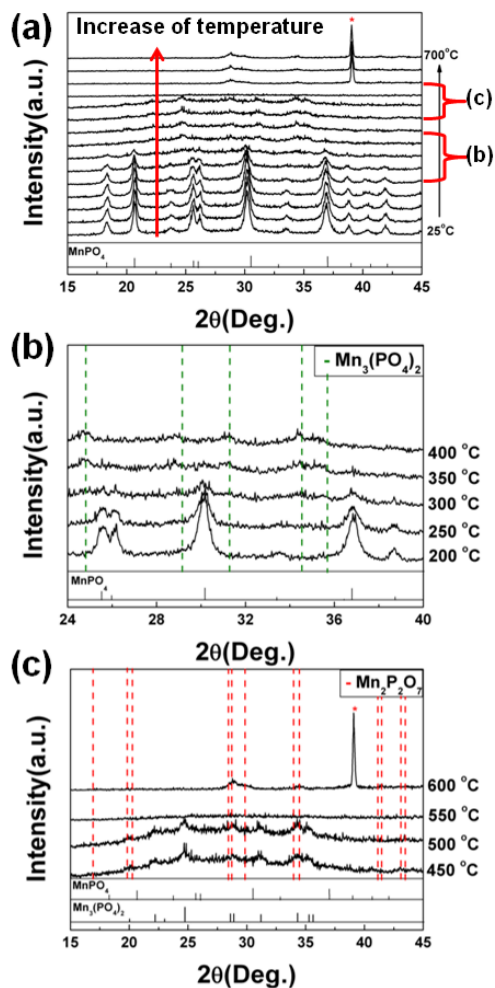


Figure 3.3.7 (a) *in-situ* XRD patterns of fully delithiated MnPO_4 at temperature from 25°C to 700°C and at 2θ from 15° to 45° , (b) *in-situ* XRD patterns of fully delithiated MnPO_4 at temperature from 200°C to 400°C and at 2θ from 24° to 40° , and (c) *in-situ* XRD patterns of fully delithiated MnPO_4 at temperature from 450°C to 600°C and at 2θ from 15° to 45° . [* : the XRD peak of Pt holder]

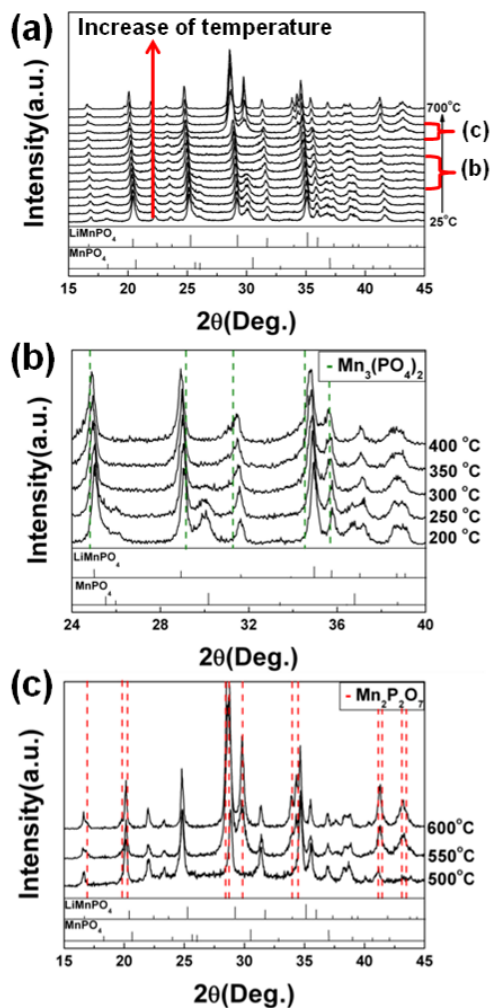


Figure 3.3.8 (a) *in-situ* XRD patterns of partially delithiated $\text{Li}_{0.5}\text{MnPO}_4$ at temperature from 25°C to 700°C and at 2θ from 15° to 45°, (b) *in-situ* XRD patterns of partially delithiated $\text{Li}_{0.5}\text{MnPO}_4$ at temperature from 200°C to 400°C, and at 2θ from 24° to 40°, and (c) *in-situ* XRD patterns of partially delithiated $\text{Li}_{0.5}\text{MnPO}_4$ at temperature from 500°C to 600°C and at 2θ from 15° to 45°

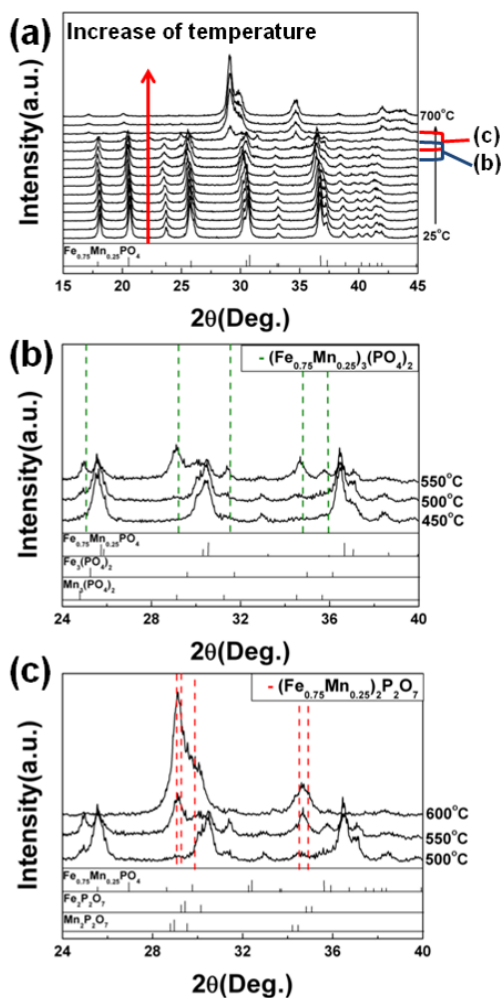


Figure 3.3.9 (a) *in-situ* XRD patterns of fully delithiated $\text{Fe}_{0.75}\text{Mn}_{0.25}\text{PO}_4$ at temperature from 25°C to 700°C and at 2θ from 15° to 45°, (b) *in-situ* XRD patterns of fully delithiated fully delithiated $\text{Fe}_{0.75}\text{Mn}_{0.25}\text{PO}_4$ at temperature from 450°C to 550°C and at 2θ from 24° to 40°, and (c) *in-situ* XRD patterns of fully delithiated fully delithiated $\text{Fe}_{0.75}\text{Mn}_{0.25}\text{PO}_4$ at temperature from 500 °C to 600 °C and at 2θ from 24° to 40°

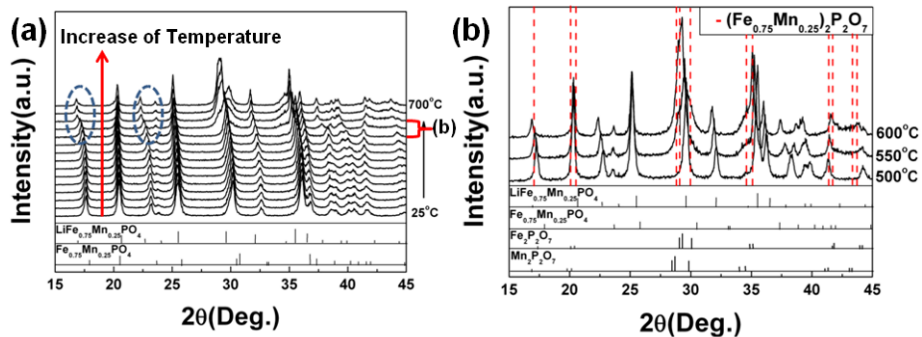


Figure 3.3.10 (a) *in-situ* XRD patterns of partially delithiated $\text{Li}_{0.44}\text{Fe}_{0.75}\text{Mn}_{0.25}\text{PO}_4$ at temperature from 25°C to 700°C and at 2θ from 15° to 45° and (b) *in-situ* XRD patterns of partially delithiated $\text{Li}_{0.44}\text{Fe}_{0.75}\text{Mn}_{0.25}\text{PO}_4$ at temperature from 500°C to 600°C at 2θ from 15° to 45°

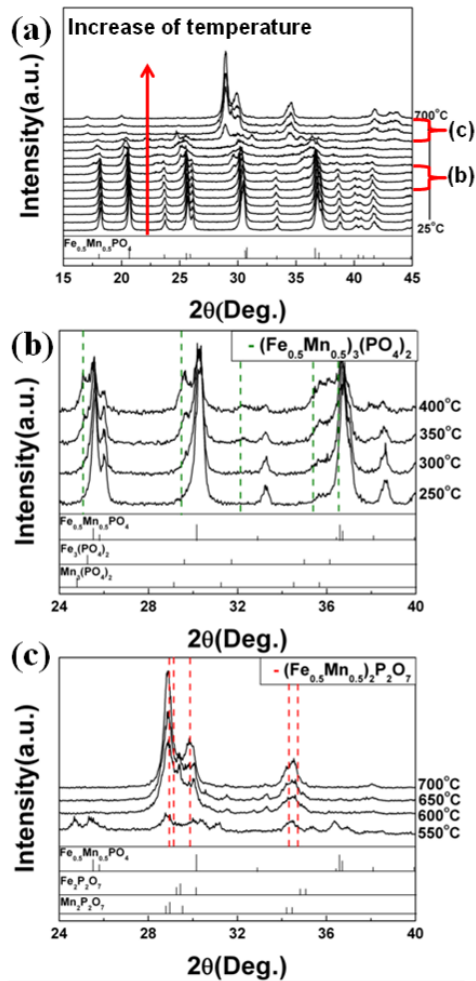


Figure 3.3.11 (a) *in-situ* XRD patterns of fully delithiated $\text{Fe}_{0.5}\text{Mn}_{0.5}\text{PO}_4$ at temperature from 25°C to 700°C and at 2θ from 15° to 45°, (b) *in-situ* XRD patterns of fully delithiated fully delithiated $\text{Fe}_{0.5}\text{Mn}_{0.5}\text{PO}_4$ at temperature from 250°C to 400°C and at 2θ from 24° to 40°, and (c) *in-situ* XRD patterns of fully delithiated fully delithiated $\text{Fe}_{0.5}\text{Mn}_{0.5}\text{PO}_4$ at temperature from 550°C to 700°C and at 2θ from 24° to 40°

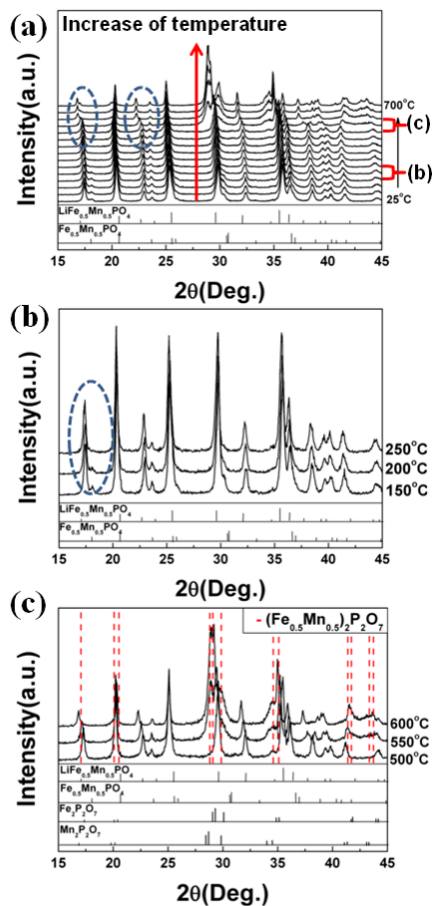


Figure 3.3.12 (a) *in-situ* XRD patterns of partially delithiated $\text{Li}_{0.4}\text{Fe}_{0.5}\text{Mn}_{0.5}\text{PO}_4$ at temperature from 25°C to 700°C and at 2θ from 15° to 45°, (b) *in-situ* XRD patterns of partially delithiated fully delithiated $\text{Li}_{0.4}\text{Fe}_{0.5}\text{Mn}_{0.5}\text{PO}_4$ at temperature from 150°C to 250°C and at 2θ from 15° to 45°, and (c) *in-situ* XRD patterns of partially delithiated fully delithiated $\text{Li}_{0.4}\text{Fe}_{0.5}\text{Mn}_{0.5}\text{PO}_4$ at temperature from 500°C to 600°C and at 2θ from 15° to 45°

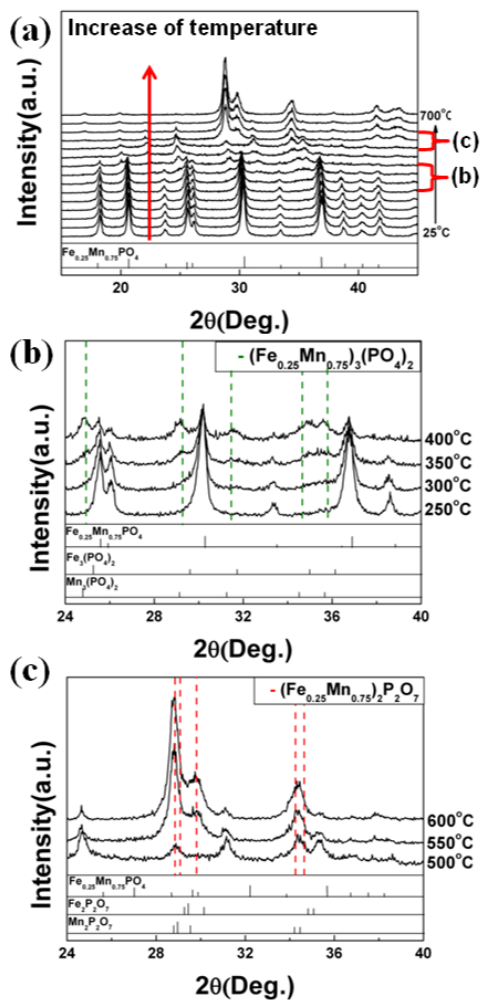


Figure 3.3.13 (a) *in-situ* XRD patterns of fully delithiated $\text{Fe}_{0.25}\text{Mn}_{0.75}\text{PO}_4$ at temperature from 25°C to 700°C and at 2θ from 15° to 45°, (b) *in-situ* XRD patterns of fully delithiated fully delithiated $\text{Fe}_{0.25}\text{Mn}_{0.75}\text{PO}_4$ at temperature from 250°C to 400°C and at 2θ from 24° to 40°, and (c) *in-situ* XRD patterns of fully delithiated fully delithiated $\text{Fe}_{0.25}\text{Mn}_{0.75}\text{PO}_4$ at temperature from 500°C to 600°C and at 2θ from 24° to 40°

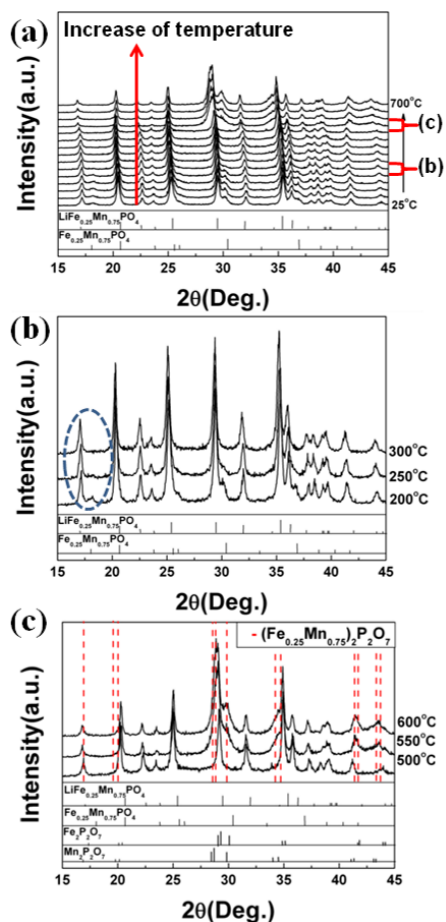


Figure 3.3.14 (a) *in-situ* XRD patterns of partially delithiated $\text{Li}_{0.46}\text{Fe}_{0.25}\text{Mn}_{0.75}\text{PO}_4$ at temperature from 25°C to 700°C and at 2θ from 15° to 45° , (b) *in-situ* XRD patterns of partially delithiated fully delithiated $\text{Li}_{0.46}\text{Fe}_{0.25}\text{Mn}_{0.75}\text{PO}_4$ at temperature from 200°C to 300°C and at 2θ from 15° to 45° , and (c) *in-situ* XRD patterns of partially delithiated fully delithiated $\text{Li}_{0.46}\text{Fe}_{0.25}\text{Mn}_{0.75}\text{PO}_4$ at temperature from 500°C to 600°C and at 2θ from 15° to 45°

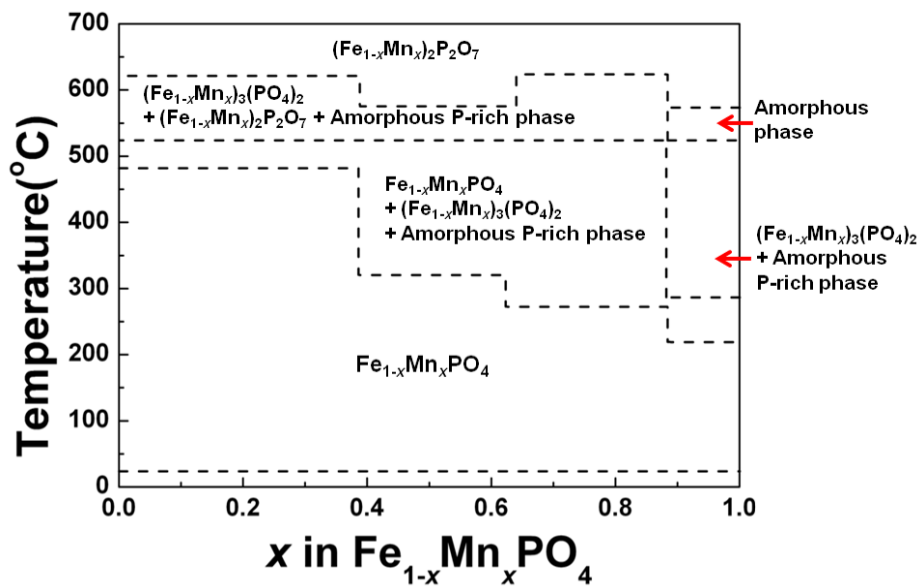


Figure 3.3.15 The phase stability map of fully delithiated $\text{Fe}_{1-x}\text{Mn}_x\text{PO}_4$ [$0 \leq x \leq 1$] as functions of temperature

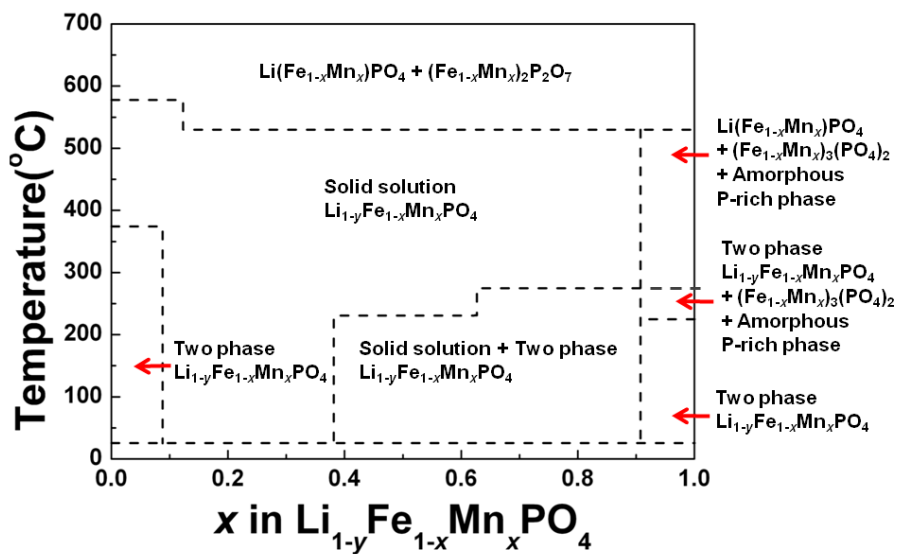


Figure 3.3.16 The phase stability map of partially delithiated $\text{Li}_{1-y}\text{Fe}_{1-x}\text{Mn}_x\text{PO}_4$ [$0 \leq x \leq 1$, $y \approx 0.6$] as functions of temperature

	Atom	As-prepared phase	Partially delithiated phase	Fully delithiated phase
$\text{Li}_{1-y}\text{FePO}_4$	Li	1	0.6	0
	Fe	1	1	1
$\text{Li}_{1-y}\text{Fe}_{0.75}\text{Mn}_{0.25}\text{PO}_4$	Li	1	0.44	0
	Fe	0.75	0.75	0.75
	Mn	0.25	0.25	0.25
$\text{Li}_{1-y}\text{Fe}_{0.5}\text{Mn}_{0.5}\text{PO}_4$	Li	1	0.4	0
	Fe	0.5	0.5	0.5
	Mn	0.5	0.5	0.5
$\text{Li}_{1-y}\text{Fe}_{0.25}\text{Mn}_{0.75}\text{PO}_4$	Li	1	0.46	0
	Fe	0.25	0.25	0.25
	Mn	0.75	0.75	0.75
$\text{Li}_{1-y}\text{MnPO}_4$	Li	1	0.5	0
	Mn	1	1	1

Table 3.3.1 Atomic ratio of metal ions (Li, Fe, and Mn) in $\text{Li}_{1-y}\text{Fe}_{1-x}\text{Mn}_x\text{PO}_4$ [$0 \leq x, y \leq 1$]

	a (Å)	b (Å)	c (Å)
LiFePO₄	10.328	6.009	4.697
LiFe_{0.75}Mn_{0.25}PO₄	10.348	6.026	4.704
LiFe_{0.5}Mn_{0.5}PO₄	10.384	6.053	4.718
LiFe_{0.25}Mn_{0.75}PO₄	10.415	6.079	4.735
LiMnPO₄	10.450	6.106	4.748

Table 3.3.2 Lattice parameters of LiFe_{1-x}Mn_xPO₄ [$0 \leq x \leq 1$]

	Lattice	Thermal coefficient (K ⁻¹)
LiFePO ₄	<i>a</i>	1.57 × 10 ⁻⁴
	<i>b</i>	1.08 × 10 ⁻⁴
	<i>c</i>	1.01 × 10 ⁻⁴
	Volume	1.61 × 10 ⁻²
LiFe _{0.75} Mn _{0.25} PO ₄	<i>a</i>	1.49 × 10 ⁻⁴
	<i>b</i>	1.02 × 10 ⁻⁴
	<i>c</i>	9.49 × 10 ⁻⁵
	Volume	1.53 × 10 ⁻²
LiFe _{0.5} Mn _{0.5} PO ₄	<i>a</i>	1.50 × 10 ⁻⁴
	<i>b</i>	9.88 × 10 ⁻⁵
	<i>c</i>	9.09 × 10 ⁻⁵
	Volume	1.50 × 10 ⁻²
LiFe _{0.25} Mn _{0.75} PO ₄	<i>a</i>	1.61 × 10 ⁻⁴
	<i>b</i>	9.90 × 10 ⁻⁵
	<i>c</i>	9.07 × 10 ⁻⁵
	Volume	1.55 × 10 ⁻²
LiMnPO ₄	<i>a</i>	1.59 × 10 ⁻⁴
	<i>b</i>	9.49 × 10 ⁻⁴
	<i>c</i>	9.09 × 10 ⁻⁵
	Volume	1.53 × 10 ⁻²

Table 3.3.3 The thermal coefficients of LiFe_{1-x}Mn_xPO₄ [0 ≤ x ≤ 1]

3.3.6 References

- [1] A. K. Padhi, K. S. Nanjundaswamy, J. B. Goodenough, *J. Electrochem. Soc.*, **144**, 1188 (1997).
- [2] A. Yamada, Y. Takei, H. Koizumi, N. Sonoyama, R. Kanno, K. Itoh, M. Yonemura, T. Kamiyama, *Chem. Mater.*, **18**, 804 (2006).
- [3] S. Y. Chung, J. T. Bloking, Y. M. Chiang, *Nat. Mater.*, **1**, 123 (2002).
- [4] J. Kim, Y. U. Park, D. H. Seo, J. Kim, S. W. Kim, K. Kang, *J. Electrochem. Soc.*, **158**, A250 (2011).
- [5] H. Gwon, D. H. Seo, S. W. Kim, J. Kim, K. Kang, *Adv. Funct. Mater.*, **19**, 3285 (2009).
- [6] J. Kim, D. H. Seo, S. W. Kim, Y. U. Park, K. Kang, *Chem. Commun.*, **46**, 1305 (2010).
- [7] Y.-U. Park, J. Kim, H. Gwon, D. H. Seo, S. W. Kim, K. Kang, *Chem. Mater.*, **22**, 2573 (2010).
- [8] A. Yamada, Y. Kudo, K. Y. Liu, *J. Electrochem. Soc.*, **148**, A747 (2001).
- [9] K. Saravanan, J. J. Vittal, M. V. Reddy, B. V. R. Chowdari, P. Balaya, *J. Solid State Electrochem.*, **14**, 1755 (2010).
- [10] S. M. Oh, H. G. Jung, C. S. Yoon, S. T. Myung, Z. H. Chen, K. Amine, Y. K. Sun, *J. Power Sources*, **196**, 6924 (2011).
- [11] B. Zhang, X. J. Wang, H. Li, X. J. Huang, *J. Power Sources*, **196**, 6992

(2011).

[12] M. Yonemura, A. Yamada, Y. Takei, N. Sonoyama, R. Kanno, *J. Electrochem. Soc.*, **151**, A1352 (2004).

[13] P. S. Herle, B. Ellis, N. Coombs, L. F. Nazar, *Nat. Mater.*, **3**, 147 (2004).

[14] Y. G. Wang, Y. R. Wang, E. J. Hosono, K. X. Wang, H. S. Zhou, *Angew. Chem.*, **47**, 7461 (2008).

[15] P. Gibot, M. Casas-Cabanas, L. Laffont, S. Levasseur, P. Carlach, S. Hamelet, J. M. Tarascon, C. Masquelier, *Nat. Mater.*, **7**, 741 (2008).

[16] C. Delacourt, L. Laffont, R. Bouchet, C. Wurm, J. B. Leriche, M. Morcrette, J. M. Tarascon, C. Masquelier, *J. Electrochem. Soc.*, **152**, A913 (2005).

[17] A. Yamada, Y. Kudo, K. Y. Liu, *J. Electrochem. Soc.*, **148**, A1153 (2001).

[18] G. Kobayashi, A. Yamada, S. Nishimura, R. Kanno, Y. Kobayashi, S. Seki, Y. Ohno, H. Miyashiro, *J. Power Sources*, **189**, 397 (2009).

[19] H. L. Wang, Y. Yang, Y. Y. Liang, L. F. Cui, H. S. Casalongue, Y. G. Li, G. S. Hong, Y. Cui, H. J. Dai, *Angew. Chem.*, **50**, 7364 (2011).

[20] C. Delacourt, P. Poizot, J.-M. Tarascon, C. Masquelier, *Nat. Mater.*, **4**, 254 (2005).

[21] S.-W. Kim, J. Kim, H. Gwon, K. Kang, *J. Electrochem. Soc.*, **156**, A635 (2009).

- [22] G. Y. Chen, T. J. Richardson, *J. Power Sources*, **195**, 1221 (2010).
- [23] S. P. Ong, A. Jain, G. Hautier, B. Kang, G. Ceder, *Electrochem. Commun.*, **12**, 427 (2010).
- [24] J. K. Warner, A. K. Cheetham, A. G. Nord, R. B. Vondreele, M. Yethiraj, *J. Mater. Chem.*, **2**, 191 (1992).
- [25] J. P. Perdew, K. Burke, M. Ernzerhof, *Phy. Rev. Lett.*, **77**, 3865 (1996).
- [26] G. Kresse, J. Furthmuller, *Com. Mater. Science*, **6**, 15 (1996).
- [27] K. Kang, Y. S. Meng, J. Breger, C. P. Grey, G. Ceder, *Science*, **311**, 977 (2006).
- [28] K. Kang, D. Morgan, G. Ceder, *Phy. Rev. B*, **79**, 014305 (2009).
- [29] D. H. Seo, H. Gwon, S. W. Kim, J. Kim, K. Kang, *Chem. Materi.*, **22**, 518 (2010).
- [30] F. Zhou, K. S. Kang, T. Maxisch, G. Ceder, D. Morgan, *Solid State Commun.*, **132**, 181 (2004).
- [31] R. D. Shannon, C. T. Prewitt, *Acta Cryst. B*, **B 25**, 925 (1969).
- [32] S. W. Martin, *J. Am. Cer. Soc.*, **74**, 1767 (1991).
- [33] J. Kim, K.-Y. Park, I.-C. Park, J.-K. Yoo, D.-H. Seo, S.-W. Kim, K. Kang, *J. Electrochem. Soc.*, **159**, A55-A59 (2012).
- [34] K.-Y. Park, J. Hong, J. Kim, Y.-U. Park, H. Kim, D.-H. Seo, S.-W. Kim, J.-W. Choi and K. Kang *J. Electrochem. Soc.*, **160**, A444-A448 (2013)

Chapter 4. NASICON Electrode

4.1. $\text{Li}_3\text{V}_2(\text{PO}_4)_3$ /Conducting Polymer as a High Power 4V-class Lithium battery electrode

4.1.1 . Research Background

Lithium ion batteries have been considered as potential energy storage materials due to their ability to store and release electric energy with high density and reversibility.[1-3] At present, lithium ion batteries are required to possess high safety and power/energy density for large-scale energy storage system such as electric vehicles.[1, 4, 5] NASICON framework monoclinic $\text{Li}_3\text{V}_2(\text{PO}_4)_3$ has much attraction as a prospective candidate for use as the potential cathode material in lithium ion batteries due to the high thermal stability induced by strong P-O bonds and three-dimensional solid framework in polyanion $(\text{PO}_4)^{3-}$, higher redox potential (average potential of *ca.* 3.85V vs. Li^+) than LiFePO_4 , and its two independent lithium sites with a high theoretical capacities of 133 mAh g^{-1} (when charged up to 4.4V).[6-9] However, the low electrical conductivity of monoclinic $\text{Li}_3\text{V}_2(\text{PO}_4)_3$ (2.4×10^{-7} S cm^{-1} at 25°C) was a major drawback for its high current-rate performance.^{6,8} In the past few years, carbon-coating were usually used for improvement of the low conductivity. To avoid the irregular carbon-coating that can lead to poor connectivity among particles and low improvement of

conductivity below expectations, it has been generally used that the surface of each particle is uniformly coated by carbonization using organic compounds.[7, 10, 11] However, this carbon-coating is formed at high temperature in an inert or reducing atmosphere and accompanies the formation of non environmental-friendly products such as volatile organic compounds, CO, and CO₂. [7, 12]

Conductive polymers are attractive materials in covering crystallite surfaces in terms of improving not only mechanical flexibility but also electrical conductivity to improve Li ions diffusion.[13, 14] Also, they can be coated under mild processing conditions such as low temperature synthesis to prevent formations of harmful gases, compared to the carbon coating using organic compound.[15] Recently, improvement on cyclability and rate capability was reported when some battery materials were supported by conducting polymers.[13-15]

As inspired this, we fabricate the Li₃V₂(PO₄)₃ composite with the conducting polymer, poly(3,4-ethylenedioxythiophene) (=PEDOT) for highly improved electrochemical performances. PEDOT is uniformly deposited on the surface of Li₃V₂(PO₄)₃ and this Li₃V₂(PO₄)₃/PEDOT composite has significantly improved rate capability and cyclability without any conductive carbon, compared to pristine Li₃V₂(PO₄)₃ mixed with

conductive carbon.

3.1.2 Experimental Section

3.1.2.1. Synthesis of $\text{Li}_3\text{V}_2(\text{PO}_4)_3$

$\text{Li}_3\text{V}_2(\text{PO}_4)_3$ powder was synthesized using the conventional solid-state synthesis. LiNO_3 (Sigma Aldrich, 98%), V_2O_5 (Sigma Aldrich, 98%), and $\text{NH}_4\text{H}_2\text{PO}_4$ (Fluka, 98%) with molar ratios of 3 : 1 : 3 were used as precursors. They were dispersed into acetone, thoroughly mixed, and ground by wet ball-milling. After evaporating the acetone, the precursors were then fired at 350°C under Ar and 5% H_2 conditions for 5 hours. The mixture was then re-ground and manually pelletized using a disk-shaped mold. After pre-heating, we calcined the pellets at 750°C under Ar and 5% H_2 conditions for 5 hours.

3.1.2.2. Materials characterization

Powder XRD of all materials was carried out on a Bruker D8-Advantage powder diffractometer using Cu $K\alpha$ radiation ($= 1.54178 \text{ \AA}$) from $2\theta = 10$ to 60° at 1s per step of 0.01° . The *ex-situ* XRD of fully lithiated alluaudite- LiFePO_4 was determined by XRD (Bruker D8 ADVANCE) with Cu $K\alpha$ radiation ($= 1.54178 \text{ \AA}$). Data were recorded over a 2θ range of 10° to 60° , with a step size of 0.01° . Structural refinements were done by the Rietveld method with Fullprof software. The morphology and particle size parameters were observed by field emission transmission electron microscopy (FETEM,

PHILIPS Tecnai F20) operating at 200 kV. Samples were further characterized using a Fourier transform infrared (FT-IR) microscope (JASCO) by KBr pellet analysis. Atomic ratios of elements such as Li, V, and P were determined by inductively coupled plasma atomic emission spectroscopy (ICP-AES, Thermo Jarrel Ash, Polyscan 60E, USA).

3.1.2.3. Electrochemistry

The slurry of 95wt% $\text{Li}_3\text{V}_2(\text{PO}_4)_3$ /PEDOT composite (82wt% $\text{Li}_3\text{V}_2(\text{PO}_4)_3$ and 13wt% PEDOT) and 5wt% polyvinylidene fluoride (PVDF) dispersed in N-methyl-2-pyrrolidone (NMP) was prepared and cast on aluminum foil. NMP was evaporated at 70°C for 2 hours. Electrochemical cells were assembled in a CR2016 type coin cell with a Li counter electrode, separator (Celgard 2400), and 1 M LiPF_6 electrolyte in a mixture of 1:1 ethyl carbonate/dimethyl carbonate in an Ar-filled glove box. Electrochemical cells were assembled under an atmosphere of highly pure argon in a glove box. The charge/discharge test was performed using a galvanostat (WonA Tech).

4.1.3 Results and Discussion

4.1.3.1. Fabrication process of $\text{Li}_3\text{V}_2(\text{PO}_4)_3$ /PEDOT composite

The Fabrication process of $\text{Li}_3\text{V}_2(\text{PO}_4)_3$ /PEDOT composite is shown in Figure 4.1.1. The first step is delithiation of $\text{Li}_3\text{V}_2(\text{PO}_4)_3$ for polymerization

of monomer 3,4-ethylenedioxythiophene (EDOT). The oxidized transition metal ions in the delithiated phase are the driving force for polymerization of the monomers.[11, 15] Therefore, outer surface on each particle is uniformly coated with polymer. For Li deintercalation from the structure, the synthesized $\text{Li}_3\text{V}_2(\text{PO}_4)_3$ was chemically delithiated by NO_2BF_4 , which is a strong oxidizing agent with a high redox potential of *ca.* 5.1V vs. Li^+/Li .[16] The composition of $\text{Li}_{3-x}\text{V}_2(\text{PO}_4)_3$ was controlled by 24hours of the reaction time and a molar ratio of 3 : 0.5 between the $\text{Li}_3\text{V}_2(\text{PO}_4)_3$ and NO_2BF_4 with acetonitrile in an Ar-filled glove box. And then, monomer EDOTs are polymerized on the surface with reduction from V^{4+} and V^{3+} and Li^+ reinsertion. The polymerization of EDOT by the Li reinsertion operates without any other source of oxidant or initiator. Finally, $\text{Li}_3\text{V}_2(\text{PO}_4)_3/\text{PEDOT}$ composite is fabricated. The fabrication mechanism of $\text{Li}_3\text{V}_2(\text{PO}_4)_3/\text{PEDOT}$ composite is summarized at Equation (1).



4.1.3.2. Structural information of $\text{Li}_3\text{V}_2(\text{PO}_4)_3/\text{PEDOT}$ composite

Figure 4.1.2 shows the X-ray diffraction (= XRD) patterns of pristine $\text{Li}_3\text{V}_2(\text{PO}_4)_3$, delithiated $\text{Li}_{3-x}\text{V}_2(\text{PO}_4)_3$, and $\text{Li}_3\text{V}_2(\text{PO}_4)_3/\text{PEDOT}$. Pristine

$\text{Li}_3\text{V}_2(\text{PO}_4)_3$ has the pure monoclinic phase without any contaminations or second phases. Its lattice parameter using the ($P 1 21/n 1$) space group is $a = 8.5987(6)\text{\AA}$, $b = 8.5885(6)\text{\AA}$, $c = 12.0263(8)\text{\AA}$, and $\beta = 90.576(4)^\circ$. These are similar to those reported previous researches.[6, 9] The XRD pattern of $\text{Li}_{3-x}\text{V}_2(\text{PO}_4)_3$ is changed by Li extraction from the structure. The refinement of XRD pattern resulted in lattice parameters of $a = 8.5091(6)\text{\AA}$, $b = 8.6215(6)\text{\AA}$, $c = 11.9147(9)\text{\AA}$, and $\beta = 90.484(11)^\circ$. Compared to those of pristine $\text{Li}_3\text{V}_2(\text{PO}_4)_3$, the a and c lattice parameter are smaller while the b lattice parameter is larger. This change tendency of each lattice parameter of $\text{Li}_3\text{V}_2(\text{PO}_4)_3$ when Li ions are extracted from the structure is similar to the previous report[6] and inductively coupled plasma atomic emission spectroscopy (=ICP-AES) analysis shows that delithiated $\text{Li}_{3-x}\text{V}_2(\text{PO}_4)_3$ has less than 3Li ions ($x \approx 0.5$) in the structure. From these results, we could identify the Li extraction from $\text{Li}_3\text{V}_2(\text{PO}_4)_3$. The final material, $\text{Li}_3\text{V}_2(\text{PO}_4)_3/\text{PEDOT}$ obtained after the polymerization reaction has very similar XRD pattern and lattice parameters (Table 4.1.1) to pristine $\text{Li}_3\text{V}_2(\text{PO}_4)_3$. Any contaminations or second phases induced by PEDOT coating and Li reinsertion are not detected in the XRD pattern of $\text{Li}_3\text{V}_2(\text{PO}_4)_3/\text{PEDOT}$. Furthermore, we identified that the atomic ratio of Li, V, and P in $\text{Li}_3\text{V}_2(\text{PO}_4)_3/\text{PEDOT}$ composite is 1 : 1 : 1 using ICP-AES

analysis. These results clearly show that $\text{Li}_3\text{V}_2(\text{PO}_4)_3/\text{PEDOT}$ has ($P 1 21/n$ 1) space group and Li ions are reinserted into the structure.

4.1.3.3. Identifying the existence of PEDOT in $\text{Li}_3\text{V}_2(\text{PO}_4)_3$

The existence of PEDOT on $\text{Li}_3\text{V}_2(\text{PO}_4)_3$ can be identified by Fourier transform infrared spectroscopy (FT-IR) (Figure 4.1.3). The peaks at 1040 cm^{-1} , 1229 cm^{-1} , and 1197 cm^{-1} show the stretching vibration of $(\text{PO}_4)^{3-}$. [17, 18] The peaks at 634 cm^{-1} and 503 cm^{-1} were assigned to the V-O stretching (γ_1) and bending (γ_4) vibrations in the VO_6 octahedra, respectively. [17] The formation of PEDOT is identified by vibrations from the C-S bond in the thiophene ring (*ca.* 697 cm^{-1} by $\delta(\text{C-S-C})_{\text{ring}}$ and 830 cm^{-1} by $\nu(\text{C-S})_{\text{ring}}$) [19], stretching in the alkylendioxy group $\nu(-\text{COROC}-)$ ($1144\text{-}1128$, $1093\text{-}1076$ and $1052\text{-}1047\text{ cm}^{-1}$) [19], and polymer *p*-doping (*ca.* 1520 cm^{-1} and *ca.* 1320 cm^{-1}) [20]. This result are consistent with previous reports and prove the formation of PEDOT with $\text{Li}_3\text{V}_2(\text{PO}_4)_3$.

Transmission electron microscopy (TEM) analysis revealed the morphology of $\text{Li}_3\text{V}_2(\text{PO}_4)_3$ and an appreciable polymer coating on the surface of each $\text{Li}_3\text{V}_2(\text{PO}_4)_3$ particles. As shown in Figure 4.1.4(a) and (b), the $\text{Li}_3\text{V}_2(\text{PO}_4)_3$ particle with an average diameter of 200nm are uniformly coated with a thin layer of an amorphous layer expected to be PEDOT. The thickness of a thin layer is *ca.* 5-10nm. To identify that this layer is PEDOT,

we measured the element analysis by energy-dispersive X-ray spectroscopy (EDS) elemental mapping. Figure 4.1.4(c) and (d) shows that the each particles are composed of vanadium and phosphor atoms and is encircled by sulfur atoms. It means that PEDOT layer is uniformly coated on the surface of $\text{Li}_3\text{V}_2(\text{PO}_4)_3$ particles. Additionally, the cross-sectional composition profile in Figure 4.1.4(e) clearly reveals the core-shell structure, as the intensity of sulfur at the shell region is higher than that in core region, while the intensity of vanadium and phosphor at the shell region is lower than those in core region.

The weight percentage of PEDOT in the $\text{Li}_3\text{V}_2(\text{PO}_4)_3/\text{PEDOT}$ composite was measured by thermogravimetric analysis (TGA) (Figure 4.1.5). Unlike pristine $\text{Li}_3\text{V}_2(\text{PO}_4)_3$ without weight change, the weight of $\text{Li}_3\text{V}_2(\text{PO}_4)_3/\text{PEDOT}$ composite decreased by decomposition of PEDOT. The differential weight loss of pristine $\text{Li}_3\text{V}_2(\text{PO}_4)_3$ and $\text{Li}_3\text{V}_2(\text{PO}_4)_3/\text{PEDOT}$ composite was *ca.* 13%.

4.1.3.4. Electrochemical performance of $\text{Li}_3\text{V}_2(\text{PO}_4)_3/\text{PEDOT}$ composite

To investigate the effect of coated conducting polymer on the electrochemical properties, we tested the $\text{Li}_3\text{V}_2(\text{PO}_4)_3/\text{PEDOT}$ composite in a Li cell with galvanostatic measurement and compared the pristine

$\text{Li}_3\text{V}_2(\text{PO}_4)_3$ electrode with same amount of carbon instead of PEDOT. Figure 4.1.6(a) shows the discharge profiles of the $\text{Li}_3\text{V}_2(\text{PO}_4)_3/\text{PEDOT}$ composite measured at various current rates (1C, 3C, 5C, 10C, 30C, and 50C). This composite had excellent rate-capability. At 1C charge/discharge from 2.5V to 4.4V, The $\text{Li}_3\text{V}_2(\text{PO}_4)_3/\text{PEDOT}$ composite showed the capacities of 133 mAh g^{-1} at 1C, which are same to the theoretical capacity of $\text{Li}_3\text{V}_2(\text{PO}_4)_3$ when charged up to 4.4V and the 3-step extraction/insertion of Li ions (*ca.* 3.6V, 3.7V, and 4.1V) are clearly observed. About 83% of its theoretical capacity was retained at high current rate (30C). Comparison between $\text{Li}_3\text{V}_2(\text{PO}_4)_3/\text{PEDOT}$ composite and pristine $\text{Li}_3\text{V}_2(\text{PO}_4)_3$ clearly showed significant improvement of kinetic behavior at high current rate. As shown in Figure 4.1.6(b), the discharge capacity of $\text{Li}_3\text{V}_2(\text{PO}_4)_3/\text{PEDOT}$ composite at 10C is more than 10 times higher than that of pristine $\text{Li}_3\text{V}_2(\text{PO}_4)_3$. It is notable that PEDOT coating without conducting carbon such as acetylene black or super-P can dramatically enhance the power capability of $\text{Li}_3\text{V}_2(\text{PO}_4)_3$. Furthermore, $\text{Li}_3\text{V}_2(\text{PO}_4)_3/\text{PEDOT}$ composite exhibits excellent cyclability with a negligible capacity fade. At 10C rate, 122 mAh g^{-1} (*ca.* 92% of the theoretical capacity when charged up to 4.4V) was stably retained during 100 cycles.

4.1.4 Summary

In summary, we demonstrated that the electrochemical properties of monoclinic $\text{Li}_3\text{V}_2(\text{PO}_4)_3/\text{PEDOT}$ composite are significantly improved without any conductive carbon. By intrinsic oxidation power of delithiated $\text{Li}_{3-x}\text{V}_2(\text{PO}_4)_3$, EDOT (monomer of PEDOT) can be polymerized on the surface of $\text{Li}_3\text{V}_2(\text{PO}_4)_3$ and PEDOT is uniformly deposited. The coating of conducting polymer, PEDOT on the surface of $\text{Li}_3\text{V}_2(\text{PO}_4)_3$ lead to higher power capability without conductive carbon. The utilization of core-shell structure with conductive polymer is suggested as a promising strategy for lithium ion batteries with high power performance.

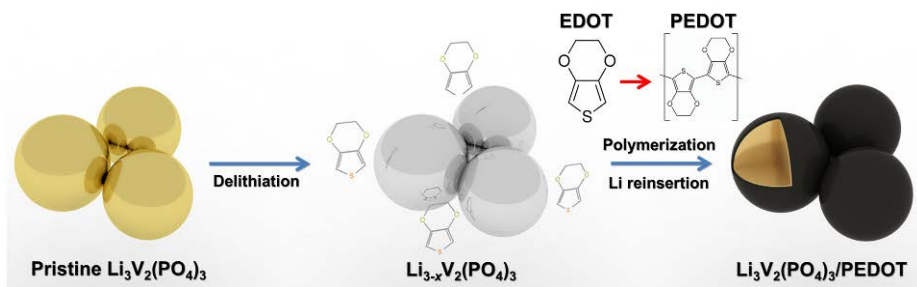


Figure 4.1.1 Schematic illustration of the fabrication process of $\text{Li}_3\text{V}_2(\text{PO}_4)_3/\text{PEDOT}$ composite

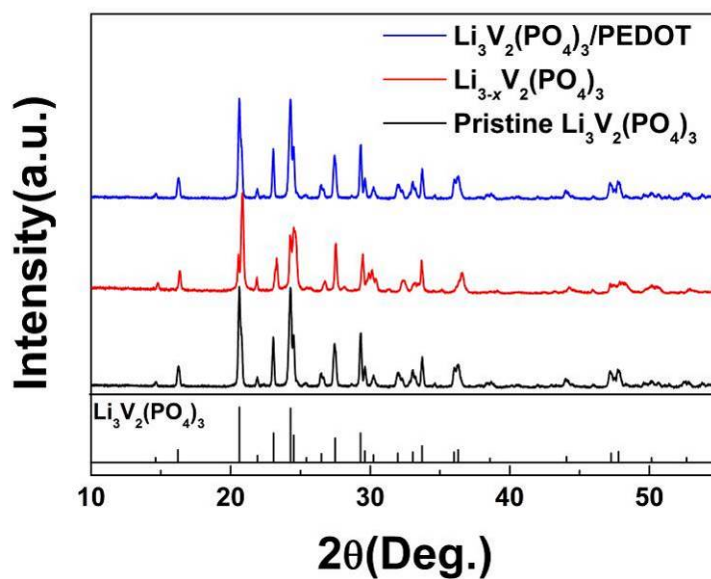


Figure 4.1.2 XRD patterns of pristine $\text{Li}_3\text{V}_2(\text{PO}_4)_3$ (black), partially delithiated $\text{Li}_{3-x}\text{V}_2(\text{PO}_4)_3$ (red), and $\text{Li}_3\text{V}_2(\text{PO}_4)_3/\text{PEDOT}$ composite (blue)

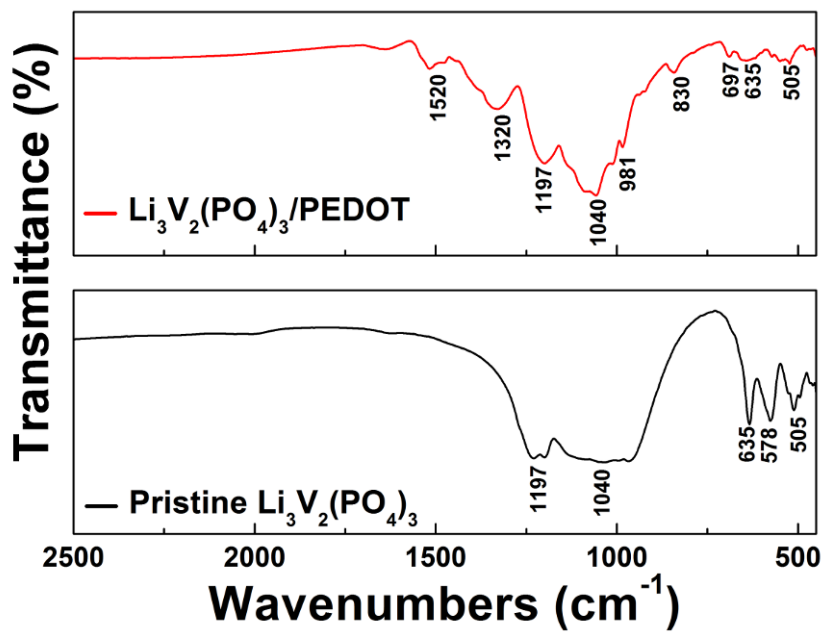


Figure 4.1.3 Comparison of FT-IR between $\text{Li}_3\text{V}_2(\text{PO}_4)_3/\text{PEDOT}$ composite and pristine $\text{Li}_3\text{V}_2(\text{PO}_4)_3$

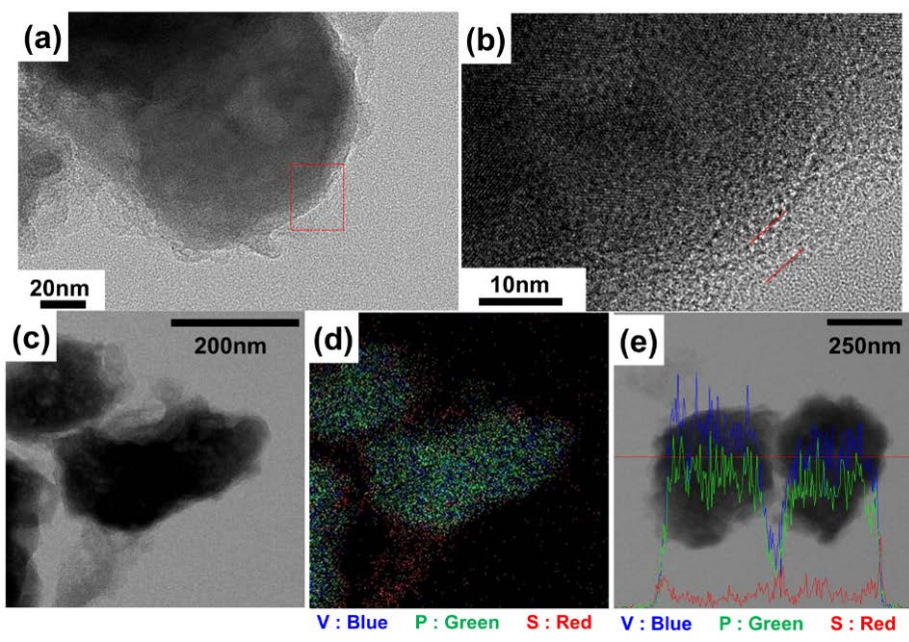


Figure 4.1.4 (a,b) TEM images of $\text{Li}_3\text{V}_2(\text{PO}_4)_3/\text{PEDOT}$ composite. (c-e) TEM analysis in bright-field mode (c), elemental analysis using energy-dispersive X-ray mapping (d) (V: blue, P: green, S: red), and cross-sectional composition line profiles (e) (V: blue, P: green, S: red) of $\text{Li}_3\text{V}_2(\text{PO}_4)_3/\text{PEDOT}$ composite

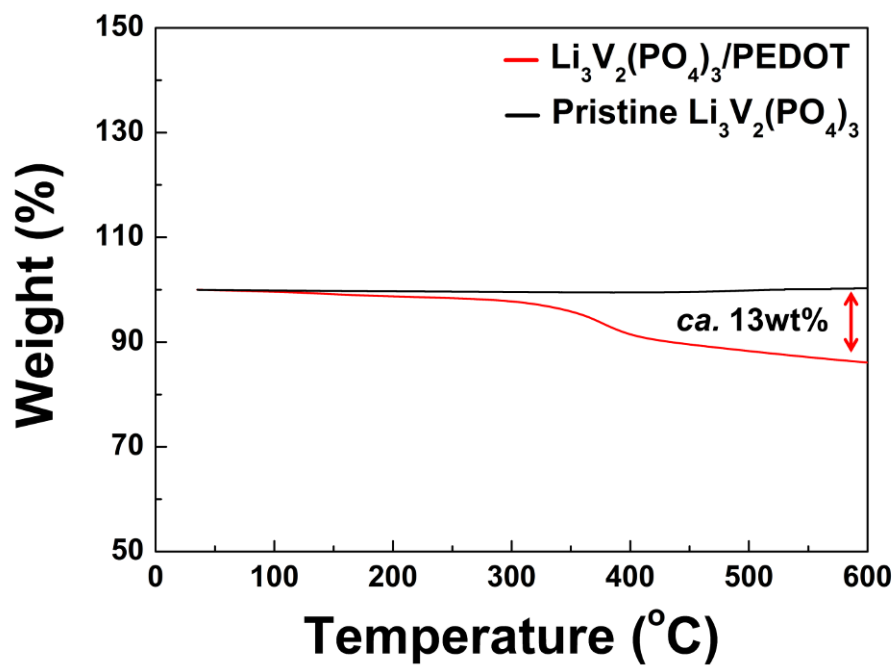


Figure 4.1.5 TGA profile of Li₃V₂(PO₄)₃/PEDOT composite and pristine Li₃V₂(PO₄)₃

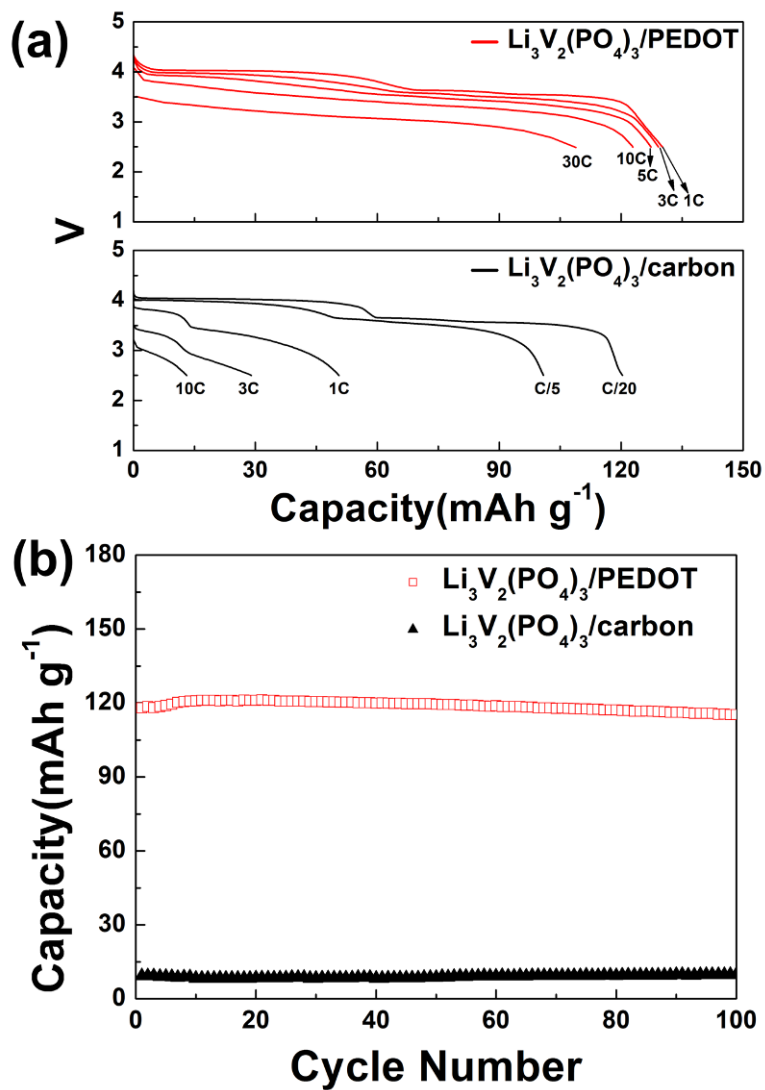


Figure 4.1.6 (a) Specific discharge capacities of $\text{Li}_3\text{V}_2(\text{PO}_4)_3/\text{PEDOT}$ and $\text{Li}_3\text{V}_2(\text{PO}_4)_3/\text{carbon}$ in the voltage range 2.5-4.4 V with various current rates. (b) Cyclability of $\text{Li}_3\text{V}_2(\text{PO}_4)_3/\text{PEDOT}$ and $\text{Li}_3\text{V}_2(\text{PO}_4)_3/\text{carbon}$ electrode in the voltage range 2.5-4.4 V with a current rate of 10C (1C = 133 mA g⁻¹)

	Pristine $\text{Li}_3\text{V}_2(\text{PO}_4)_3$	$\text{Li}_{3-x}\text{V}_2(\text{PO}_4)_3$	$\text{Li}_3\text{V}_2(\text{PO}_4)_3$ /PEDOT
<i>a</i>	8.5987(6)Å	8.5091(6)Å	8.5977(6)Å
<i>b</i>	8.5885(6)Å	8.6215(6)Å	8.5880(6)Å
<i>c</i>	12.0263(8)Å	11.9147(9)Å	12.0252(8)Å
β	90.576(4)°	90.484(11)°	90.573(4)°

Table 4.1.1 Lattice parameters of pristine $\text{Li}_3\text{V}_2(\text{PO}_4)_3$, delithiated $\text{Li}_{3-x}\text{V}_2(\text{PO}_4)_3$, and $\text{Li}_3\text{V}_2(\text{PO}_4)_3$ /PEDOT composite

4.1.5 References

- [1] M. Armand, J. M. Tarascon, *Nature*, **451**, 652-657 (2008) .
- [2] Y. J. Lee, H. Yi, W. J. Kim, K. Kang, D. S. Yun, M. S. Strano, G. Ceder, A. M. Belcher , *Science*, **324** , 1051-1055 (2009).
- [3] J. Kim, D. H. Seo, S. W. Kim, Y. U. Park, K. Kang, *Chem. Commun.*, **46** , 1305-1307 (2010).
- [4] P. G. Bruce, B. Scrosati, J. M. Tarascon, *Angew. Chem. Int. Ed.*, **47**, 2930-2946 (2008).
- [5] H. Gwon, D. H. Seo, S. W. Kim, J. Kim, K. Kang, *Adv. Funct. Mater.*, **19**, 3285-3292 (2009).
- [6] H. Huang, S. C. Yin, T. Kerr, N. Taylor, L. F. Nazar, *Adv. Mater.*, **14**, 1525 (2002).
- [7] M. M. Ren, Z. Zhou, X. P. Gao, W. X. Peng, J. P. Wei, *J. Phys. Chem. C*, **112**, 5689-5693 (2008).
- [8] H. D. Liu, P. Gao, J. H. Fang, G. Yang, *Chem. Commun.*, **47**, 9110- 9112 (2011).
- [9] A. R. Cho, J. N. Son, V. Aravindan, H. Kim, K. S. Kang, W. S. Yoon, W. S. Kim, Y. S. Lee, *J. Mater. Chem.*, **22**, 6556-6560 (2012).
- [10] S. M. Oh, S. W. Oh, C. S. Yoon, B. Scrosati, K. Amine, Y. K. Sun, *Adv. Funct. Mater.*, **20**, 3260-3265 (2010).

- [11] J. Kim, Y. U. Park, D. H. Seo, J. Kim, S. W. Kim, K. Kang, *J. Electrochem. Soc.*, **158**, A250-A254 (2011).
- [12] J. Barker, M. Y. Saidi, J. L. Swoyer, *J. Electrochem. Soc.*, **150**, A1394-A1398 (2003).
- [13] Y. U. Park, D. H. Seo, B. Kim, K. P. Hong, H. Kim, S. Lee, R. A. Shakoor, K. Miyasaka, J. M. Tarascon, K. Kang, *Sci. Rep.*, **2**, 704 (2012).
- [14] M. Yonemura, A. Yamada, Y. Takei, N. Sonoyama, R. Kanno, *J. Electrochem. Soc.*, **151**, A1352-A1356 (2004).
- [15] S. Nishimura, M. Nakamura, R. Natsui, A. Yamada, *J. Am. Chem. Soc.*, **132**, 13596-13597 (2010).
- [16] N. Furuta, S. Nishimura, P. Barpanda, A. Yamada, *Chem. Mater.*, **24**, 1055-1061 (2012).
- [17] T. Drezen, N. H. Kwon, P. Bowen, I. Teerlinck, M. Isono, I. Exnar, *J. Power Sources*, **174**, 949-953 (2007).
- [18] Y.-U. Park, J. Kim, H. Gwon, D. H. Seo, S. W. Kim, K. Kang, *Chem. Mater.*, **22**, 2573-2581 (2010).
- [19] C. M. Doherty, R. A. Caruso, B. M. Smarsly, P. Adelhelm, C. J. Drummond, *Chem. Mater.*, **21**, 5300-5306 (2009).
- [20] A. A. Salah, A. Mauger, K. Zaghbi, J. B. Goodenough, N. Ravet, M. Gauthier, F. Gendron, C. M. Julien, *J. Electrochem. Soc.*, **153**, A1692- A1701

(2006).

[21] Y. G. Wang, Y. R. Wang, E. J. Hosono, K. X. Wang, H. S. Zhou, *Angew. Chem. Int. Ed.*, **47**, 7461-7465 (2008).

[22] Y. Q. Hu, M. M. Doeff, R. Kostecki, R. Finones, *J. Electrochem. Soc.*, **151**, A1279-A1285 (2004).

[23] A. V. Murugan, T. Muraliganth, A. Manthiram, *Electrochem. Commun.*, **10**, 903-906 (2008).

[24] K. S. Park, S. B. Schougaard, J. B. Goodenough, *Adv. Mater.*, **19**, 848-851 (2007).

[25] D. Lepage, C. Michot, G. X. Liang, M. Gauthier, S. B. Schougaard, *Angew. Chem. Int. Ed.*, **50**, 6884-6887 (2011).

[26] A. R. Wizansky, P. E. Rauch, F. J. Disalvo, *J. Solid State Chem.*, **81**, 203-207 (1989).

[27] C. Kvarnström, H. Neugebauer, S. Blomquist, H. J. Ahonen, J. Kankare, A. Ivaska, *Electrochim. Acta*, **44**, 2739-2750 (1999).

[28] C. Kvarnström, H. Neugebauer, A. Ivaska, N. S. Sariciftci, *J. Mol. Struct.*, **521**, 271-277 (2000).

Chapter 5. Alluaudite Electrode

5.1 LiFePO₄ with an alluaudite crystal structure for lithium ion batteries

5.1.1 Research Background

The large-scale energy storage system for electric vehicles requires batteries with high safety, cost-effectiveness and high energy/power density.[1-4] In search for electrode materials for such batteries, the olivine LiFePO₄ has been one of the most intensively studied cathode in recent years.[5-13] The combination of the naturally abundant Fe and the stable covalent poly-anion unit (PO₄³⁻) in LiFePO₄ is the important aspect that makes it cost-effective and safe electrode material for the next-generation lithium ion batteries.[5-17] LiFePO₄ continues to surprise researchers with its unusual physico-chemical characteristics.[9-11, 18-20] Herein, we explore further the LiFePO₄ chemistry by introducing a novel non-olivine LiFePO₄ with an alluaudite crystal structure. While the relationship between structure and property of material forms a basis of materials chemistry, the new polymorphic structure of LiFePO₄ will provide further insights on LiFePO₄ chemistry. Furthermore, we found that the alluaudite LiFePO₄ shows promising electrochemical properties allowing reversible extraction and insertion of *ca.* 0.8Li⁺ in the structure with one-phase based reaction.

Alluaudite compounds have the general formula $X(1)X(2)M(1)M(2)_2(PO_4)_3$, in which X and M are different cation species.[21] The structure is comprised of infinite chains of two edge-shared $M(2)O_6$ octahedra linked by distorted $M(1)O_6$ octahedra as illustrated in Figure 5.1.1(a). M(1) and M(2) are occupied by Fe, and X(1) and X(2) are filled with either Na or Li in the targeted structure. The chains are connected by tetrahedral PO_4 units, while X cations reside in tunnels along the *c*-axis providing plausible diffusion pathways. Previous studies have shown that compounds such as $NaMnFe_2(PO_4)_3$, $Li_{0.5}Na_{0.5}MnFe_2(PO_4)_3$ and $Na_2FeMn_2(PO_4)_3$ can be prepared.[22-24] Inspired by this, we attempted to prepare a novel $Na_2Fe_3(PO_4)_3$ ($=Na_{0.67}FePO_4$), as a starting material to the alluaudite $LiFePO_4$. Hatert *et al.* reported that the structural refinements of the alluaudite structure evidence the existence of three more cationic sites.[25] These sites are located in the channels at crystallographic positions that are different from those of X(1) and X(2) sites implying the feasibility of further insertion of cations into channel.[25] Moreover, the presence of partial M^{3+} in the parent alluaudite structure enables the additional Li^+ or Na^+ ions to be intercalated.[22, 23] Therefore, we supposed that the alluaudite $LiFePO_4$ can be synthesized from the $Na_{0.67}FePO_4$ by the ion-exchange of Na with Li with additional lithiation process.

5.1.2 Experimental Section

5.1.2.1. The synthesis process

Na_2CO_3 (Sigma Aldrich, 98%), $\text{Fe}(\text{NO}_3)_3 \cdot 9\text{H}_2\text{O}$ (Sigma Aldrich, 98%), $\text{FeC}_2\text{O}_4 \cdot 2\text{H}_2\text{O}$ (Sigma Aldrich, 98%), and $\text{NH}_4\text{H}_2\text{PO}_4$ (Fluka, 98%) with molar ratios of 0.33 : 0.33 : 0.67 : 1 were used as precursors. They were thoroughly mixed and grounded by high energy ball-milling. The mixed precursors were then fired at 350°C under Ar conditions for 5 hours. The mixture was then re-ground and manually pelletized using a disk-shaped mold. After pre-heating, we calcined the pellet at 600°C under Ar conditions for 10 hours.

5.1.2.2. The ion-exchange process of $\text{Li}_{0.67}\text{FePO}_4$

To prepare $\text{Li}_{0.67}\text{FePO}_4$, ion-exchange of $\text{Na}_{0.67}\text{FePO}_4$ was carried out in a refluxing solution of 5M LiBr in Hexanol for 18 hours at 170°C.

5.1.2.3. Materials characterization

The stoichiometry of the delithiated compound was determined by inductively coupled plasma-atomic emission spectroscopy (ICP-AES). Powder XRD of all materials was carried out on a Bruker D8-Advantage powder diffractometer using Cu $K\alpha$ radiation ($= 1.54178 \text{ \AA}$) from $2\theta = 10$ to 60° at 1s per step of 0.01° . The *ex-situ* XRD of fully lithiated alluaudite- LiFePO_4 was determined by XRD (Bruker D8 ADVANCE and Rigaku

D/Max 2500) with Cu K α radiation ($\lambda = 1.54178 \text{ \AA}$). Data were recorded over a 2θ range of 10° to 60° , with a step size of 0.02° . Each step was exposed for 4s. ND analysis of $\text{Na}_{0.67}\text{FePO}_4$ and $\text{Li}_{0.67}\text{FePO}_4$ was carried out to determine each position and occupancy of all atoms. ND data were collected over a 2θ range between 0° and 180° with a step size of 0.05° , and $\lambda = 1.8348 \text{ \AA}$ was supplied by a Ge (331) single-crystal monochromator on a high-resolution powder diffractometer (HRPD) at the HANARO facility at the Korea Atomic Energy Research Institute. Structural refinements were done by the Rietveld method with Fullprof software. Fe K-edge X-ray absorption spectra (XAS) were taken on the 1D beamline at the Pohang Accelerator Laboratory (PAL). Fe K-edge energy calibration was performed using Fe metal foil as reference. A reference spectrum was simultaneously recorded for in-situ spectrum using Fe metal foil.

5.1.2.4. Electrochemistry

Electrochemical tests were performed in a CR2016-type coin cell assembled in an Ar-filled glove-box. The slurry of 75 wt% $\text{Na}_{0.67}\text{FePO}_4$ and $\text{Li}_{0.67}\text{FePO}_4$, 26 wt% carbon black (Super-P), and 9 wt% polyvinylidene fluoride dispersed in N-methyl-2-pyrrolidone (NMP) was prepared and cast on aluminum foil. NMP was evaporated at 120°C for 2 hours. Electrochemical cells were assembled in a CR2016 type coin cell with a Li

counter electrode, separator (Celgard 2400), and 1 M LiPF₆ electrolyte in a mixture of 1:1 ethyl carbonate/dimethyl carbonate in an Ar-filled glove box. The charge/discharge test was performed using a galvanostat (WonA Tech).

5.1.3 Results and discussion

5.1.3.1 Structural information of alluaudite materials

Alluaudite Na_{0.67}FePO₄ powder was synthesized through the conventional solid-state route. The X-ray Diffraction (XRD, Figure 5.1.2) and Neutron Diffraction (ND) analysis in Figure 5.1.1(b) indicates that a novel alluaudite Na_{0.67}FePO₄ (*a*-Na_{0.67}FePO₄) was successfully obtained and can be indexed using the monoclinic (*C* 1 2/*c* 1) space group similar to other known alluaudite-based materials.[22, 24] No noticeable contaminations were detected. The refinement of ND pattern resulted in lattice parameters of $a = 11.8649(7)\text{\AA}$, $b = 12.5238(7)\text{\AA}$, $c = 6.4667(4)\text{\AA}$, and $\beta = 114.396(3)^\circ$, in consistent with results from the XRD refinement (Table 5.1.1). The good quality of the refinement shown by the small reliability factors suggests the adequacy of the structural model to describe the structure of *a*-Na_{0.67}FePO₄ (Table 5.1.2).

The well crystallized *a*-Na_{0.67}FePO₄ was used as a precursor to obtain the alluaudite Li_{0.67}FePO₄ (=partially delithiated phase of alluaudite LiFePO₄). The alluaudite Li_{0.67}FePO₄ was prepared from a soft chemical ion-exchange

method. The inductively coupled plasma (ICP) measurement revealed that the chemical composition of the ion-exchanged lithium phase was $\text{Li}_{0.47}\text{Na}_{0.2}\text{FePO}_4$ (hereafter, $a\text{-Li}_{0.67}\text{FePO}_4$). While various conditions of ion-exchange were carried out, we found that the maximum exchange of Na with Li was 0.47 without destructing the alluaudite structure. Stronger ion-exchange conditions resulted in a significant Fe dissolution (Table 5.1.3) and finally led to the collapse of the structure (Figure 5.1.3). It implies that the residual Na^+ ions aid to sustain the $\text{Li}_{0.67}\text{FePO}_4$ within the alluaudite structure, while the thermodynamically stable phase of $\text{Li}_{0.67}\text{FePO}_4$ is the mixture of two olivines; LiFePO_4 and FePO_4 .

The crystallinity of $a\text{-Li}_{0.67}\text{FePO}_4$ phase was studied by XRD analysis (Figure 5.1.4). The comparison of the XRD pattern with that of $a\text{-Na}_{0.67}\text{FePO}_4$ reveals that the general patterns are similar, but peaks have shifted to the higher 2θ angle indicating that the topotactic ion-exchange between Na and Li has occurred. The refinement of the XRD pattern using the space group of $C 1 2/c 1$ resulted in lattice parameters of $a = 11.8569(4)\text{\AA}$, $b = 12.3863(3)\text{\AA}$, $c = 6.36381(14)\text{\AA}$, and $\beta = 114.514(3)^\circ$ without any contaminations or second phases detected. The a , b and c lattice parameters are smaller than those of $a\text{-Na}_{0.67}\text{FePO}_4$, which is attributed to the smaller ionic radius of Li^+ ($r = 0.74\text{\AA}$) compared to that of Na^+ ($r =$

1.02Å).[26] One notable difference in the XRD pattern compared to that of $a\text{-Na}_{0.67}\text{FePO}_4$ is that the (-111) peak has substantially grown in the ion-exchanged phase. From the series of XRD simulation in Figure 5.1.5, we found out that the (-111) peak intensity is sensitively affected by the partial occupancy of Fe in M(1) site as a result of Li-Fe site disordering. (020) and (200) peaks also strongly depended on the relative occupancies of Fe and Li sites. The detailed site occupancies and its effect on the XRD pattern are provided in Table 5.1.4. Unlike $a\text{-Na}_{0.67}\text{FePO}_4$, the $a\text{-Li}_{0.67}\text{FePO}_4$ possesses partial Fe-Li site exchange, which is believed to be induced during the ion-exchange process. In order to clearly quantify the Li and Fe site occupancies, ND analysis was further carried out in Figure 5.1.6. The detailed refinement of occupancies revealed that about 20% of Li-Fe disordering has occurred. (Table 5.1.5) The lattice parameters obtained from the ND pattern were close to those from the XRD.

The alluaudite LiFePO_4 ($a\text{-LiFePO}_4$) could be obtained through additional lithiation of $a\text{-Li}_{0.67}\text{FePO}_4$. During the lithiation, noted were a slight structural change and a shift of oxidation state of Fe. Figure 5.1.7(a) shows the XRD pattern of the $a\text{-LiFePO}_4$. While the patterns become generally broader, the peak positions of the $a\text{-LiFePO}_4$ have slightly shifted compared to that of the $a\text{-Li}_{0.67}\text{FePO}_4$. Close investigation in Figure 5.1.7(b) clearly

indicates that main peaks of a -LiFePO₄ have shifted to lower angle implying the expansion of the crystal with lithiation. The refined lattice parameters of a -LiFePO₄ were $a = 11.868(3)\text{\AA}$, $b = 12.445(4)\text{\AA}$, $c = 6.4049(13)\text{\AA}$, and $\beta = 114.65(3)^\circ$ (Figure 5.1.7(a)). The a , b and c lattice parameters are slightly bigger than those of Li_{0.67}FePO₄. The expansion of crystal lattices strongly suggests the intercalation of lithium ions in the structure.

In addition, we traced the change of the oxidation state of Fe using X-ray absorption spectroscopy (XAS). Figure 5.1.7(c) compares the Fe K-edge X-ray absorption near edge structure (XANES) spectra of the a -Li _{x} FePO₄ ($0 \leq x \leq 1$). Fe K-edge of the pristine a -Li_{0.67}FePO₄ shifted toward lower energy when further lithiated. This indicates that Fe^{2.33+} in Li_{0.67}FePO₄ was reduced to lower valence state (Fe²⁺). The position of the Fe-K edge XANES spectrum of the a -LiFePO₄ agrees well with that of FeO (Fe²⁺ reference), which reveals that the Fe ions exist mainly as Fe²⁺ in the lithiated alluaudite phase, a -LiFePO₄. The reduction to Fe²⁺ as well as the expansion of lattice supports that a novel alluaudite LiFePO₄ phase was successfully obtained. It was further confirmed that the Fe K-edge shifts back to higher energy with delithiation implying that reversible redox reaction can occur in the alluaudite phase.

5.1.3.2 Electrochemical performance of alluaudite LiFePO₄

The electrochemical activity of the a -LiFePO₄ was investigated in Li cells. Figure 5.1.8(a) shows that about 80% of Li in a -LiFePO₄ could be extracted and reinserted reversibly. At a C/20 rate, the specific capacity is approximately 140 mAh g⁻¹, whereas the theoretical value of a -LiFePO₄ based on full delithiation is *ca.* 170 mAh g⁻¹. The slightly lower specific capacity than the theoretical value is attributed to the existence of residual Na in the structure. The *ca.* 0.2Na⁺ ions remaining in the structure appears to be immobile during the electrochemical cycling. However, the existence of residual Na ions is believed to stabilize the alluaudite structure. The lithiation and delithiation reaction in the a -LiFePO₄ was highly reversible. The initial capacity of 140 mAh g⁻¹ could be retained even after 25 times of cycles. Also, the shape of the charge/discharge profile did not change significantly over cycles indicating that phase transition to the olivine does not occur.

5.1.3.1 Comparison with olivine LiFePO₄

It is notable that the electrochemical activity of a -LiFePO₄ is centered *ca.* 3.0V vs. Li⁺ and is different from the typical redox potential of the olivine LiFePO₄ (*ca.* 3.4V) despite the identical Fe²⁺/Fe³⁺ redox couple. We suppose that it is related to the different local environments of Fe in two crystal structures. In the olivine framework, the FeO₆ octahedrons share corners

with other FeO_6 octahedrons. On the other hand, all FeO_6 octahedrons in the alluaudite share edges, which results in more significant overlaps of Fe orbitals among them. Less localization of charge in the Fe due to the edge sharing in the alluaudite is believed to reduce the redox potential of $\text{Fe}^{2+}/\text{Fe}^{3+}$. [27] The corner-sharing between FeO_6 and PO_4 in the alluaudite in comparison to the edge-sharing in the olivine is also likely to reduce the inductive effect lowering the redox potential further. [28] In addition to the difference in the redox potential, the shape of the charge/discharge profile deviates from the typical flat electrochemical profile of the olivine LiFePO_4 . The slanted shape of the charge/discharge profile is the characteristics of one-phase based lithiation and delithiation. In order to confirm this, the de/lithiation mechanism of *a*- LiFePO_4 was investigated by a series of *ex-situ* XRD of the electrodes. Figure 5.1.8(b) shows that the peaks continuously shift without the evolution of any new peaks, which corresponds to the characteristic behavior of one-phase based charge/discharge reaction. It is clearly contrasted with the olivine LiFePO_4 electrode that undergoes two-phase based charge/discharge reaction between LiFePO_4 and FePO_4 . We found that lithium insertion and extraction can occur reasonably fast in the alluaudite structure. Figure 5.1.8(c) compares the specific capacities at various current densities from C/20 to 3C. At a C/20 rate, almost all lithium

except the residual 0.2Na in the structure could be reinserted into the alluaudite. At the ten times higher rate of C/2, it could still retain about 75% of the full capacity. While no special treatments such as nano-sizing were done on the sample, we attribute the reasonably high rate performance to the open crystal structure of the alluaudite. It should be further noted that about 20% of Li and Fe site exchange is present in our sample. With similar level of Li/Fe site disorder, the olivine LiFePO₄ would not be electrochemically active.[29] It is believed that with further optimization in the synthesis such as reducing the Li/Fe disorder and the particle size, the rate performance would be significantly enhanced.

5.1.3 Summary

In summary, a novel non-olivine LiFePO₄ with alluaudite structure was successfully prepared, and its structure was investigated in detail through combined ND and XRD analysis. The alluaudite LiFePO₄ showed fundamentally different electrochemical behavior from that of the well-known olivine LiFePO₄, while the same Fe²⁺/Fe³⁺ redox reaction occurs. Almost all lithium ions in *a*-LiFePO₄ could be reversibly extracted and inserted with reasonable fast rates presenting it as another possible iron-based cathode for lithium rechargeable batteries. We believe that this study will provide an insight on the relation between structure and the

electrochemical activity of LiFePO_4 chemistry.

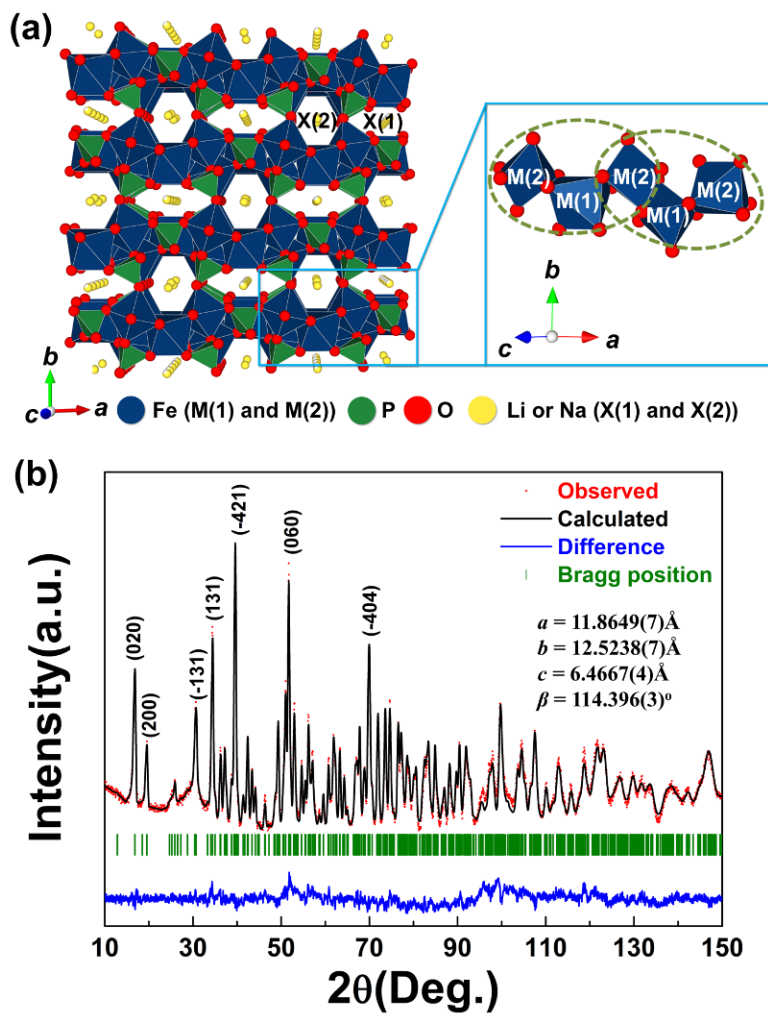


Figure 5.1.1 (a) Schematic representation of alluaudite $\text{Na}_{0.67}\text{FePO}_4$ or $\text{Li}_{0.67}\text{FePO}_4$. The local geometry of the chains of edge-shared FeO_6 octahedra linked by tetrahedra PO_4 units in the alluaudite, (b) Rietveld refinements of the ND pattern of $\text{Na}_{0.67}\text{FePO}_4$ with its refined lattice parameters ($R_P = 4.15\%$, $R_I = 5.40\%$, $R_F = 2.17\%$, and $\chi^2 = 6.17\%$)

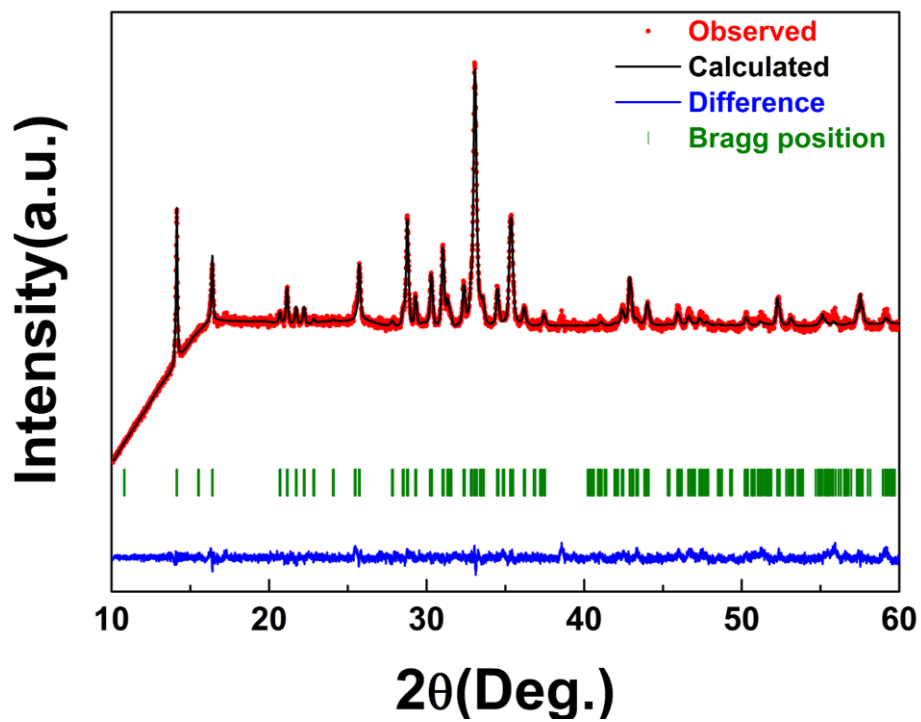


Figure 5.1.2 Rietveld refinements of the XRD pattern of $\text{Na}_{0.67}\text{FePO}_4$. ($R_p = 1.26\%$, $R_I = 0.78\%$, $R_F = 0.74\%$, $\chi^2 = 2.17\%$)

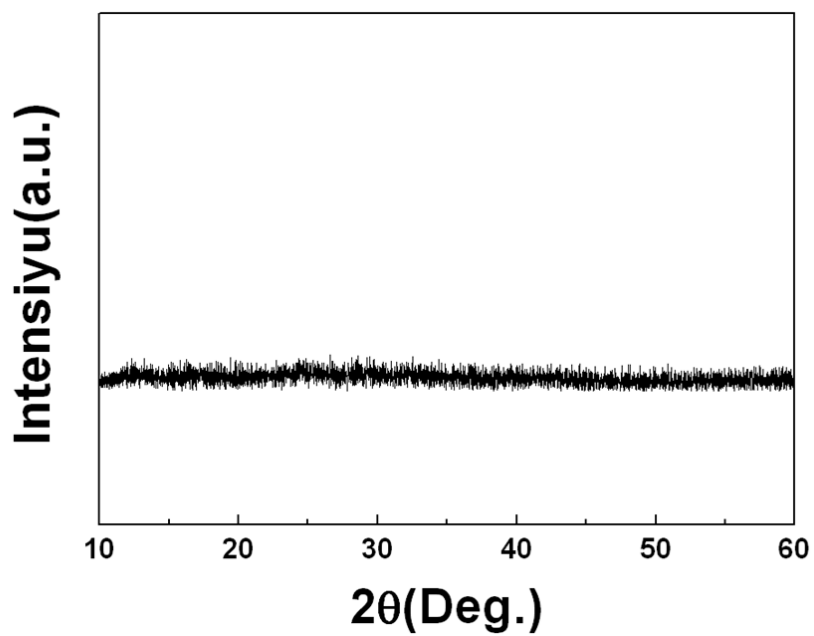


Figure 5.1.3 The XRD pattern of ion-exchanged alluaudite $\text{Li}_{0.67}\text{FePO}_4$ at harsh condition (25M LiBr in Hexanol for 48 hours at 170°C)

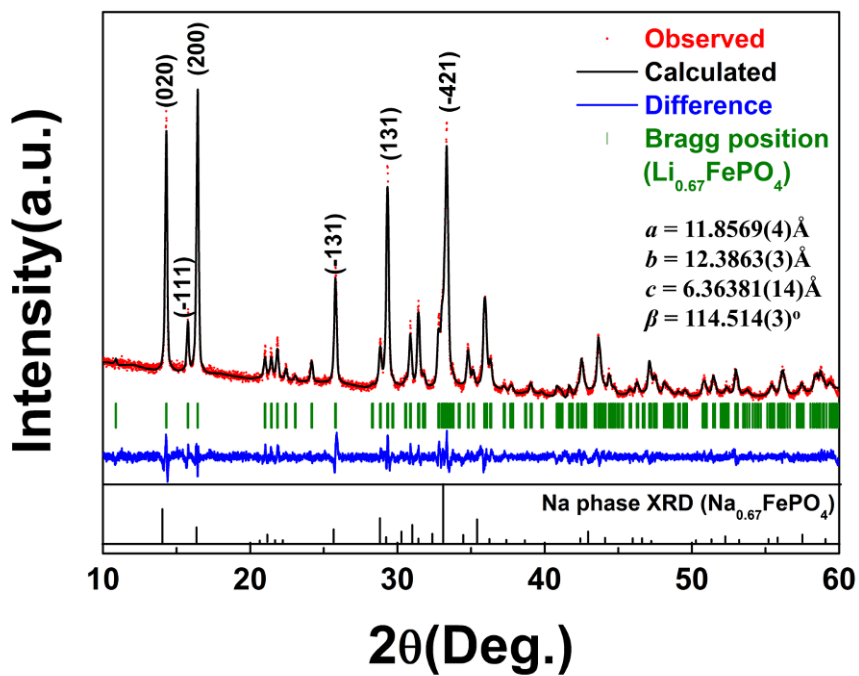


Figure 5.1.4 Rietveld refinements of the XRD pattern of alluaudite

$\text{Li}_{0.67}\text{FePO}_4$ ($R_p = 4.51\%$, $R_I = 5.52\%$, $R_F = 5.86\%$, and $\chi^2 = 2.10\%$)

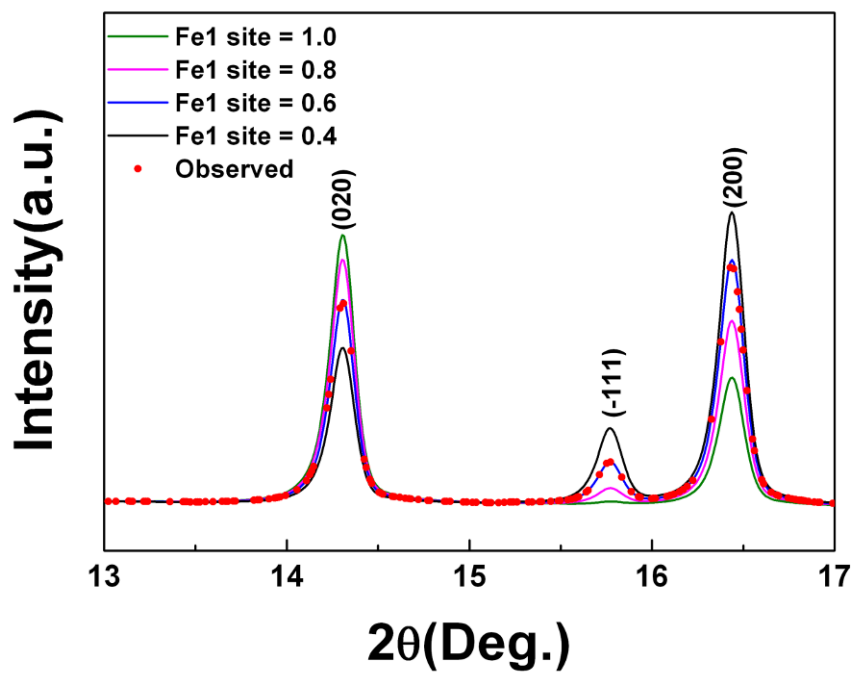


Figure 5.1.5 Simulated XRD patterns of alluaudite $\text{Li}_{0.67}\text{FePO}_4$ as a function of partial occupancy of Fe

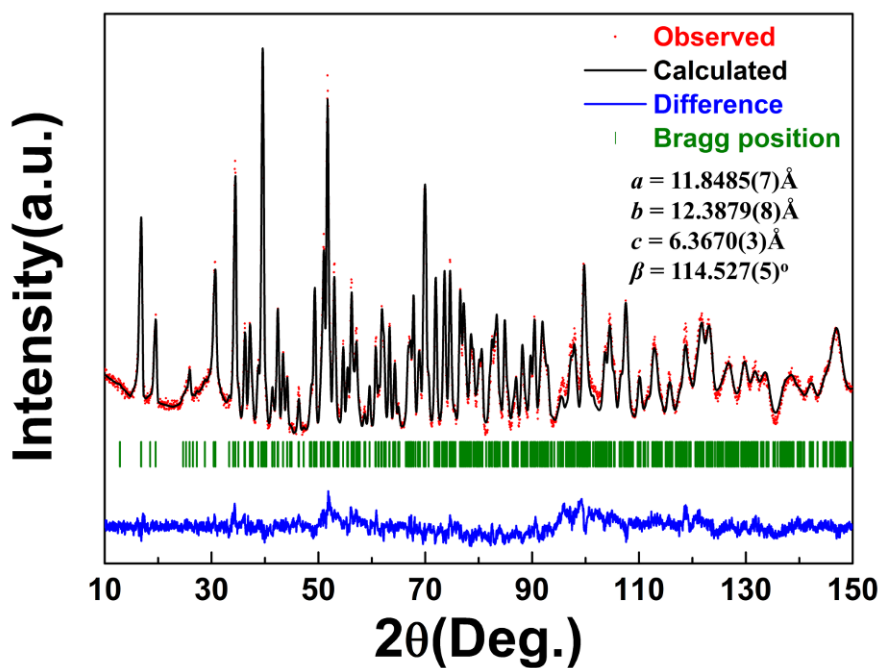


Figure 5.1.6 Rietveld refinements of the ND pattern of alluaudite $\text{Li}_{0.67}\text{FePO}_4$ with its refined lattice parameters. ($R_p = 2.17\%$, $R_I = 3.41\%$, $R_F = 1.88\%$, $\chi^2 = 2.28\%$)

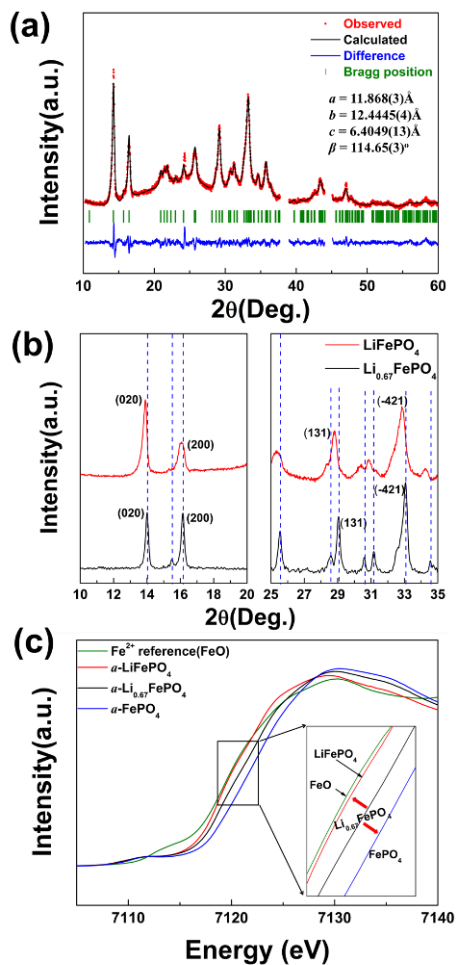


Figure 5.1.7 (a) XRD of fully lithiated alluaudite LiFePO_4 with its refined lattice parameters. ($R_p = 2.86\%$, $R_I = 2.39\%$, $R_F = 2.66\%$, and $\chi^2 = 2.32\%$). The blank regions between 37.7° and 39° and between 44° and 45.1° are the XRD peaks of Al foil. (b) Comparison of XRD patterns between alluaudite $\text{Li}_{0.67}\text{FePO}_4$ and alluaudite LiFePO_4 . (c) Normalized Fe K-edge XANES spectra for alluaudite Li_xFePO_4

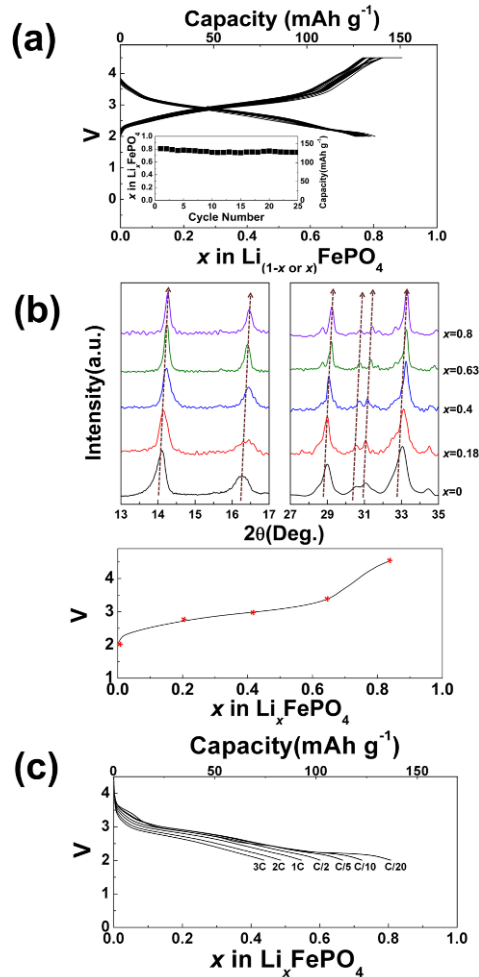


Figure 5.1.8 (a) Galvanostatic curves of alluaudite LiFePO_4 during 25 cycles at C/20 (inset: cyclability of alluaudite LiFePO_4 during 25 cycles at C/20), (b) *ex situ* XRD patterns of $a\text{-Li}_x\text{FePO}_4$ ($0 \leq x \leq 0.8$), (c) charge profile of $a\text{-Li}_x\text{FePO}_4$ ($0 \leq x \leq 0.8$) for *ex situ* XRD, (d) discharge curves of alluaudite LiFePO_4 as a function of C rate from C/20 to 3C (charging with CCCV mode (C/20 rate and 5 hour holding at 4.5V))

		Lattice parameter
Na_{0.67}FePO₄	<i>a</i>	11.8710(5) Å
	<i>b</i>	12.5180(4) Å
	<i>c</i>	6.4776(19) Å
	<i>β</i>	114.456(3) Å

Table 5.1.1 Lattice parameters of alluaudite Na_{0.67}FePO₄

Atom	Multiplicity	<i>x</i>	<i>y</i>	<i>z</i>	<i>B</i> _{iso}	Occupancy
Na1	4	0	0.5	0	2.09(2)	1
Na2	4	0	-0.0209(12)	0.25	2.4(3)	1
Fe1	4	0	0.2686(4)	0.25	1.90(10)	1
Fe2	8	0.2803(4)	0.6550(3)	0.3628(7)	1.00(5)	1
P1	4	0	0.7117(7)	0.25	1.00(16)	1
P2	8	0.2394(6)	0.8905(5)	0.1242(12)	0.87(11)	1
O1	8	0.4555(5)	0.7175(4)	0.5417(11)	0.08(9)	1
O2	8	0.1042(5)	0.6369(4)	0.2543(10)	0.68(9)	1
O3	8	0.3351(5)	0.6635(5)	0.1054(10)	0.20(9)	1
O4	8	0.1251(6)	0.4008(5)	0.3261(10)	0.49(9)	1
O5	8	0.2237(5)	0.8221(4)	0.3129(9)	0.36(9)	1
O6	8	0.3233(4)	0.5023(5)	0.3858(9)	0.36(9)	1

Table 5.1.2 Atomic position and occupancy of refined Na_{0.67}FePO₄ using the ND pattern

	Atom	Atomic ratio
Li_{0.67}FePO₄	Li	1.05
	Na	0.11
	Fe	0.65
	P	1

Table 5.1.3 The atomic ratio of the ion-exchanged alluaudite-Li_{0.67}FePO₄ at harsh conditions (5M LiBr in Hexanol for 48 hours at 170°C)

Atom	Multiplicity	x	y	z	B _{iso}	Occupancy
Li1	4	0	0.5	0	0.2(8)	0.564 (16)
Na1	4	0	0.5	0	0.2(8)	0.12(4)
Fe3	4	0	0.5	0	0.2(8)	0.088 (16)
Li2	4	0	-0.0048(19)	0.25	4.3(5)	0.512 (16)
Na2	4	0	-0.0048(19)	0.25	4.3(5)	0.401(9)
Fe4	4	0	-0.0048(19)	0.25	4.3(5)	0.062(16)
Fe1	4	0	0.2705(7)	0.25	3.8(2)	0.5904(16)
Li3	4	0	0.2705(7)	0.25	3.8(2)	0.266(17)
Fe2	8	0.2820(4)	0.6551(3)	0.3646(7)	3.08(10)	1(4)
P1	4	0	0.7095(7)	0.25	1.8(2)	1
P2	8	0.2429(8)	0.9001(6)	0.1385(14)	3.18(19)	1
O1	8	0.4498(9)	0.7248(9)	0.5246(19)	0.3(3)	1
O2	8	0.0957(11)	0.6304(9)	0.2333(16)	0.7(3)	1
O3	8	0.3361(10)	0.6656(11)	0.093(2)	2.0(3)	1
O4	8	0.1219(12)	0.4080(9)	0.2990(19)	2.8(4)	1
O5	8	0.2203(9)	0.830(10)	0.305(2)	1.6(3)	1
O6	8	0.3285(10)	0.5170(13)	0.3887(16)	2.2(3)	1

Table 5.1.4 Atomic position and occupancy of refined alluaudite

Li_{0.67}FePO₄ using the XRD pattern

Atom	Multiplicity	<i>x</i>	<i>y</i>	<i>z</i>	<i>B</i> _{iso}	Occupancy
Li1	4	0	0.5	0	1(4)	0.561 (17)
Na1	4	0	0.5	0	1(4)	0.132(9)
Fe3	4	0	0.5	0	1(4)	0.085 (3)
Li2	4	0	0.013(4)	0.25	2.2(11)	0.522 (17)
Na2	4	0	0.013(4)	0.25	2.2(11)	0.416(9)
Fe4	4	0	0.013(4)	0.25	2.2(11)	0.061(4)
Fe1	4	0	0.2589(9)	0.25	2.3(3)	0.591(5)
Li3	4	0	0.2589(9)	0.25	2.3(3)	0.28(19)
Fe2	8	0.2767(4)	0.6531(3)	0.3624(9)	1.33(7)	1(6)
P1	4	0	0.7056(7)	0.25	0.02(14)	1
P2	8	0.2368(6)	0.8904(6)	0.1370(13)	0.63(12)	1
O1	8	0.4519(6)	0.7149(5)	0.5347(12)	1.01(13)	1
O2	8	0.1009(6)	0.6343(5)	0.2387(11)	1.40(15)	1
O3	8	0.3357(6)	0.6672(6)	0.1045(10)	1.57(15)	1
O4	8	0.1198(6)	0.4042(5)	0.3035(12)	1.79(13)	1
O5	8	0.2211(5)	0.8213(4)	0.3266(9)	1.14(13)	1
O6	8	0.3181(5)	0.5010(5)	0.3808(11)	1.83(14)	1

Table 5.1.5 Atomic position and occupancy of refined alluaudite

Li_{0.67}FePO₄ using the ND pattern

5.1.5 References

- [1] K. Kang, Y. S. Meng, J. Breger, C. P. Grey and G. Ceder, *Science*, **311**, 977-980 (2006).
- [2] M. Armand and J. M. Tarascon, *Nature*, **451**, 652-657 (2008).
- [3] J. M. Tarascon and M. Armand, *Nature*, **414**, 359-367 (2001).
- [4] M. R. Palacin, *Chem. Soc. Rev.*, **38**, 2565-2575 (2009).
- [5] S. Y. Chung, J. T. Bloking and Y. M. Chiang, *Nat. Mater.*, **1**, 123-128 (2002).
- [6] P. S. Herle, B. Ellis, N. Coombs and L. F. Nazar, *Nat. Mater.*, **3**, 147-152 (2004).
- [7] A. K. Padhi, K. S. Nanjundaswamy and J. B. Goodenough, *J. Electrochem. Soc.*, **144**, 1188-1194 (1997).
- [8] Y. G. Wang, Y. R. Wang, E. J. Hosono, K. X. Wang and H. S. Zhou, *Angew. Chem.*, **47**, 7461-7465 (2008).
- [9] C. Delmas, M. Maccario, L. Croguennec, F. Le Cras and F. Weill, *Nat. Mater.*, **7**, 665-671 (2008).
- [10] P. Gibot, M. Casas-Cabanas, L. Laffont, S. Levasseur, P. Carlach, S. Hamelet, J. M. Tarascon and C. Masquelier, *Nat. Mater.*, **7**, 741-747 (2008).
- [11] S. Nishimura, G. Kobayashi, K. Ohoyama, R. Kanno, M. Yashima and A. Yamada, *Nat. Mater.*, **7**, 707-711 (2008).

- [12] B. Kang and G. Ceder, *Nature*, **458**, 190-193 (2009).
- [13] C. Delacourt, P. Poizot, J.-M. Tarascon and C. Masquelier, *Nat. Mater.*, **4**, 254-260 (2005).
- [14] A. Yamada, Y. Takei, H. Koizumi, N. Sonoyama, R. Kanno, K. Itoh, M. Yonemura and T. Kamiyama, *Chem. Mater.*, **18**, 804-813 (2006).
- [15] M. Yonemura, A. Yamada, Y. Takei, N. Sonoyama and R. Kanno, *J. Electrochem. Soc.*, **151**, A1352-A1356 (2004).
- [16] S. Y. Chung, J. G. Kim, Y. M. Kim and Y. B. Lee, *Adv. Mater.*, **23**, 1398-1403 (2011).
- [17] J. Kim, D. H. Seo, S. W. Kim, Y. U. Park and K. Kang, *Chem. Commun.*, **46**, 1305-1307 (2010).
- [18] S. Y. Chung, S. Y. Choi, S. Lee and Y. Ikuhara, *Phy. Rev. Lett.*, **108**, 195501 (2012).
- [19] S. Y. Chung, S. Y. Choi, T. Yamamoto and Y. Ikuhara, *Angew. Chem.*, **48**, 543-546 (2009).
- [20] S. Y. Chung, Y. M. Kim, J. G. Kim and Y. J. Kim, *Nat. Phys.*, **5**, 68-73 (2009).
- [21] P. B. Moore, *Am. Miner.*, **56**, 1955 (1971).
- [22] K. Trad, D. Carlier, L. Croguennec, A. Wattiaux, M. Ben Amara and C. Delmas, *Chem. Mater.*, **22**, 5554-5562 (2010).

- [23] K. Trad, D. Carlier, L. Croguennec, A. Wattiaux, M. Ben Amara and C. Delmas, *Inorg. Chem.*, **49**, 10378-10389 (2010).
- [24] T. J. Richardson, *J. Power Sources*, **119**, 262-265 (2003).
- [25] F. Hatert, P. Keller, F. Lissner, D. Antenucci and A. M. Fransolet, *Euro. J. Miner.*, **12**, 847-857 (2000).
- [26] R. D. Shannon and C. T. Prewitt, *Acta Cryst. B*, **B 25**, 925 (1969).
- [27] F. Zhou, C. A. Marianetti, M. Cococcioni, D. Morgan and G. Ceder, *Phy. Rev. B*, **69**, 4 (2004).
- [28] A. K. Padhi, K. S. Nanjundaswamy, C. Masquelier, S. Okada and J. B. Goodenough, *J. Electrochem. Soc.*, **144**, 1609-1613 (1997).
- [29] R. Malik, D. Burch, M. Bazant and G. Ceder, *Nano Lett.*, **10**, 4123-4127 (2010).

Chapter 6. Summary

In this thesis, the phosphate materials such as olivine, NASICON, and alluaudite are investigated for Li rechargeable batteries. Through various experiments, our targeted phosphate electrode materials are expected to have excellent battery performance for large-scale applications.

Olivine study is composed of three parts. First part is the study on Fe-Mg co-doped LiMnPO_4 which is investigated as a high power/energy cathode material. The electrochemical properties of LiMnPO_4 olivine cathode can be significantly improved by even small amounts of two transition metals that have either higher or lower redox potential than $\text{Mn}^{2+}/\text{Mn}^{3+}$. The coexistence of local Fe^{3+} -V- Mn^{2+} (or Mg^{2+} - Li^+ - Mn^{3+}) regions during (de)lithiation creates unfavorable Mn^{2+} -Vacancy (or Mn^{3+} - Li^+) pair neighbors that promote the $\text{Mn}^{2+}/\text{Mn}^{3+}$ redox reaction, which thereby acts as a nucleation enhancer. Easier and more frequent formation of nucleation in LiMnPO_4 significantly enhanced the rate capability, as evidenced by the electrochemical results. Second part is the study on the particle size effect on phase stability of LiMnPO_4 . The delithiated Li_xMnPO_4 having large particle size decomposes into $\text{Mn}_2\text{P}_2\text{O}_7$. However, when the particle size of LiMnPO_4 decreases from *ca.* 1 μm to *ca.* 50 nm, the delithiated Li_xMnPO_4 undergoes partial phase transformation into $\text{Mn}_3(\text{PO}_4)_2$ below 250°C. We believe that this change in

the decomposition reaction is purely size-driven due to the surface energy term of the Gibbs free energy. The third part is the study on the thermal stability of binary olivine $\text{LiFe}_{1-x}\text{Mn}_x\text{PO}_4$. The phase stability of $\text{LiFe}_{1-x}\text{Mn}_x\text{PO}_4$ was investigated as a function of the temperature, the Li composition into the structure, and the amounts of transition metals using temperature-controlled *in situ* XRD. Fully lithiated phase $\text{LiFe}_{1-x}\text{Mn}_x\text{PO}_4$ remained stable up to high temperatures (higher than 700°C). However, the delithiated phase $\text{Li}_{1-y}\text{Fe}_{1-x}\text{Mn}_x\text{PO}_4$ is less stable than the fully lithiated phase. Phase stability of $\text{Li}_{1-y}\text{Fe}_{1-x}\text{Mn}_x\text{PO}_4$ and the delithiation mechanism (one-phase vs. two-phase reaction) were significantly influenced by the Fe/Mn ratio in the structure. Mn-rich $\text{LiFe}_{1-x}\text{Mn}_x\text{PO}_4$ exhibited poorer thermal stabilities in the delithiated states than Fe-rich $\text{LiFe}_{1-x}\text{Mn}_x\text{PO}_4$ and has a stronger preference for the two-phase reaction.

NASICON study is focused on the improvement of electrochemical performance of monoclinic $\text{Li}_3\text{V}_2(\text{PO}_4)_3$. The electrochemical properties of monoclinic $\text{Li}_3\text{V}_2(\text{PO}_4)_3/\text{PEDOT}$ composite are significantly improved without any conductive carbon. By intrinsic oxidation power of delithiated $\text{Li}_{3-x}\text{V}_2(\text{PO}_4)_3$, EDOT (monomer of PEDOT) can be polymerized on the surface of $\text{Li}_3\text{V}_2(\text{PO}_4)_3$ and PEDOT is uniformly deposited. The coating of conducting polymer, PEDOT on the surface of $\text{Li}_3\text{V}_2(\text{PO}_4)_3$ lead to higher

power capability without conductive carbon. The utilization of core-shell structure with conductive polymer is suggested as a promising strategy for lithium ion batteries with high power performance.

Alluaudite study is the preparation of non-olivine LiFePO_4 with alluaudite crystal structure. The non-olivine LiFePO_4 with alluaudite structure was successfully prepared by additional lithiation of alluaudite- $\text{Li}_{0.67}\text{FePO}_4$. Additional intercalation of 0.23Li^+ ions into alluaudite- $\text{Li}_{0.67}\text{FePO}_4$ was possible when alluaudite- $\text{Li}_{0.67}\text{FePO}_4$ was discharged to 2.0V and cycling from LiFePO_4 to FePO_4 was reversible at the voltage range from 4.5V to 2.0V. The changed XRD peak position and lattice parameters of alluaudite- LiFePO_4 compared to alluaudite- $\text{Li}_{0.67}\text{FePO}_4$ could back up additional lithiation into alluaudite- $\text{Li}_{0.67}\text{FePO}_4$ and the formation of alluaudite- LiFePO_4 . Additionally, we could observe that $\text{Fe}^{2+}/\text{Fe}^{3+}$ redox couple of alluaudite LiFePO_4 was lower than that of olivine LiFePO_4 and alluaudite- LiFePO_4 has one-phase reaction during charge/discharge while olivine LiFePO_4 has two-phase reaction. This is the first report in which the composition of LiFePO_4 can exist as the alluaudite phase, not the olivine phase.

We believe that our extensive studies on the phosphate cathode materials can deliver the simulating hints for the next-generation Li rechargeable

batteries for Electric vehicles and its potential new applications.

Chapter 7 Abstract in Korean

세계적으로 지속가능하며 친환경적인 에너지에 대한 관심이 크게 증가하고 있으며, 이러한 에너지의 효과적인 활용을 위한 고효율 에너지 저장시스템인 이차전지에 대한 연구가 많이 이루어지고 있다. 특히, 리튬이차전지는 다른 에너지저장시스템에 비해 에너지 밀도, 파워출력 그리고 수명특성이 우수하기 때문에 휴대용 전자기기를 위한 에너지저장매체로 크게 관심을 받으며 사용되고 있으며, 최근에는 전기자동차와 같은 대용량 에너지저장시스템에 리튬이차전지를 사용하기 위한 집중적인 연구가 이루어지고 있는 상황이다. 하지만, 현재 상용화되어 사용되고있는 층상형계 리튬이차전지 양극재료의 경우 과충전시 그리고 낮은 온도에서 리튬탈리상의 구조 붕괴로 인해 발생하는 산소와 발열반응으로 인해 폭발 및 화재 가능성이 매우 높기 때문에 전기자동차와 같은 대용량 에너지저장체계에는 부적합하다. 따라서 안전한 리튬이차전지용 양극재료를 찾기 위한 많은 연구가 진행되어왔으며, 많은 후보군들 중에서, 인산염계 물질이 인과 산소 사이에 존재하는 강력한 공유결합으로 인해 열적안정성이 뛰어나고 높은 에너지밀도 및 수명특성으로 인해 크게 관심을 받고 있다. 본 논문에서는 올리빈, 나시콘, 알루아우다이트라는 다양한 인산염계 물질들에 대한 특성을 분석하고 전기화학적 특성을 향상시키고자 하였다.

올리빈 관련 연구는 총 세분야로 구성되어있다. 첫번째로, 차세대 리튬이차전지 양극재료로 크게 관심받고있는 LiMnPO_4 의 전기화학적 특성을 Fe와 Mg의 소량 도핑을 통해서 크게 향상시켰다. 기존의 LiMnPO_4 의 경우 충방전시 오직 한부분에서만 핵생성 및 핵성장이 나타나 구조에서 리튬이온의 삽입 또는 탈리되는 것이 힘들지만, Fe와 Mg가 있는 경우 다수의 핵생성 및 핵성장이 가능하게 되어 보다 쉽게 리튬이온이 삽입 또는 탈리되어 LiMnPO_4 의 파워출력을 크게 향상되었다. Fe와 Mg가 도핑된 $\text{LiFe}_{0.05}\text{Mn}_{0.05}\text{Mn}_{0.9}\text{PO}_4$ 는 C/5 ($1\text{C} = 170\text{mA g}^{-1}$)의 전류밀도에서 $\sim 140\text{mAh g}^{-1}$ 의 용량을 보였으며, 3C라는 매우 빠른 전류밀도에서도 110mAh g^{-1} 라는 매우 큰 방전 용량을 보였음을 확인하였다. 두번째로, 고온에서 Li_xMnPO_4 ($x < 1$)의 상안정성이 입자크기에 따라 크게 변화하였음을 확인하였다. 200nm이상의 크기를 가지는 Li_xMnPO_4 는 200도 이상에서 $\text{Mn}_2\text{P}_2\text{O}_7$ 로 분해되지만, 50nm 이하의 크기를 가지는 경우는 $\text{Mn}_3(\text{PO}_4)_2$ 로 분해되었다. 이처럼 입자크기에 따라 다른 분해과정을 가지는 이유는 입자크기에 따라 달라지는 표면에너지 차이가 크게 영향을 미치는 것임을 확인하였다. 세번째로, $\text{LiFe}_{1-x}\text{Mn}_x\text{PO}_4$ 의 열안정성을 평가하였고 리튬탈리상 $\text{Li}_{1-y}\text{Fe}_{1-x}\text{Mn}_x\text{PO}_4$ 의 열안정성이 Fe/Mn 비율에 따라 크게 영향 받는 것을 확인하였다. 리튬이 부분적으로 탈리된 상의 경우 고용화되는 온도가 Fe의 비율이 커질수록 낮아지는 것을 확

인하였고, 리튬이 모두 탈리된 상의 경우 분해온도가 Fe의 비율이 커질수록 높아져 Fe가 많이 함유되어있을수록 높은 열안정성을 가진다는 것을 확인하였다.

나시콘 구조에 대한 연구로, 차세대 리튬이차전지 양극재료로 크게 각광받고 있는 $\text{Li}_3\text{V}_2(\text{PO}_4)_3$ 를 저온공정을 통해 전도성 폴리머 PEDOT로 균일하게 코팅하여 전기화학적 특성을 크게 향상시켰다. $\text{Li}_3\text{V}_2(\text{PO}_4)_3/\text{PEDOT}$ 의 경우 10C ($1\text{C} = 133 \text{ mA g}^{-1}$)라는 큰 전류 밀도에서 이론용량의 90% 이상의 값인 $\sim 120 \text{ mAh g}^{-1}$ 의 방전용량을 보였으며, 수명특성 또한 100사이클 후에도 첫 사이클의 97%이상의 용량을 유지하고 있음을 확인하였다.

알루아우다이트 구조에 대한 연구로, 우리는 최초로 LiFePO_4 조성을 기존에 널리 알려진 올리빈 구조가 아닌 알루아우다이트 구조로 합성하고 특성을 평가하였다. 열린 구조를 가지고 있는 알루아우다이트 LiFePO_4 는 높은 파워출력을 보였으며, 구조 내에서 약 0.8몰의 리튬이온이 삽입 및 탈리되었다. 충방전시 기존의 올리빈 LiFePO_4 와는 달리 두상 반응이 아닌 단일상 반응 메커니즘을 보였으며, 평균 구동전압이 $\sim 2.95\text{V}$ 로 올리빈 LiFePO_4 에 비해 다소 낮은 값을 가지는 것을 확인하였다.

위의 결과를 종합해보면, 올리빈, 나시콘, 알루아우다이트와 같은 다양한 인산염계 물질들은 대용량 에너지저장체계에 이용될만큼

충분히 훌륭한 특성을 가지고 있음을 알수있었다. 본 논문의 연구 내용들이 전기자동차용 대용량 에너지저장을 위한 차세대 리튬이차전지 양극재료개발에 크게 기여할 수 있을 것이라 판단한다.

주요어 : 리튬이차전지, 인산염, 올리빈, 나시콘, 알루아우다이트
학번: 2011-30783

감사의 글

지난 대학원 과정 동안 학위를 마치는데 있어서 아직 부족한 점이 많지만 훌륭한 연구자가 될 수 있도록 많은 도움과 가르침을 주신 분들께 이 글을 빌어 감사의 말씀 드립니다.

먼저, 부족했던 저를 제자로 받아주시고 연구, 그리고 인생에 있어 많은 가르침과 열정을 가르쳐주신 저의 지도교수님 강기석 교수님께 진심으로 감사드립니다. 앞으로 연구자로서 살아가며 평생 교수님의 가르침을 마음 깊이 간직하고 교수님께 부끄럽지 않은 제자, 그리고 훌륭한 연구자가 되어 스승의 은혜 보답하도록 하겠습니다. 바쁘신 와중에도 학위심사를 위해 시간을 내주시고 조언을 아끼지 않으셨던 남기태 교수님, 장호원 교수님, 박찬범 교수님, 전석우 교수님께 깊은 감사의 마음을 전합니다.

늘 같은 공간에서 지내며 저를 도와준 연구실 분들에게도 감사함을 전달하고 싶습니다. 석사 때부터 지금까지 긴 시간 동안 못난 저 때문에 마음고생, 몸고생 많이해서 정말 미안한 동기 이승기 님은 혁조형, 앞으로 좋은 일만 가득하실 메탈에어 전문가 멋쟁이 진수형, 연구란 무엇인지 보여주시며 저를 반성하게 하셨던 영욱이형, 정말 못하는게 없는 부산의 자랑 지현이, 힘들 때 정말 많이 도와주시고 항상 감사한 정근이형, 언제나 열심히하는 모습이 멋진 해겸이, 풍류를 즐길줄 아는 멋진 형섭이형, 저질 선배덕에 가장 고통스러웠을 착하고 성실한 규영이, 특히 게임을 잘하고 못하는 게 없는 만능인 희대, 저를 커피의 세계로 인도해준 신사 인철이, 맨날 고기 굽게해서 미안한 계산왕이 될 병주, 진정한

달변가 흠장난이 성균이, 늘 열심히 연구 진행했던 인경이, 느리지만 운동 좀 하는 영준이, 살만 빼면 완벽할 잘생긴 교진이, 하스스톤 가르쳐준 못하는게 없는 똑똑한 갑인이, 외부에서 인물 좋다는 소리듣는 현아, 연구실 최고의 분위기 메이커 인상이, 이 모든 연구실 일원들에게 감사의 말씀을 전합니다.

그리고 저의 대학원 생활 동안 물심양면으로 정말 많이 도와주셨던 선배님 김성욱 박사님, 서동화 박사님, 연구실 최고의 간지를 보이신 이병헌 님은 상훈이형, 아무것도 모르고 한없이 귀찮음만 드렸지만 친절하게 정말 많은 걸 가르쳐주시고 대학원 생활에 큰 힘을 주신 이성재 박사님, 김주식 박사님께 정말 감사드립니다.

마지막으로 언제나 저를 응원해주시고 도와주신 사랑하는 가족에게 감사의 말씀 전합니다. 제가 어떠한 고난 없이 연구에 집중 할 수 있도록 도와주시고 힘들 때 저를 위해 기도하고 저에게 용기와 힘을 주시는 부모님, 하늘에서 저를 응원해주시고 지켜봐 주시는 할머니, 제게 믿음과 큰 힘을 주는 형님, 형수님, 누님, 매형께 진심 어린 감사의 마음과 사랑을 전합니다.

Curriculum Vitae

Name : Jongsoon Kim

Date of Birth : September 28, 1986

Phase of Birth : Naju, Jeollanam-do, Republic of Korea

Educational Background

2002-2003 : Chonnam Science High School

2004-2007 : Department of Materials Science and Engineering, KAIST (B.S.)

2008-2010 : Department of Materials Science and Engineering, KAIST (M.S.)

2011-2013 : Department of Materials Science and Engineering, Seoul
National University (Ph.D.)

List of Publications

Thesis

1. “Electrode material designs for lithium rechargeable batteries”, KAIST, M.S. Thesis, 2010 (in English)
2. “Tailoring phosphate cathode materials for high performance lithium rechargeable battery”, Seoul National University, Ph. D. Thesis, 2013 (in English)

International SCI-Journal

1. **J. Kim**, J.-K. Yoo, Y. S. Jung, and K. Kang, “ $\text{Li}_3\text{V}_2(\text{PO}_4)_3$ -Conducting Polymer as a High Power 4V-class Lithium battery electrode” *Adv. Energy Mater.*, 3, 1004-1007 (2013)
2. **J. Kim**, H. Kim, I. Park, Y.-U. Park, J.-K. Yoo, K.-Y. Park, S. Lee, and K. Kang, “ LiFePO_4 with Alluaudite crystal structure for Lithium ion Batteries” *Energy & Environ. Sci.*, 6, 830-834 (2013)
3. **J. Kim**[†], J.-K. Yoo[†], Y. S. Jung, and K. Kang, “Scalable Fabrication of Silicon Nanotubes and their Application to Energy Storage”, *Adv. Mater.*, 24, 5452–5456 (2012) († These authors contributed equally to this work)
4. **J. Kim**, K.-Y. Park, I. Park, J.-K. Yoo, J. Hong, and K. Kang,

- “Thermal stability of Fe-Mn binary olivine cathode for Li rechargeable battery” *J. Mater. Chem.*, 22, 11964-11970 (2012)
5. **J. Kim**, K.-Y. Park, I. Park, J.-K. Yoo, D.-H. Seo, S.-W. Kim and K. Kang, “The Effect of Particle Size on Phase Stability of the Delithiated Li_xMnPO_4 ”, *J. Electrochem. Soc.*, 159, A55-A59 (2012)
 6. **J. Kim**, Y.-U. Park, D.-H. Seo, J. Kim, S.-W. Kim, and K. Kang, “Mg and Fe co-doped Mn based Olivine Cathode Material for High Power Capability” *J. Electrochem. Soc.*, 158 (3), A250-A254 (2011)
 7. **J. Kim**, D.-H. Seo, S.-W. Kim, Y.-U. Park, and K. Kang, “Mn Based Olivine Electrode Material with High Power and Energy”, *Chem. Commun.*, 46, 1305-1307 (2010)
 8. **J. Kim**, S.-W. Kim, H. Gwon, W.-S. Yoon and K. Kang, “Comparative study of $\text{Li}(\text{Li}_{1/3}\text{Ti}_{5/3})\text{O}_4$ and $\text{Li}(\text{Ni}_{1/2-x}\text{Li}_{2x/3}\text{Ti}_{x/3})\text{Ti}_{3/2}\text{O}_4$ ($x=1/3$) anodes for Li rechargeable batteries” *Electrochim. Acta*, 54, 5914-5918 (2009)
 9. R. Essehli, B. El. Bali, A. Faik, M. Naji, S. Benmokhtar, Y.R. Zhong, L.W. Su, Z. Zhou, **J. Kim**, K. Kang, M. Dusek, “Iron titanium phosphates as high-specific-capacity electrode materials for lithium ion batteries”, *J. Alloy, Com.*, 585, 434-441 (2014)
 10. Y.-U. Park, D.-H. Seo, H.-S. Kwon, B. Kim, **J. Kim**, H. Kim, I. Kim,

- H.-I. Yoo, and K. Kang, “A new high-energy cathode for a Na-ion battery with ultra-high stability”, *J. Am. Chem. Soc.*, 135, 13870-13878 (2013)
11. H. Kim, I. Park, S. Lee, H. Kim, K.-Y. Park, Y.-U. Park, H. Kim, **J. Kim**, H.-D. Lim, W.-S. Yoon, and K. Kang, “Understanding the electrochemical mechanism of the new iron-based mixed-phosphate $\text{Na}_4\text{Fe}_3(\text{PO}_4)_2(\text{P}_2\text{O}_7)$ in a Na rechargeable battery”, *Chem. Mater.*, 25, 3614-3622 (2013)
12. J.-K. Yoo, **J. Kim**, H. Lee, J. Choi, M.-J. Choi, D. M. Sim, Y. S. Jung, and K. Kang, “Porous silicon nanowires for lithium rechargeable batteries”, *Nanotech.*, 24, 424008 (2013)
13. K.-Y. Park, J. Hong, **J. Kim**, Y.-U. Park, H. Kim, D.-H. Seo, S.-W. Kim, J.-W. Choi and K. Kang, “Factors that affect the phase behavior of multi-component olivine ($\text{LiFe}_x\text{Mn}_y\text{Co}_{1-x-y}\text{PO}_4$; $0 < x, y < 1$) in lithium rechargeable batteries: One-phase reaction vs. two-phase reaction” *J. Electrochem. Soc.*, 160, A444-A448 (2013)
14. R. A. Shakoor, D.-H. Seo, H. Kim, Y.-U. Park, **J. Kim**, S.-W. Kim, H. Gwon, S. Lee and K. Kang, “A combined first principles and experimental study on $\text{Na}_3\text{V}_2(\text{PO}_4)_2\text{F}_3$ for rechargeable Na batteries” *J. Mater. Chem.*, 22, 20535-20541 (2012)

15. H. Kim, S. Lee, Y.-U. Park, H. Kim, **J. Kim**, S. Jeon and K. Kang, “Neutron and X-ray diffraction study of pyrophosphate-based $\text{Li}_{2-x}\text{MP}_2\text{O}_7$ (M = Fe, Co) for lithium rechargeable battery electrodes”, *Chem. Mater.*, 23, 3930-3937, (2011)
16. S.-W. Kim, V. G. Kumar, D.-H. Seo, Y.-U. Park, J. Kim, H. Kim, **J. Kim**, J. Hong, and K. Kang, “Preparation and Electrochemical Characterization of Doped Spinel $\text{LiMn}_{1.88}\text{Ge}_{0.1}\text{Li}_{0.02}\text{O}_4$ Cathode Material” *Elect. Mater. Lett.*, Vol. 7, No. 2, 105-108 (2011)
17. H. Kim, D.-H. Seo, S.-W. Kim, **J. Kim**, and K. Kang, “Highly Reversible Co_3O_4 /Graphene Hybrid Anode for Lithium Rechargeable Batteries” *Carbon*, 49, 326-332 (2011)
18. S.-W. Kim, D.-H. Seo, H. Gwon, **J. Kim**, and K. Kang, “Fabrication of FeF_3 Nanoflowers on CNT Branches and Their Application to High Power Lithium Rechargeable Batteries” *Adv. Mater.*, 22 (46), 5260 (2010)
19. Y.-U. Park, **J. Kim**, H. Gwon, D.-H. Seo, S.-W. Kim, and K. Kang, “Synthesis of Multi-component Olivine by a Novel Mixed Transition Metal Oxalate Coprecipitation Method and Electrochemical Characterization”, *Chem. Mater.*, 22 (8), 2573-2581 (2010)
20. D.-H. Seo, H. Gwon, S.-W. Kim, **J. Kim**, and K. Kang,

- “Multicomponent Olivine Cathode for Lithium Rechargeable Batteries: A First-Principles Study” *Chem. Mater.*, 22 (2), 518-23 (2010)
21. H. Gwon, D.-H. Seo, S.-W. Kim, **J. Kim**, and K. Kang, “Combined First-Principles and Experimental Study on Multi-Components Olivine Cathode for Lithium Rechargeable Batteries”, *Adv. Funct. Mater.*, 19, 3285-3292 (2009)
22. S.-W. Kim, **J. Kim**, H. Gwon and K. Kang, “Phase Stability Study of $\text{Li}_{1-x}\text{MnPO}_4$ ($0 < x < 1$) Cathode for Li Rechargeable Battery”, *J. Electrochem. Soc.*, 156, 8 (2009)
23. S.-W. Kim, T. H. Han, **J. Kim**, H. Gwon, H.-S. Moon, S.-W. Kang, S. O. Kim and K. Kang, “Fabrication and Electrochemical Characterization of TiO_2 Three-Dimensional Nanonetwork Based on Peptide Assembly” *ACS Nano*, 3 (5), 1085-1090 (2009)

Domestic Journal

1. J. Kim, S. Yoon, J.-K. Yoo, **J. Kim**, H. Kim, K. Kang, “Highly Laminated Electrospun ZnO Nanofibrous Film on the Transparent Conducting Oxide for Photovoltaic Device” *J. Electrochem. Sci. Tech.*, 3, 68-71 (2012)

2. R. A. Shakoor, Y.-U. Park, **J. Kim**, S.-W. Kim, D.-H. Seo, H. Gwon, and Kisuk Kang, “Synthesis of $\text{NaFePO}_4/\text{NaCoPO}_4$ and their application to Sodium Batteries” *J. Korean Battery Soc.*, 3, 00-00 (2010)

Domestic Patent

1. “망간을 기초로 하는 올리빈 복합고용체 및 이의 제조방법”
Korea Patent, [KR] 10-1134511
2. “스피넬 복합고용체 및 이의 제조방법” Korea Patent, [KR] 10-1166908

International Conference

1. **J. Kim**, H. Kim, I. Park, Y.-U. Park, J.-K. Yoo, K.-Y. Park, S. Lee, and K. Kang, “Non-olivine LiFePO_4 with Alluaudite structure for Lithium rechargeable Battery”, *ECS Fall meeting 2013*, October 27-November 1, 2013, San Francisco. U.S.A. (Oral)
2. **J. Kim**, K.-Y. Park, I. Park, J.-K. Yoo, J. Hong, and K. Kang, “Thermal stability of Fe-Mn binary olivine cathodes for Li rechargeable batteries”, *Prime 2012 (ECS Fall meeting)*, October 7-12, 2012, Hawaii. U.S.A. (Oral)

3. **J. Kim**, D.-H. Seo, S.-W. Kim, Y. U. Park, and K. Kang, “Highly Improved Power Capability of the Mn based Olivine Cathode Material”, *Advanced Electrochemical Energy Symposium*, December 28-30, 2011, Hong-Kong, China (Oral)
4. **J. Kim**, D.-H. Seo, S.-W. Kim, Y. U. Park, and K. Kang, “Electrode material designs for lithium rechargeable batteries” *ECS Spring Meeting*, May1-6, 2011, Montreal, Canada (Oral)
5. **J. Kim**, D.-H. Seo, S.-W. Kim, Y. U. Park, and K. Kang, “Nucleation Enhancers: Significantly Improved Power Capability of the Mn based Olivine Cathode Material”, *219th ECS Meeting*, May 2, 2011, Montréal, Canada (Oral)
6. **J. Kim**, H. Gwon, and K. Kang, “Synthesis and characterization of LiMnPO_4 as a cathode material for lithium secondary batteries”, *3rd Asian Conference on Electrochemical Power Sources*, November 10-12, 2008, Seoul, Korea (Poster)
7. S.-W. Kim, D.-H. Seo, H. Gwon, **J. Kim**, and K. Kang, “Iron fluoride based cathode materials for lithium rechargeable batteries”, *219th ECS Meeting*, May 2, 2011, Montréal, Canada (Oral)
8. Y.-U. Park, **J. Kim**, H. Gwon, D.-H. Seo, S.-W. Kim, and K. Kang, “Synthesis of Multicomponent Olivine by a Novel Mixed Transition

Metal Oxalate Coprecipitation Method and Electrochemical Characterization”, *IMLB 2010*, June 29, 2010, Montréal. Canada (Oral)

9. H. Kim, D.-H. Seo, S.-W. Kim **J. Kim**, and K. Kang, “Co₃O₄/graphene hybrid anode with high reversibility for lithium rechargeable batteries”, *3rd International Conference on Advanced Lithium Batteries for Automobile Application*, September 8, 2010, Seoul. Korea (Poster)
10. D.-H. Seo, H. Gwon, S.-W. Kim **J. Kim**, and K. Kang, “A First-Principles Study on the Multi-Component Olivine Cathode for Lithium Rechargeable Batteries”, *3rd International Conference on Advanced Lithium Batteries for Automobile Application*, September 8, 2010, Seoul. Korea (Poster)
11. H. Gwon, D.-H. Seo, S.-W. Kim **J. Kim**, and K. Kang, “Combined First-Principle and Experimental Study on Multi-Components Olivine Cathode”, *LIBD 2009*, September 20, 2009, Arcachon, France (Oral)

Domestic Confenernce

1. **J. Kim**, H. Kim, I. Park, Y.-U. Park, J.-K. Yoo, K.-Y. Park, S. Lee,

and K. Kang, "LiFePO₄ with Alluaudite structure for Lithium rechargeable Battery", *2013 Spring Meeting of the Korean Electrochemical Society*, April 11-13, 2013, Chang-Won. Korea (Oral)

2. **J. Kim**, J.-K. Yoo, Y. S. Jung, and K. Kang, "Scalable Fabrication of Silicon Nanotubes and their Application to Energy Storage", *The 20th Korean conference on Semiconductors*, February 4-6, 2013, Pyeong-Chang. Korea (Oral)
3. **J. Kim**, K.-Y. Park, I. Park, J.-K. Yoo, D.-H. Seo, S.-W. Kim and K. Kang, "The Effect of Particle Size on Phase Stability of Olivine LiMnPO₄ Cathode Material for Li Rechargeable Batteries", *ENGE*, September 16-19, 2012, Jeju, Korea (Oral)
4. **J. Kim**, K.-Y. Park, I. Park, J.-K. Yoo, J. Hong, and K. Kang, "Thermal stability of binary Fe-Mn olivine cathode materials", *2012 Spring Meeting of the Korean Battery Society*, May 17, 2012, Daejeon. Korea (Oral)
5. **J. Kim**, Y. U. Park, D.-H. Seo, J. Kim, S.-W. Kim, and K. Kang, "Mg and Fe Co-doped LiMnPO₄ for High Power Capability", *10th Anniversary Meeting of the Korean Battery Society*, December 1, 2011, Jeju. Korea (Poster)

6. **J. Kim**, D.-H. Seo, S.-W. Kim, Y. U. Park, and K. Kang, “Nucleation Enhancer; Mn based olivine cathode material with high power and Energy”, *2010 Spring Meeting of Korean Battery Society*, May 27-28, 2010, Siheung, Korea (Oral)
7. **J. Kim**, D.-H. Seo, S.-W. Kim, Y. U. Park, and K. Kang, “Li(FeCo)_{0.05}Mn_{0.9}PO₄; 고출력의 망간을 기초로하는 올리빈 구조의 양극물질”, *2010 Spring Meeting of Korea Electrochemical Society*, April 22-24, 2010, Jeju, Korea (Poster)
8. **J. Kim**, S.-W. Kim, H. Gwon, W. Yoon, and K. Kang, “Comparative study of Li(Li_{1/3}Ti_{5/3})O₄ and Li(Ni_{1/2-x}Li_{2x/3}Ti_{x/3})Ti_{3/2}O₄ (x = 1/3) anodes for Li rechargeable batteries”, *2009 Fall Meeting of Korean Ceramic Society*, October 19-20, 2009, Daejeon, Korea (Oral)
9. **J. Kim**, S.-W. Kim, H. Gwon, W. Yoon, and K. Kang, “Comparative study of Li(Li_{1/3}Ti_{5/3})O₄ and Li(Ni_{1/2-x}Li_{2x/3}Ti_{x/3})Ti_{3/2}O₄ (x = 1/3) anodes for Li rechargeable batteries”, *2009 Spring Meeting of Korean Battery Society*, May 28-29, 2009, Seoul, Korea (Poster)
10. K.-Y. Park, I. Park, H. Kim, **J. Kim**, J. Hong and K. Kang, “Defect recombination upon charge carrier injection in crystal: Anti-site re-ordering in Li_xFePO₄”, *2013 Fall Meeting of the Korean Battery*

Society, November 28, 2013, Jeju. Korea (Poster)

11. Y.-U. Park, D.-H Seo, H.-S Gwon, B. Kim, **J. Kim**, H. Kim, I. Kim, H.-I. Yoo, and K. Kang, “A high-energy cathode for a Na-ion battery with long cycle life”, *2013 Fall Meeting of the Korean Battery Society*, November 28, 2013, Jeju. Korea (Poster)
12. Y.-U. Park, D.-H Seo, H.-S Gwon, B. Kim, **J. Kim**, H. Kim, I. Kim, H.-I. Yoo, and K. Kang,, “A novel high-energy cathode for a Na-ion battery with long cycle life”, *2013 Fall Meeting of the Korean Electrochemical Society*, November 8, 2013, Daejeon. Korea (Oral)
13. H. Kim, I. Park, S. Lee, H. Kim, K.-Y. Park, Y.-U. Park, H, Kim, **J. Kim**, H.-D Lim, W.-S. Yoon, and K. Kang,, “Understanding the structural evolution of iron-based mixed-phosphate cathodes for Na rechargeable battery”, *2013 Fall Meeting of the Korean Electrochemical Society*, November 8, 2013, Daejeon. Korea (Oral)
14. J.-K. Yoo, **J. Kim**, Y. S. Jung, and K. Kang,, “Scalable method of one-dimensional silicon nanostructures for lithium-ion batteries”, *2013 Spring Meeting of the Korean Electrochemical Society*, April 11-13, 2013, Chang-Won. Korea (Oral)
15. R. A. Shakoor, D.-H. Seo, H. Kim, Y.-U. Park, **J. Kim**, S.-W. Kim, H. Gwon, S. Lee and K. Kang, “A Combined First Principles and

Experimental Study on $\text{Na}_3\text{V}_2(\text{PO}_4)_2\text{F}_3$ for Na Rechargeable Batteries”, *2012 Fall Meeting of Korean Ceramic Society*, October 19-20, 2012, Daejeon. Korea (Oral)

16. K.-Y. Park, Y.-U. Park, **J. Kim**, J. Hong, and K. Kang, “Phase transformation Study of Multi-component Olivine at Various Composition”, *10th Anniversary Meeting of the Korean Battery Society*, December 1, 2011, Jeju. Korea (Poster)
17. H. Kim, S. Lee, Y.-U. Park, H. Kim, **J. Kim**, S. Jeon, and K. Kang, “Neutron and X-ray Diffraction analysis of Pyrophosphate-Based $\text{Li}_{2-x}\text{MP}_2\text{O}_7$ (M= Fe, Co) for Lithium Rechargeable Battery cathode materials”, *10th Anniversary Meeting of the Korean Battery Society*, December 1, 2011, Jeju. Korea (Poster)
18. H. Kim, D.-H. Seo, S.-W. Kim **J. Kim**, and K. Kang, “Highly reversible anode for lithium rechargeable batteries”, *2010 Spring Meeting of Korean Battery Society*, May 27, 2010, Montréal. Canada (Oral)
19. Y.-U. Park, **J. Kim**, H. Gwon, D.-H Seo, S.-W. Kim, and K. Kang, “Preparation of Multicomponent Olivine by a Mixed Oxalate Coprecipitation Method and Its Electrochemical Characterization”, *2010 Spring Meeting of Korean Battery Society*, May 27, 2010,

Montréal. Canada (Oral)

20. Y.-U. Park, **J. Kim**, H. Gwon, D.-H Seo, S.-W. Kim, and K. Kang, “Synthesis of Multicomponent Olivine by a Novel Mixed Transition Metal Oxalate Coprecipitation Method and Electrochemical Characterization”, *2010 Spring Meeting of Materials Research Society of Korea*, May 13, 2010, Samchuck. Korea (Oral)
21. D.-H. Seo, H. Gwon, S.-W. Kim **J. Kim**, and K. Kang, “Combined First-Principles and Experimental Study on Multi-components Olivine Cathode”, *2009 Fall Meeting of Korean Ceramic Society*, October 19-20, 2009, Daejeon, Korea (Poster)
22. H. Gwon, D.-H. Seo, S.-W. Kim **J. Kim**, and K. Kang, “Combined First-Principles and Experimental Study on Multi-components Olivine Cathode”, *2009 Fall Meeting of Korean Battery Society*, November 26, 2009, Daejeon, Korea (Oral)
23. D.-H. Seo, H. Gwon, S.-W. Kim **J. Kim**, and K. Kang, “Multi-Component Olivine Cathode for Lithium Rechargeable Batteries: A First-Principles Study”, *2009 Fall Meeting of Korean Battery Society*, November 26, 2009, Daejeon, Korea (Poster)
24. S.-W. Kim, T. H. Han, **J. Kim**, H. Gwon, H.-S. Moon, S.-W. Kang, S. O. Kim, and K. Kang, “Fabrication and Electrochemical

Characterization of TiO₂ Three-Dimensional Nanonetwork Based on Peptide Assembly”, *2009 Spring Meeting of Korean Battery Society*, May 28, 2009, Seoul, Korea (Oral)

25. S.-W. Kim, **J. Kim**, H. Gwon, and K. Kang, “Phase Stability Study of Li_{1-x}MnPO₄ (0 < x < 1) Cathode for Li Rechargeable Battery”, *2009 Spring Meeting of Korean Battery Society*, May 28, 2009, Seoul, Korea (Poster)

26. S.-W. Kim, **J. Kim**, H. Gwon, and K. Kang, “고안정성 TiO₂ 나노네트워크 소재의 합성 및 에너지 저장 특성 평가”, *2009 Meeting of Korea Institute of Military Science and Technology*, August 27, 2009, Jeju, Korea (Oral)